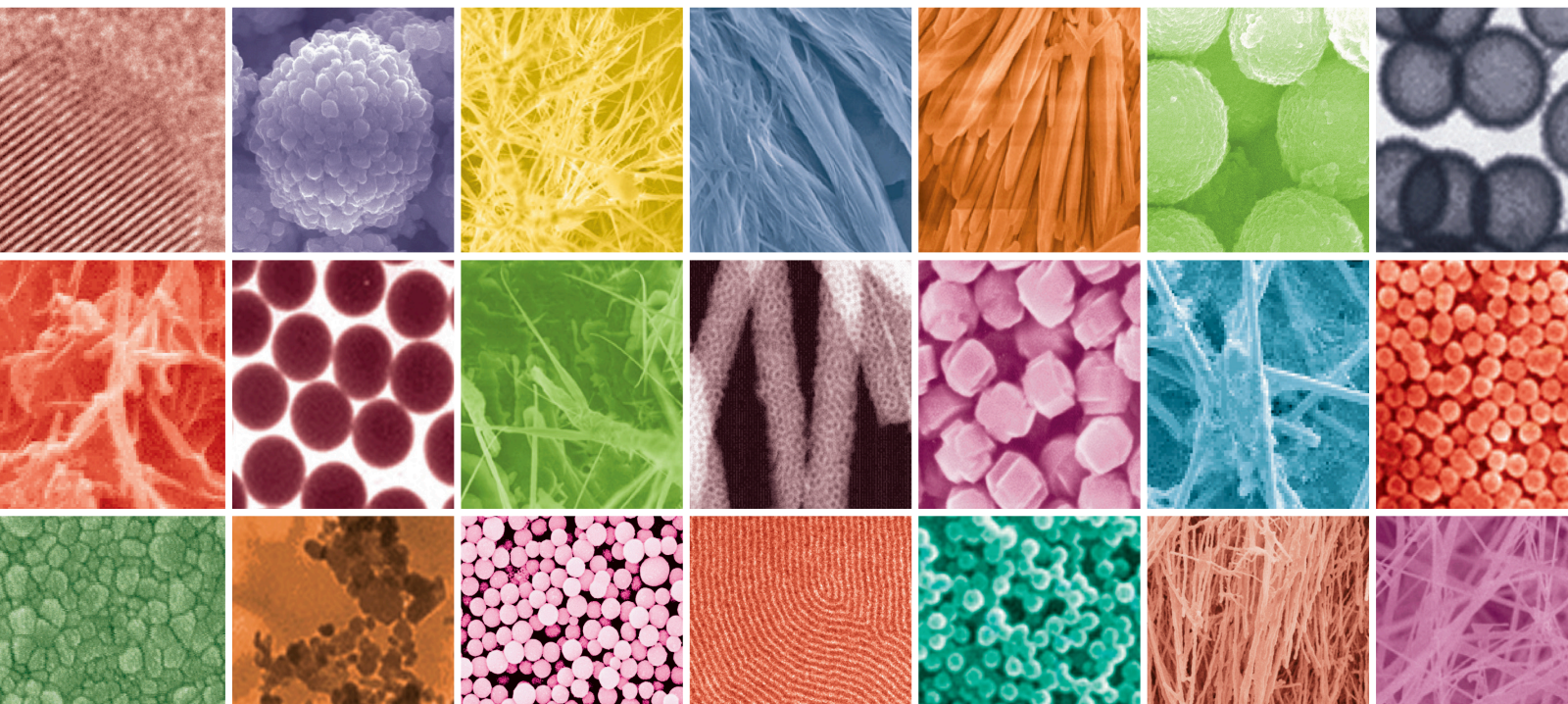


Cellular Responses to Nanomaterials with Biomedical Applications

Lead Guest Editor: Luis Jesús Villarreal Gómez

Guest Editors: Yanis Toledano Magaña, José Manuel Cornejo Bravo, Ricardo Vera Graziano, and Shengqiang Cai





Cellular Responses to Nanomaterials with Biomedical Applications

Journal of Nanomaterials

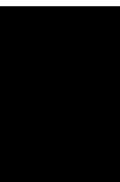
Cellular Responses to Nanomaterials with Biomedical Applications

Lead Guest Editor: Luis Jesús Villarreal Gómez

Guest Editors: Yanis Toledano Magaña, José

Manuel Cornejo Bravo, Ricardo Vera Graziano, and

Shengqiang Cai



Copyright © 2022 Hindawi Limited. All rights reserved.

This is a special issue published in "Journal of Nanomaterials." All articles are open access articles distributed under the Creative Commons Attribution License, which permits unrestricted use, distribution, and reproduction in any medium, provided the original work is properly cited.

Chief Editor

Stefano Bellucci, Italy

Editorial Board






Nagamalai, India
Buzuayehu Abebe, Ethiopia
Domenico Acierno, Italy
Ümit Ağbulut, Turkey
Katerina Aifantis, USA
Ibrahim Alarifi, Saudi Arabia
Nageh K. Allam, USA
Martin Andersson, Sweden
Raul Arenal, Spain
Hassan Azzazy, Egypt
Vincenzo Baglio, Italy
Lavinia Balan, France
Thierry Baron, France
Andrew R. Barron, USA
Enrico Bergamaschi, Italy
Debes Bhattacharyya, New Zealand
Sergio Bietti, Italy
Raghvendra A. Bohara, India
Mohamed Bououdina, Saudi Arabia
Victor M. Castaño, Mexico
Albano Cavaleiro, Portugal
Bhanu P. S. Chauhan, USA
Shafiqul Chowdhury, USA
Yu-Lun Chueh, Taiwan
Elisabetta Comini, Italy
Giuseppe Compagnini, Italy
David Cornu, France
Miguel A. Correa-Duarte, Spain
P. Davide Cozzoli, Italy
Anuja Datta, USA
Loretta L. Del Mercato, Italy
Yong Ding, USA
Yu Dong, Australia
Zehra Durmus, Germany
Ovidiu Ersen, France
Ana Espinosa, France
Claude Estournès, France
liyuxing@xaut.edu.cn Eswaramoorthy, India
Giuliana Faggio, Italy
Andrea Falqui, Saudi Arabia
Matteo Ferroni, Italy
Ilaria Fratoddi, Italy
Chong Leong Gan, Taiwan
Siddhartha Ghosh, Singapore
Filippo Giubileo, Italy
Iaroslav Gnilitskiy, Ukraine
Fabien Grasset, Japan
Jean M. Greneche, France
Kimberly Hamad-Schifferli, USA
Simo-Pekka Hannula, Finland
Michael Harris, USA
Yasuhiko Hayashi, Japan
Michael Z. Hu, USA
Zafar Iqbal, USA
Balachandran Jeyadevan, Japan
Xin Ju, China
Hassan Karimi-Maleh, Iran
Antonios Kelarakis, United Kingdom
Ali Khorsand Zak, Iran
Philippe Knauth, France
Prashant Kumar, United Kingdom
Eric Le Bourhis, France
Shijun Liao, China
Meiyong Liao, Japan
Silvia Licoccia, Italy
Nathan C. Lindquist, USA
Zainovia Lockman, Malaysia
Jim Low, Australia
Gaurav Mago, USA
Muhamamd A. Malik, United Kingdom
Ivan Marri, Italy
Laura Martinez Maestro, United Kingdom
Sanjay R. Mathur, Germany
Tony McNally, United Kingdom
Yogendra Mishra, Denmark
Paulo Cesar Morais, Brazil
Paul Munroe, Australia
Jae-Min Myoung, Republic of Korea
Rajesh R. Naik, USA
Albert Nasibulin, Russia
Toshiaki Natsuki, Japan
MU NAUSHAD, Saudi Arabia
Hiromasa Nishikiori, Japan
Sherine Obare, USA
Won-Chun Oh, Republic of Korea
Abdelwahab Omri, Canada
Ungyu Paik, Republic of Korea
Dillip K. Panda, USA

Mazeyar Parvinzadeh Gashti, Canada
Edward A. Payzant, USA
Alessandro Pegoretti, Italy
Oscar Perales-Pérez, Puerto Rico
Jorge Pérez-Juste, Spain
Suresh Perumal, India
Alexey P. Popov, Finland
Ram Prasad, India
Thathan Premkumar, Republic of Korea
Helena Prima-García, Spain
Alexander Pyatenko, Japan
Haisheng Qian, China
You Qiang, USA
Philip D. Rack, USA
Mohammad Rahimi-Gorji, Belgium
Baskaran Rangasamy, Zambia
Ilker S. Bayer, Italy
Lucien Saviot, France
Shu Seki, Japan
SENTHIL KUMARAN SELVARAJ, India
Gaurav Sharma, India
Donglu Shi, USA
Jagpreet Singh, India
Surinder Singh, USA
Bhanu P. Singh, India
Vladimir Sivakov, Germany
Pingan Song, Australia
Adolfo Speghini, Italy
Kishore Sridharan, India
Marinella Striccoli, Italy
Andreas Stylianou, Cyprus
Fengqiang Sun, China
Ashok K. Sundramoorthy, India
Angelo Taglietti, Italy
Bo Tan, Canada
Leander Tapfer, Italy
Valeri P. Tolstoy, Russia
Muhammet S. Toprak, Sweden
Sri Ramulu Torati, Republic of Korea
R. Torrecillas, Spain
Achim Trampert, Germany
Adriana Trapani, Italy
Takuya Tsuzuki, Australia
Tamer Uyar, USA
Cristian Vacacela Gomez, Ecuador
Luca Valentini, Italy
Viet Van Pham, Vietnam

Antonio Vassallo, Italy
Ester Vazquez, Spain
Ajayan Vinu, Australia
Ruibing Wang, Macau
Magnus Willander, Sweden
Zhi Li Xiao, USA
Ping Xiao, United Kingdom
Yingchao Yang, USA
Hui Yao, China
Yoke K. Yap, USA
Dong Kee Yi, Republic of Korea
Jianbo Yin, China
William Yu, USA
Michele Zappalorto, Italy
Wenhui Zeng, USA
Renyun Zhang, Sweden









Contents

Cellular Responses to Nanomaterials with Biomedical Applications

Luis Jesús Villarreal Gómez , Yanis Toledano Magaña , José Manuel Cornejo Bravo , Ricardo Vera Graziano , and Shengqiang Cai 


Editorial (3 pages), Article ID 9823140, Volume 2022 (2022)

Antimicrobial Effect of Electrospun Nanofibers Loaded with Silver Nanoparticles: Influence of Ag Incorporation Method

Luis Jesús Villarreal-Gómez , Graciela Lizeth Pérez-González , Nina Bogdanchikova , Alexey Pestryakov , Vadim Nimaev , Anastasiya Soloveva , José Manuel Cornejo-Bravo , and Yanis Toledano-Magaña 


Review Article (15 pages), Article ID 9920755, Volume 2021 (2021)

Corrigendum to “Effects of Arsenic Trioxide-Loaded PLGA Nanoparticles on Proliferation and Migration of Human Vascular Smooth Muscle Cells”

Susu Zhao, Zeqian Yu, Yifen Zhang, and Mei Lin 




Corrigendum (1 page), Article ID 9826376, Volume 2021 (2021)

Effects of Arsenic Trioxide-Loaded PLGA Nanoparticles on Proliferation and Migration of Human Vascular Smooth Muscle Cells

Susu Zhao, Zeqian Yu, Yifen Zhang, and Mei Lin 



Research Article (8 pages), Article ID 5575370, Volume 2021 (2021)

The Magnetic Nanomaterial Biofunctions in Cancer Diagnosis and Therapy

Xuefeng Bian, Ting Guo , Ji Zhang, Jianguo Xia, Xiaoqian Feng, Fujin Wang, Mei Lin , and Weizhong Tian 


Review Article (9 pages), Article ID 9968166, Volume 2021 (2021)

Evaluation of Inflammatory and Calcification after Implantation of Bioabsorbable Poly-L-Lactic Acid/Amorphous Calcium Phosphate Scaffolds in Porcine Coronary Arteries

Gaoke Feng , Chaoshi Qin, Fei Sha, Yongnan Lyu, Jinggang Xia, and Xuejun Jiang 

Research Article (8 pages), Article ID 6652648, Volume 2021 (2021)

In Vivo Evaluation of the Antitumor and Immunogenic Properties of Silver and Sodium Dichloroacetate Combination against Melanoma

Zaida Torres-Cavazos, Moisés Armides Franco-Molina , Silvia Elena Santana-Krímiskaya, Cristina Rodríguez-Padilla, Jorge Ramsy Kawas-Garza, Gustavo Hernández-Vidal, Gustavo Moreno-Degollado, and Diana Elisa Zamora-Ávila

Research Article (8 pages), Article ID 3741019, Volume 2020 (2020)

Editorial

Cellular Responses to Nanomaterials with Biomedical Applications

Luis Jesús Villarreal Gómez ^{1,2} **Yanis Toledoño Magaña** ³
José Manuel Cornejo Bravo ² **Ricardo Vera Graziano** ⁴ and **Shengqiang Cai** ⁵

¹Facultad de Ciencias de la Ingeniería y Tecnología, Universidad Autónoma de Baja California, Tijuana, Baja California, Mexico

²Facultad de Ciencias Químicas e Ingeniería, Universidad Autónoma de Baja California, Tijuana, Baja California, Mexico

³Facultad de Ciencias de la Salud, Universidad Autónoma de Baja California, Ensenada, Baja California, Mexico

⁴Instituto de Investigaciones en Materiales, Universidad Nacional Autónoma de México, Ciudad de México, Mexico

⁵Department of Mechanical and Aerospace Engineering, University of California San Diego, San Diego, California, USA

Correspondence should be addressed to Luis Jesús Villarreal Gómez; luis.villarreal@uabc.edu.mx

Received 9 March 2022; Accepted 9 March 2022; Published 8 April 2022

Copyright © 2022 Luis Jesús Villarreal Gómez et al. This is an open access article distributed under the Creative Commons Attribution License, which permits unrestricted use, distribution, and reproduction in any medium, provided the original work is properly cited.

Nanotechnology application to the biomedical field has gained significant interest. Great efforts have been made to develop nanogels, nanoparticles, and nanofibers, among others, to treat cardiovascular diseases, cancer, immune or metabolic system disorder, neurodegeneration, etc. The study of the cellular response against nanomaterials becomes essential for these potential applications. This Special Issue presents original research and review articles that illustrate and stimulate the advances in physiological processes that take place in tissue exposed to nanomaterials, such as cellular stress, adaptation mechanisms, immunological responses, biochemical pathways and cascades, pathologies, and clinical cases, among others.

1. Introduction

Nanomaterials have been gained great importance in the biomedical applications, and the evaluation of the tissue response in presence of them is one of the most important features to assess [1, 2]. Nanomaterials led to an active development of bioactive compounds that promote molecular processes for the regulation of cellular mechanisms. Still, not much literature has reported the mechanism of action of cells that interact with nanomaterials [3].

[4] discussed that physicochemical properties in nanomaterials define biocompatibility, bioactivity, and safety. In this sense, size, chemical composition of the surface, shape, charge, and topography influence cell response [5]. Hence, the proper design of the nanomaterials taking into account the above properties will elicit desired cell responses and enhanced targeting, drug delivery, cell attachment, and differentiation [6].

This special issue has 5 papers that discuss the biological effects of nanomaterials.

[7]. compared the antimicrobial effect of electrospun nanofibers loaded with silver nanoparticles prepared by different methods. It is well known that the antimicrobial bioactivity of silver nanoparticles is effective, and its use is versatile, becoming attractive to the biomedical industry. On the other hand, the electrospun nanofibers possess properties that can widen the applications of silver nanoparticles. However, silver nanoparticle bioactivity depends on the loading of silver ions into electrospun nanofibers. This review compared several methods of incorporating silver particles into electrospun nanofibers and evaluated their antimicrobial activity, discussed each procedure's limitations, and suggested the most promising one. This review showed that the preferred techniques for incorporating silver nanoparticles were direct blending and ultraviolet irradiation methods due to their simplicity and high efficiency. It was also found that polyacrylonitrile nanofibers (PAN) were reported to be the most frequently adopted polymer carrier for silver nanoparticles. In conclusion, silver nanoparticle-loaded nanofibers show high antimicrobial activity, regardless of the employed method [7].

[8] discussed the effects of the arsenic trioxide-loaded PLGA nanoparticles on the proliferation and migration of human vascular smooth muscle cells. In this report, As_2O_3 -PLGA-NPs were prepared and characterized. The energy dispersive spectrometry (EDS) has been used to confirm that the prepared nanoparticles contained elements of arsenic. The surface coating of the eluting stent of As_2O_3 -PLGA-NPs has the same characteristics as their self-prepared As_2O_3 -PLGA-NPs, and it also has a drug-sustained release character. Compared with the control group, cell proliferation and migration cells were significantly suppressed depending on the tested concentration. On the other hand, As_2O_3 -PLGA-NP depression mRNA, protein expression of Bcl-2 and MMP-9, and increased Bax mRNA and protein expression were altered when the concentration of the As_2O_3 -PLGA-NPs changed. In conclusion, the authors discussed that the As_2O_3 -PLGA-NPs inhibit human umbilical vein smooth muscle cell's (HUVSMC's) proliferation and migration. It may work via regulating Bax, Bcl-2, and MMP-9 expression *in vitro* [8].

In another study, the functions of magnetic nanomaterial in cancer diagnosis and therapy were discussed. The magnetic nanomaterials were demonstrated as a useful technology for life science and biomedical engineering in this work. These applications are most promising in cancer diagnosis due to their sensitivity and accuracy. Magnetic nanomaterials are also exploited as targeted drug carriers to increase sensitivity and reduce the side effects of chemotherapeutic drugs. Herein, this study discussed the preparation, characterization, and surface modification of various magnetic nanomaterials and their cancer diagnosis and therapy applications [9].

Moreover, the evaluation of inflammatory and calcification after implanting bioabsorbable poly-L-lactic acid/amorphous calcium phosphate scaffolds in porcine coronary arteries was reported. [10] confirmed that the addition of nanoamorphous calcium phosphate (ACP) materials could improve the support of poly-L-lactic acid (PLLA) vascular scaffolds. Based on this, this group continued to explore the effect of a novel bioresorbable scaffold composed of PLLA and ACP nanoparticles on the inflammation and calcification of surrounding tissues after scaffold implantation in a porcine coronary artery. It was found that there is no statistically significant difference between the evaluated CRP, calcium, and ALP groups at 1, 6, 12, and 24 months. The inflammation score, NF- κ B positive expression index, and calcification score in the PLLA/ACP group were lower than those in the PLLA group for 12 and 24 months. The ALP positive expression index in the PLLA/ACP group was lower than that in the PLLA group at 6, 12, and 24 months. Western blot results showed that the IL-6 expression level in the PLLA/ACP group was significantly lower than that in the control group at 6, 12, and 24 months.

Moreover, the expression of BMP-2 in the PLLA/ACP was significantly lower than in the control group at 12 and 24 months. In this study, it was demonstrated that the PLLA/ACP composite scaffold has adequate biocompatibility. Nanoscale ACP incorporation can reduce the inflammatory response induced by the PLLA scaffold acid metabolites,

procalcification factor expression in the body, and inhibit tissue calcification, making them optimal for the application and development of degradable vascular scaffolds [10].

Finally, [11], evaluate the antitumor and immunogenic properties of silver and sodium dichloroacetate combination against melanoma. Their main focus was to assess the efficacy of silver and sodium dichloroacetate as dual-function agents in melanoma treatment. Moreover, the group evaluated if the cell death mechanism induced by their treatments was immunogenic cell death. Their results showed that colloidal silver and sodium dichloroacetate combination is more effective than each treatment alone and that the antitumor mechanism is not through immunogenic cell death. Furthermore, this study can broadly contribute to the development of dichloroacetate-loaded silver nanoparticles and the design of targeted pharmacological formulations to fight melanoma and other types of cancer [11].

Conflicts of Interest

The authors declare that they have no conflicts of interest.

Luis Jesús Villarreal Gómez
Yanis Toledano Magaña
José Manuel Cornejo Bravo
Ricardo Vera Graziano
Shengqiang Cai

References

- [1] E. González-Solveyra and I. Szeifer, "What is the role of curvature on the properties of nanomaterials for biomedical applications?," *Wiley Interdisciplinary Reviews on Nanomedicine and Nanobiotechnology*, vol. 8, no. 3, pp. 334–354, 2016.
- [2] F. Villanueva-Flores, A. Castro-Lugo, O. T. Ramírez, and L. A. Palomares, "Understanding cellular interactions with nanomaterials: towards a rational design of medical nanodevices," *Nanotechnology*, vol. 31, no. 13, article 132002, 2020.
- [3] X. Q. Liu and R. Z. Tang, "Biological responses to nanomaterials: understanding nano-bio effects on cell behaviors," *Drug Delivery*, vol. 24, no. sup1, pp. 1–15, 2017.
- [4] W. Sun and Z. Gu, "Engineering DNA scaffolds for delivery of anticancer therapeutics," *Biomaterial Sciences*, vol. 3, no. 7, pp. 1018–1024, 2015.
- [5] S. Dhar, V. Sood, G. Lohiya, H. Deivendran, and D. S. Katti, "Role of physicochemical properties of protein in modulating the nanoparticle-bio interface," *Journal of Biomedical Nanotechnology*, vol. 16, no. 8, pp. 1276–1295, 2020.
- [6] X. Wang, C. H. Chang, J. Jiang et al., "Mechanistic differences in cell death responses to metal-based engineered nanomaterials in Kupffer cells and hepatocytes," *Small*, vol. 16, no. 21, article e2000528, 2020.
- [7] L. J. Villarreal-Gómez, G. L. Pérez-González, N. Bogdanchikova et al., "Antimicrobial effect of electrospun nanofibers loaded with silver nanoparticles: influence of Ag incorporation method," *Journal of Nanomaterials*, vol. 2021, Article ID 9920755, 15 pages, 2021.
- [8] S. Zhao, Z. Yu, Y. Zhang, and M. Lin, "Effects of arsenic trioxide-loaded PLGA nanoparticles on proliferation and

- migration of human vascular smooth muscle cells,” *Journal of Nanomaterials*, vol. 2021, Article ID 5575370, 8 pages, 2021.
- [9] X. Bian, T. Guo, J. Zhang et al., “The magnetic nanomaterial biofunctions in cancer diagnosis and therapy,” *Journal of Nanomaterials*, vol. 2021, Article ID 9968166, 9 pages, 2021.
- [10] G. Feng, C. Qin, F. Sha, Y. Lyu, J. Xia, and X. Jiang, “Evaluation of inflammatory and calcification after implantation of bioabsorbable poly-L-lactic acid/amorphous calcium phosphate scaffolds in porcine coronary arteries,” *Journal of Nanomaterials*, vol. 2021, Article ID 6652648, 8 pages, 2021.
- [11] Z. Torres-Cavazos, M. A. Franco-Molina, S. E. Santana-Krímskaya et al., “*In vivo* evaluation of the antitumor and immunogenic properties of silver and sodium dichloroacetate combination against melanoma,” *Journal of Nanomaterials*, vol. 2020, Article ID 3741019, 8 pages, 2020.

Review Article

Antimicrobial Effect of Electrospun Nanofibers Loaded with Silver Nanoparticles: Influence of Ag Incorporation Method

Luis Jesús Villarreal-Gómez ^{1,2}, Graciela Lizeth Pérez-González ^{1,2},
Nina Bogdanchikova ³, Alexey Pestryakov ^{4,5}, Vadim Nimaev ⁶, Anastasiya Soloveva ⁶,
José Manuel Cornejo-Bravo ² and Yanis Toledano-Magaña ⁷

¹Facultad de Ciencias de la Ingeniería y Tecnología, Universidad Autónoma de Baja California, Unidad Valle de las Palmas, Blvd. Universitario 1000, CP, 21500 Tijuana, Baja California, Mexico

²Facultad de Ciencias Químicas e Ingeniería, Universidad Autónoma de Baja California, Unidad Otay, Universidad #14418, UABC, Parque Internacional Industrial Tijuana, Tijuana, Baja California, Mexico

³Centro de Nanociencias y Nanotecnología, Universidad Nacional Autónoma de México, Km 107, Carretera Tijuana-Ensenada, CP, 22860 Ensenada, Baja California, Mexico

⁴Department of Technology of Organic Substances and Polymer Materials, Tomsk Polytechnic University, 634050 Tomsk, Russia

⁵Research Department, Sevastopol State University, Sevastopol, 299053, Russia

⁶Research Institute of Clinical and Experimental Lymphology-Branch of the Institute of Cytology and Genetics, Siberian Branch of Russian Academy of Sciences, Novosibirsk, Russia

⁷Escuela de Ciencias de la Salud Unidad Valle Dorado, Universidad Autónoma de Baja California, Ensenada 22890, Baja California, Mexico

Correspondence should be addressed to Luis Jesús Villarreal-Gómez; luis.villarreal@uabc.edu.mx

Received 3 March 2021; Accepted 29 July 2021; Published 17 August 2021

Academic Editor: Antonios Kelarakis

Copyright © 2021 Luis Jesús Villarreal-Gómez et al. This is an open access article distributed under the Creative Commons Attribution License, which permits unrestricted use, distribution, and reproduction in any medium, provided the original work is properly cited.

The antimicrobial bioactivity of silver nanoparticles is well known, and they can be used widely in many applications, becoming especially important in the biomedical industry. On the other hand, the electrospun nanofibers possess properties that can enhance silver nanoparticle applicability. However, silver nanoparticle bioactivity differs depending on the loading of silver ions into electrospun nanofibers. This review is aimed at comparing different silver incorporation methods into electrospun nanofibers and their antimicrobial activity, discussing each procedure's limitations, and presenting the most promising one. This review showed that the preferred techniques for incorporating silver nanoparticles were *direct blending* and *ultraviolet irradiation* methods due to their simplicity and efficient results. Besides, polyacrylonitrile nanofibers (PAN) have been the most reported system loaded with silver nanoparticles. Finally, independently of the technique used, silver nanoparticle-loaded nanofibers show high antimicrobial activity in all cases.

1. Introduction

In the last decades, the interest of the biomedical industry in nanomaterials has increased due to its promising applications against different diseases. In this sense, AgNPs are among the most studied nanomaterials principally due to their highly efficient antimicrobial properties [1–6]. It is known that AgNP efficiency increases using a carrier [4].

Electrospun nanofibers are ideal carriers for AgNPs since their small dimensions permit homogeneous distribution and avoid mass aggregation. The blend of technologies between nanofibers and nanoparticles maximizes both structure properties, making them an ideal amalgam for many applications.

Electrospun nanofibers are synthesized by the electrospinning technique, which allows the generation of ultrafine

fibers using natural or synthetic biomaterials [7–9]. These three-dimensional scaffolds are produced in a 10–1000 nm diameter's range [10–18]. Nanofiber's properties such as nanometric thickness, controllable porosity, and high surface contact area [7, 8] allow the potential applications in tissue engineering [19, 20], drug delivery systems [21–24], biosensor fabrication [25, 26], energy storage [27], solar cells [28], water filtration [29, 30], catalysis [31, 32], and sensing [33, 34], among other uses. Specifically, the loading of electrospun nanofibers with AgNPs has become attractive [35–37] for many applications such as food packaging [38], filters [39]. Moreover, there are investigations of electrospun nanofibers loaded with AgNPs for their use in healthcare and other biomedical applications [37, 40, 41], including wound dressing [9] and implants [40].

Thus, this amalgam of nanofiber/AgNP system properties has been proved and attributed to the metallic nanoparticle proportion, size, and spatial distribution of AgNPs in the fibers [42] (*entry 3*).

The AgNP-loaded electrospun systems can control the silver ions released through the immobilization of the AgNPs [43]. Strategies for the fabrication of AgNP-loaded nanofibers include incorporation of silver nitrate (AgNO_3) by *direct blending* into the polymeric solution followed by photoreduction with ultraviolet (UV) *irradiation* [44–46], *thermal reduction* [47] (*entry 14*), or *the silver mirror reaction* [48] (*entry 12*), among other methods.

A comparative study of AgNP loading methods on PVA was performed by electrospinning AgNO_3 -polymeric solutions followed by a reduction posttreatment. In that study, the AgNPs were mixed in the polymer solution before the electrospinning process, and the resulting polymeric scaffolds were immersed in a silver solution followed by a reduction process (comparing UV and thermal treatments). The authors reported that UV reduction was the more efficient method to incorporate AgNPs on nanofibers' surfaces [49].

In this work, we compare the results published regarding the incorporation of AgNPs in nanofibers, including all the above methods. Nevertheless, AgNP-loaded nanofibers differ in their activity depending on the silver loading method into the nanofibers. Hence, this review compares different techniques of AgNP incorporation into electrospun nanofibers and their antimicrobial effectivity to identify the most promising method and discuss the current limitation of each of them.

2. Methods of AgNP Immobilization for Loading of Electrospun Nanofibers

In literature, several strategies merge the electrospun nanofibers and AgNPs, which coat the nanofibers' surface or are embedded into the bulk [50].

The parameters considered in this work to determine the best among the discussed methods include the AgNP distribution in/on the electrospun fibers. Bortolassi et al. discussed that the bioactivity of the AgNPs depends on their capacity to attach to the microbial cell membrane's surface, altering the permeability and cellular homeostatic, thereby AgNP distribution and availability over the surface of the fibers become

crucial for the bioactivity. Hence, the combination of the high specific surface area of the electrospun fibers and an AgNP high loading with homogeneous distribution over the surface of the fibers become a desirable design for the high final antimicrobial activity [51, 52]. For instance, the loaded AgNP nanofibers fabricated by the direct addition of AgNPs into the polymeric solution decreased the antimicrobial efficiency of AgNPs due to their aggregation. When the AgNPs are incrustated in the fibers, they are not exposed for direct contact with the cellular membrane [53].

Also, it is remarkable that the presence of AgNPs into/on the polymeric nanofibers affects its intrinsic properties. The most important characteristic that is modified is its bioactivity, which is improved [46, 51–53]. Among other properties that are affected by the presence of the AgNPs on/in the fibers are the mechanical properties such as reduction in surface tension [54], increase in average fiber diameter [36], and changes in thermal properties including the glass transition temperature, degradation temperature, and temperature-dependent mass loss. In general, AgNP-loaded nanofibers are more resistant to heat. All property changes mentioned above are caused by the structural changes of the polymeric backbone [36, 46, 47].

Below, we present and compare several methods to create AgNP-loaded electrospun nanofiber scaffolds.

2.1. Direct Blending Method. A facile method to produce AgNP-loaded nanofibers is the *direct blending* of premade AgNPs in the polymer solution before electrospinning [35], being preferred the AgNP colloidal solutions for easy incorporation into the nanofibers [55]. The encapsulation of AgNPs within the poly(ϵ -caprolactone) (PCL) microfibers without Ag at the surface of microfibers allows controlling release of AgNPs from the hybrid constructs in combination with high antibacterial activity [56].

Several polymeric systems have been reported to be electrospun and loaded with AgNPs, such as the case of poly(vinylidene fluoride) (PVDF) [20] (*entry 4*), PVA/poly(urethane) (PU) [57] (*entry 2*), nylon [42, 58], and poly(vinyl pyrrolidone) (PVP) [59] (*entry 1*), among others. This versatility of modified nanofibers is because AgNPs can be prepared with various solvents such as formic acid (FA), dimethylacetamide (DMAc), water (H_2O), and hexafluoro propanol (HFIP). Also, it has been recognized by several studies that the loaded amount of AgNPs can greatly differ from 0.1 to 30% wt., of the total polymeric mass. On the other hand, it has been observed that the higher the content of AgNPs added to the polymeric solution, the higher the conductivity, promoting smaller fiber's diameters [35, 55]. These resultant fiber morphologies can be rough due to the coating and immersion of AgNPs mentioned before [55].

2.1.1. Experimental Conditions of the Direct Blending Method. For a reported direct blending technique, the first step was the dissolution at 50°C of nylon 6 (15% wt.) in formic acid, a reduction agent for AgNO_3 . In this study, the AgNO_3 (0.5 and 1.25% wt.) was slowly added to the polymer solution, kept in darkness with constant stirring at room temperature for 24 h, enough time for the reduction of

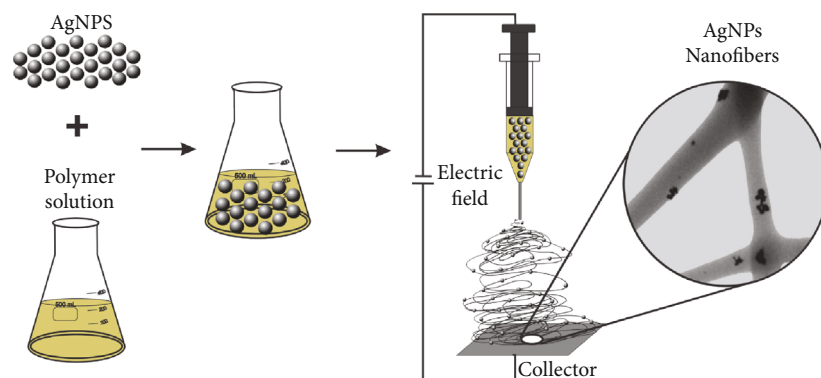


FIGURE 1: Direct blending method for incorporation of AgNPs on nanofibers. Based on [41, 55, 59].

AgNO₃. After that, the final dispersion was electrospun [42] (entry 3).

In another study, tannic acid prepared in an ammonia solution (NH₃·H₂O) was added to the polymer solution as a reducing agent of AgNO₃. After one hour, the powder obtained by solution concentration was resuspended in acetone and filtered. Synthesized AgNPs were extracted using vacuum drying at room temperature and then added to a PVP solution before electrospinning (Figure 1).

2.2. UV-Irradiation Method. The amount of AgNPs loaded on nanofibers is more significant when a UV-irradiation method is used to produce the initial silver burst release, either in the form of AgNPs or in the residual Ag⁺ ions. This method promotes incorporating the AgNPs into nanofibers' surface in a random distribution [44–46]. The method induces the silver ion migration from the core to the surface during the formation of the AgNPs [45]. Also, it has been described that the UV-irradiation method achieves smaller AgNP diameters with narrower distributions than the other methods. These results are relevant for antimicrobial activity because the high surface area of AgNPs promotes a faster Ag⁺ ion release [60] (entries 8 and 16).

Moreover, the biological activity of electrospun scaffolds is related to the AgNO₃ content. It was reported that AgNP-loaded poly(ether amide) (PEBA) fibers were fabricated using 0.15% of AgNO₃ in the polymer solution for electrospinning inhibits >99.99% of *Staphylococcus aureus* (*S. aureus*) and *Escherichia coli* (*E. coli*) cultures. However, when the AgNO₃ concentration decreased (0.05% AgNO₃), the bacterial inhibition decreases (20% less activity in both bacterial strains) [61] (entry 7). A similar activity was observed on loaded AgNPs in gelatin nanofibers evaluated against *S. aureus* and *E. coli*, with selective activity for the later strain. Authors suggest that the different biocidal effect is due to the generous peptidoglycan layer next to the cell membrane of Gram-positive bacteria such as *S. aureus*, which serves as a protective structure for external threats reducing the AgNP introduction to the bacterial cell [60].

Phan et al. [46] (entry 5) synthesized silver/polyacrylonitrile (Ag/PAN) nanocomposite membranes testing their antibacterial activity. In this study, electrospun AgNP/PAN nanofibers were prepared from the solution of PAN and

AgNO₃ using the UV-irradiation method to reduce the Ag⁺ ions into AgNPs. The nanofiber antibacterial activity was tested against *E. coli* and *Bacillus subtilis* (*B. subtilis*), finding long-term bactericidal effects. The authors claim that these nanofiber systems are useful for water purification, bacterial filtration, and biomedical devices [46] (entry 5).

2.2.1. Experimental Conditions of the UV-Irradiation Method. In the case of the UV-irradiation method, most of the studies prepared the Ag-loaded nanofibers by mixing the polymeric and AgNO₃ solutions previous to the electrospinning process [44, 45, 60–62] except for Phan et al. [46] (entry 5) that electrospun the fibers before the AgNO₃ incorporation. An advantage of this method is that, as reported, no extra time or additional solvent is required [44–46, 60–63]. Besides, no further treatments are needed after the irradiation step, and the exposition time to UV light can be changed depending on the desired results. Interestingly, it has been reported that after four hours of irradiation, the number and size of the AgNPs continuously increased [44]. Figure 2 explains the UV-irradiation method general procedure, where the incrustated AgNPs can be appreciated over the nanofiber surface.

Additionally, the electrospinning conditions in both methods (*direct blending* and *UV irradiation*) are selected depending on the polymer system used [62]. After the electrospinning process, the UV irradiation step is developed. Here, the UV light's specific wavelengths are 254 and 365 nm [46] (entry 5), but not a specific irradiation time is presented. Several conditions are reported as follows: UV light (254 nm) irradiation for 24 h [46] (entry 5), UV light (254 nm) for 6 h [61] (entry 7), UV light (254 and 365 nm) irradiation from 10 min to 8 h [44] (entry 10), UV light (254 nm) irradiation for 10 min [45] (entry 9), UV light (365 nm) irradiation from 3 h [62] (entries 8 and 16), and UV light (not defined wavelength) irradiation for 4 h [63] (entry 6).

2.3. Silver Mirror Reaction Method (SMR). The SMR method is a versatile method that uses different substances as reducing agents for AgNO₃ solution to produce the AgNPs, which coat the surface of an object submerged in the reaction solution. This reduction can generate a visual phenomenon that

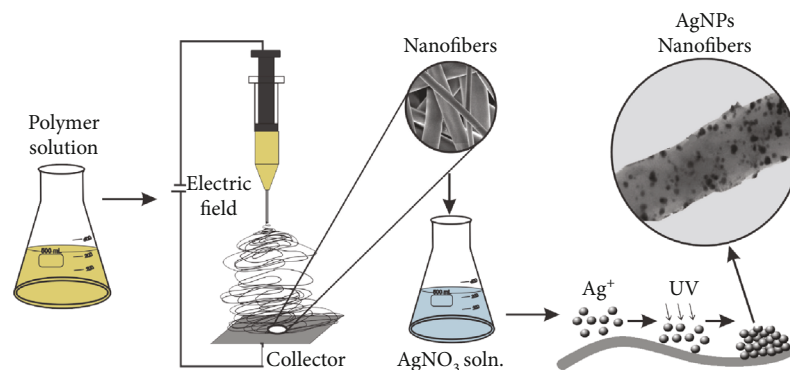


FIGURE 2: UV-irradiation method for incorporation of AgNPs on nanofibers. Based on [44–47, 60–63].

resembles a shiny mirror coat over the upper surface of the solution or over an object submerged.

It is used to create a controllable smooth coating over different surfaces: for large surfaces (e.g., telescope glasses) and extremely small surfaces (nanofibers) [64] (*entry 13*). The reaction occurs at ambient conditions, which is very appropriate for nanotechnology applications [65] (*entry 11*). Even though using this method is impossible to achieve shape control of AgNPs, the technique can produce quasispheres, wires, rods, right bipyramids, beams, spheres, cubes, or octahedrons [65, 66].

Several applications have been reported for SMR synthesized nanofibers. Excellent antimicrobial activities against bacteria and fungi were observed with PAN/AgNP nanofibers with AgNPs evenly dispersed on the nanofiber's external surface. Those were prepared with PAN nanofibers pretreated in AgNO_3 aqueous solution followed by the SMR process [48]. Also, noble metal nanoparticles loaded on electrospun nanofibers have been synthesized due to their potential use as sensors [67]. Another application is for silver nanowire membranes, in this case, Ag^+ ions coated poly(acrylonitrile-co-phenylethylene) (P(AN-S)) nanofibers used as a template for the reduction of a silver solution on the nanofibers' surface. The SMR process allows silver deposition on the nanofiber's surface. Thus, nanowires were developed and characterized by scanning electron microscopy (SEM), energy dispersive spectrometry (EDS), and X-ray diffraction (XRD). These nanowires have different resistance and transmittance on PET and glass: $15\ \Omega/\text{sq}$ and 80%, and $37\ \Omega/\text{sq}$ and 81%, respectively [65].

2.3.1. Experimental Conditions of the SMR Method. The reported methodologies differ in time and posttreatment steps [53, 54], but an advantage over other methods is that the reaction can be made at room temperature. In two manuscripts, the polymeric solution needs a 12 h reaction at room temperature before the electrospinning process [48, 65]. In another study, just 30 min were used, and a sol-gel process was done before the electrospinning step [64]. Hence, the polymer solution preparation time is not standardized and differs depending on the methodology used to achieve complete polymer dissolution. Wang et al. prepared PAN nanofibers stirring the polymeric solution just for 1 hour at room temperature, using the same polymer as the compared stud-

ies. Hence, these polymeric solution reaction times can vary depending on the polymer chosen and the AgNP incorporation method [11]. Within the reported procedures, we can find nanofibers exposed to the AgNO_3 solution for 18 and 24 h in a dark room at room temperature [48], and AgNO_3 solution mixed with the polymer solution before the electrospinning process [64, 65]. Hence, the AgNO_3 solution can be added before or after the formation of fibers.

Regarding electrospinning, parameters depend more on the polymeric solution than on the AgNP immobilization method or the presence of AgNO_3 . The electrospinning parameters determine the morphology, diameter, porosity, and distribution of the fibers [20]. After fiber preparation, several posttreatments are needed. Obtained fibrous mats are submerged into AgNO_3 solution at the desire concentration, usually in a 1:2 AgNO_3 /polymer solution ratio, but other relative proportions AgNO_3 /polymer were also tested [64, 65]. Ag^+ ions are deposited over the fiber's surface when the AgNO_3 solution is added to the fibers earlier prepared. In contrast, Ag^+ ions get encapsulated into the fibers if AgNO_3 solution is added before fiber preparation [68]. Other procedures include fibrous scaffolds freeze-drying before the SMR [48] or a two-step filtration with an organic-free filter followed by a $0.2\ \mu\text{m}$ filter to removed particles [64].

Other differences were observed for the reported SMR step. In some cases, the authors dropped ammonium hydroxide (NH_4OH) into AgNO_3 solution to prepare a diamine silver (I) ($\text{Ag}(\text{NH}_3)_2^+$) solution [65] (*entry 11*). Others used a hydrazinium hydroxide ($\text{N}_2\text{H}_5\text{OH}$) solution as a reducing agent [64] (*entry 13*). On the other hand, Shi et al. [48] (*entry 12*) submerged the fibers into the AgNO_3 solution, then added concentrated ammonia (NH_3) (2.5% wt.) into the beakers just until the brown precipitate dissolved, and then added formaldehyde (HCHO) (1% wt.) as the final step. Additional steps after SMR as a threefold washing procedure with distilled water or 40°C vacuum oven drying are reported [64, 65].

A simplified schematization of the silver mirror reaction method showing the AgNP distribution on the nanofiber's surface is represented in Figure 3.

2.4. Thermal Reduction Method. This method is promising due to the easy steps to perform. Some advantages of this method are as follows: uniform AgNP distribution on the

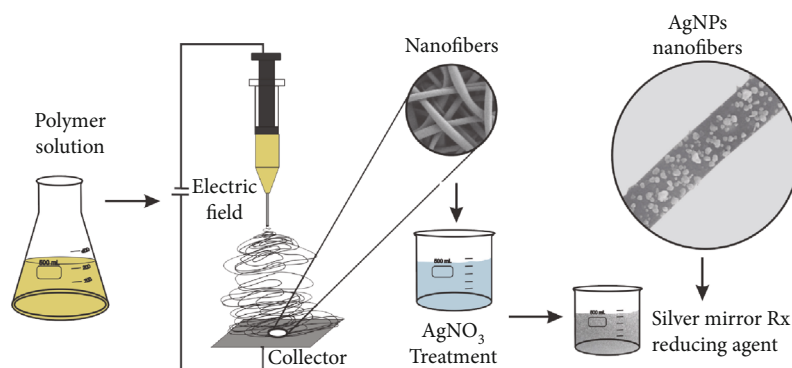


FIGURE 3: Silver mirror reaction method for incorporation of AgNPs on nanofibers. Based on [48, 61, 65, 68].

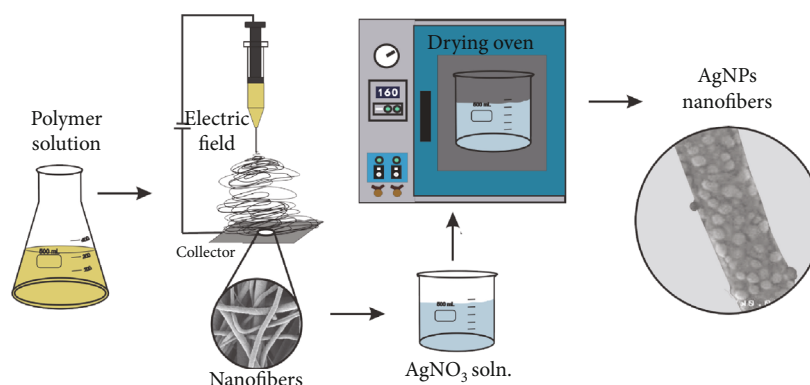


FIGURE 4: Thermal treatment method for incorporation of AgNP on nanofibers. Based on [47, 62, 70].

nanofiber's cross-section [69], decomposition temperature decreases when Ag content increases on PVA-AgNPs [49, 62], and more desired stability (less probability of AgNP aggregation). However, AgNP leaching could inactivate the membrane once the first Ag^+ release from the nanofiber surface has occurred [62].

Silver conducting nets were synthesized using the thermal reduction method over a plane scaffold prepared with electrospun nanofibers of poly(methyl methacrylate) (PMMA), and silver trifluoroacetate (STA) deposited on transparent substrates. Those nets had high transmittance and low resistance [70]. STA is reduced to AgNPs with a 100°C postthermal treatment that decomposes the organic polymer to achieve the one-dimensional net configuration. The nets' sheet resistance was as low as $15\ \Omega/\text{sq}$ correlated with the morphology and the STA/PMMA ratio. Properties as surface plasmon resonances (SPRs), fiber morphologies, and electrical and optical properties (diffusive optical transparency of $\approx 54\%$) were determined.

2.4.1. Experimental Conditions of the Thermal Reduction Method. For this method, several strategies are reported to incorporate the Ag^+ ions into the nanofibers. Jatoi et al. [47] (entry 14) prepared acetate cellulose (CA) solution under constant stirring for 24 h and then electrospun the solution. On the other hand, Chen et al. [70] (entry 15) replaced the AgNO_3 solution with an STA solution and mixed it with the PMMA solution using a reaction time of

24 h at room temperature. Similarly, Lin et al. [62] (entries 8 and 16) mixed the previously prepared (~ 2 h) PVA solution with the AgNO_3 solution stirring vigorously for an additional 30 min, taking just 2.5 h before the electrospinning step.

For the electrospinning technique, no special modifications were added. The optimization of the fiber formation and the electrospinning parameters were chosen depending on the properties (viscosity, concentration, conductivity, and surface tension) of the polymer solution [20, 47, 62, 70].

CA fibrous mats were synthesized with a simple alkaline treatment (NaOH) by submerging the fibers in the solution for 48 h, creating cellulose fibers (CEF). The CEAg samples were obtained immersing the CEF for 24 h at 23°C in an AgNO_3 solution then dried for 2 h. Finally, the reduction process of CEAg was done in a drying oven at 160°C for 1 h, 1.5 h, and 2 h [47]. Silver nets also could be obtained by thermal decomposition at 500°C of PMMA for 3 h under air or nitrogen atmosphere. In this case, AgNPs were obtained by reduction of silver precursors for 12 h at 100°C [70]. Contrary to the previous two discussed methods, before the electrospinning process, Lin et al. [62] (entries 8 and 16) pretreated the polymeric/ AgNO_3 solution at 105°C for 1 h, no further treatments after the obtention of the fibers.

Figure 4 represents the general procedure of the *thermal reduction method*.

AgNP particle size and average nanofiber diameter obtained with four AgNP incorporation methods are presented in Table 1.

TABLE 1: Physicochemical and antimicrobial properties of AgNP-nanofiber systems prepared by different methods.

Entry	AgNP electrospun system	Method used	AgNP size nm	Nanofibers/fiber size	[AgNO ₃]/[polymer] % wt.	[loaded AgNPs]/[polymer] % wt.	[AgNO ₃]/[loaded AgNPs]	Characterization	Method (medium used)	Antimicrobial activity (% effectivity)	Applications	Ref.
1	AgNPs/FK/PVP/PEO	Direct blending method	13.67 ± 2.95 nm	~140-300 nm	120 mmol/L AgNO ₃ /12% FK	0-3% AgNPs/12% FK	120 mmol/L AgNO ₃ /0-3% AgNPs	SEM-EDX, TEM, XRD, TGA, tensile stress, antibacterial activity	Inhibition zone method (LB agar)	8.24 mm inhibition zone, (<i>E. coli</i>) 2.08 mm inhibition zone, (<i>S. aureus</i>)	Biomedical applications	[58]
2	AgNPs/WPU/PVA	Direct blending method	5.1 ± 0.6 nm	290 ± 35 nm	1% AgNPs/15% WPU/PVA	Not tested/15% WPU/PVA	1% AgNPs/not tested	TEM/SEM, TGA, XPS, antibacterial assay, cytotoxicity assay	Inhibition zone assay (nutrient agar)	2.4-fold inhibition (<i>S. aureus</i>) 1.6-fold (<i>E. coli</i>)	Antimicrobial agents, wound dressings, and water or air purification techniques. A	[56]
3	AgNPs/nylon 6	Direct blending method	2-4 nm	~50-150 nm	0.5-1.25% AgNO ₃ /15% nylon 6	Not tested/15% nylon 6	0.5-1.25% AgNO ₃ /not tested	Viscosity, conductivity, SEM, TEM, Ag release profile, antibacterial activity	Viable cell-counting method (LB broth and TSA broth)	4 log reduction 0.5% AgNO ₃ 5.8 log reduction 1.25% AgNO ₃ (<i>E. coli</i>) 3.4 log reduction 0.5% AgNO ₃ 3.4 log reduction 1.25% AgNO ₃ 99.99% (<i>B. cereus</i>) 43-77% growth inhibition (<i>S. aureus</i>) 57-77% growth inhibition (<i>K. pneumoniae</i>)	Energy storage, biomedical materials, catalysis, sensors	[41]
4	AgNPs/PVDF	Direct blending method	5.1 nm	600 ± 176 nm	280-676 ppm AgNPs/10-25% PVDF	310-730 ppm AgNPs/10-25% PVDF	280-676 ppm AgNPs/310-730 ppm AgNPs	SEM, TEM, XPS, ICP, viscosity, antibacterial activity	Growth inhibition rate (nutrient broth)	Water filters, wound dressings, or antiadhesion membranes		[7]
5	AgNPs/PAN	UV-irradiation method	2.0 ± 0.6 nm	~400-500 nm	0.1, 0.3, and 0.5 M AgNO ₃ /8% PAN [1 fold:5 fold]	Not tested/8% PAN	0.1, 0.3, and 0.5 M AgNO ₃ /not tested	SEM, XRD, Ag release profile, FTIR, antibacterial activity	Kirby-Bauer Method; disk diffusion test (LB broth)	89.67 ± 1.7% (<i>E. coli</i>) 87.67 ± 4.03% (<i>B. subtilis</i>) 17 mm inhibition zone (<i>E. coli</i>) 18 mm inhibition zone (<i>S. aureus</i>) (nutritive broth)	Water purification, bacterial filtration, biomedical devices	[46]
6	AgNPs/PAN	UV-irradiation method	2-50 nm	~600-900 nm	0.05-1% AgNO ₃ /8% PAN [1 fold:8 fold]	Not tested/8% PAN	0.05-1% AgNO ₃ /not tested	SEM, EDAX, UV-Vis, XRD, AFM, air filtration efficiency test, antibacterial activity	Inhibition zone method (nutrient broth)	Antimicrobial filters		[64]
7	AgNPs/PEBA	UV-irradiation method	13.5-16.5 nm	~100-300 nm	0.05-0.25% AgNO ₃ /5%-2.5% PEBA [1 fold:100 fold]	No tested/5%-2.5% PEBA	0.05-0.25% AgNO ₃ /no tested	TEM-EDS, SEM, DSC, TGA, XPS, antibacterial activity	Pour-plate culture Method (nutrient broth)	99.99% <i>E. coli</i> , <i>S. aureus</i>	Biomedical materials, sports apparatus, and laminating films	[59]

TABLE 1: Continued.

Entry	AgNP electrospun system	Method used	AgNP size	Nanofibers/fiber size	[AgNO ₃]/[polymer]	[loaded AgNPs]/[polymer] % wt.	[AgNO ₃]/[loaded AgNPs]	Characterization	Method (medium used)	Antimicrobial activity (% effectivity)	Applications	Ref.
		<i>Thermal reduction method</i>			1% AgNO ₃ /15% PVA [1 fold:1.5 fold]	2.6% wt, AgNPs/15% PVA	1% AgNO ₃ /2.6% wt, AgNPs	XRD, SEM, TEM, EDS, DLS, XPS, antibacterial activity	Inhibition zones assay	2-fold log reduction (<i>S. aureus</i>), 1.4-fold log reduction (<i>E. coli</i>)	Biological sensors, conductive interconnects, optoelectronic devices, effective bioactive materials	

Materials: AgNPs: silver nanoparticles; CA: cellulose acetate; CE: cellulose; PAN: poly(acrylonitrile); FK: feather keratin; PMMA: poly(methyl methacrylate); PVA: poly(vinyl alcohol); PEO: poly(ethylene oxide); PEBA: poly(ether block amide); P(AN-S): poly(acrylonitrile-co-phenylethylene); STA: silver trifluoroacetate. Assays: AFM: atomic force microscopy; EDAX: energy dispersive X-ray analysis; SEM: scanning electron microscopy; EDX: energy dispersive X-ray spectroscopy; ICP: inductively coupled plasma; TEM: transmission electron microscopy; XRD: X-ray diffraction; XPS: X-ray photoelectron spectroscopy; TGA: thermogravimetric analysis; UV-Vis: ultraviolet-visible light spectroscopy.

3. Antimicrobial Activities of Ag Nanofibers

AgNPs are well known to have antimicrobial bioactivity. This bioactivity occurs through cell membrane damage, free radical generation, and DNA interaction, among others (Figure 5) [71, 72]. One of the proposed mechanisms of AgNP action is the effect on the lipid bilayer induced by the AgNP accumulation in the bacterial cell wall [59]. Thus, membrane permeability increased, causing cell damage and death. Moreover, the effect increases while the AgNP size decreases [73]. Another mechanism suggested for cell death induced by AgNPs is the reaction with thiol groups ($-SH$) of cysteine and phosphorus compounds on the cell wall, affecting respiration and replication processes [59, 74]. Another explanation for the antimicrobial activity is that metal depletion may cause the formation of irregularly shaped pits in the outer membrane and change membrane permeability, which is caused by a progressive release of lipopolysaccharide molecules and membrane proteins [63] (entry 6).

AgNPs or the released silver ions (Ag^+) can also enter the bacterial cells and interact with compounds containing sulfur and phosphorus, preventing DNA replication and inactivating proteins. Besides, they can inhibit the activity of endocellular ATP levels, thereby preventing the cell's respiratory function. Furthermore, AgNPs have been reported to induce the release of reactive oxygen species (ROS), forming free radicals with strong bactericidal effects (Figure 5) [75]. AgNPs have a broad antibacterial spectrum covering aerobic, anaerobic, and Gram amphoteric bacteria [76], low incidence of resistance [77], and sustained antibacterial activity [78], thus have been widely used in antibacterial wound dressings [75].

The antimicrobial activity of AgNPs depends on the surface area of the nanomaterial [72]. The highest concentrations of released Ag^+ ions have been observed from AgNPs with the highest surface area. On the contrary, Ag^+ ion's low release has been found for AgNPs with low surface area, resulting in weak antimicrobial properties [79]. Most electrospun nanofibers do not affect microbial cell reproduction by themselves, but only with the presence of AgNPs. Such is the case of PAN nanofibers which were endowed with excellent antibacterial properties due to the introduction of AgNPs. The authors claim that AgNPs have strong antibacterial properties since they attach to the cell walls and disturb cell-wall permeability and cellular respiration [48] (entry 12).

Poly(vinyl alcohol-co-vinyl acetate)/octadecyl aminemontmorillonite (P(VA-co-VAc)/ODA-MMT) nanofibers loaded with AgNPs showed high antimicrobial activity against fungus (*Candida albicans*, *tropicalis*, *glabrata*, *keyfr*, and *krusei*) and bacteria (*S. aureus* and *E. coli*) [80]. It has been demonstrated that Ag^+ release confers the AgNP microbicidal effect [81–83]. Moreover, the internalization of AgNPs into the fibers permits a longer bioavailability of the silver on the application site because the release of the A^+ ions depends on the time of fiber degradation [84]. This could explain that 10 nm AgNPs were more toxic for *E. coli* than 20–80 nm due to a more efficient cell-particle contact. Thus, AgNP toxicity correlates with size and content because of the Ag^+ initial release rate, affecting the fibrous scaffold

cytotoxicity. However, the AgNP amount also regulates the long-term Ag^+ release rate and, therefore, the microbicidal activity [72, 75].

AgNP-loaded electrospun membranes with antibacterial properties have been tested in food packaging material to delay food spoilage or bacteria contamination [63, 78]. Chaudhary et al. [63] (entry 6) used an electrospun AgNP/PAN composite filter media to cover a nutrient media in room conditions and pass ambient air through the filter media. The nutrient media protected by the nanofibrous filter remained free of bacteria growth after two months, while the unprotected nutrient media show microorganism growth. Taking advantage of the excellent dispersion of AgNPs in electrospun nanofibers, Castro-Mayorga et al. [85] reported electrohydrodynamic processing, which combines the electrospaying and electrospinning techniques to produce a multilayer system comprising a poly(hydroxy alkanate) (PHA) substrate and an electrospun PHA coating containing AgNPs. The materials reduced the *Salmonella enterica* population below the detection limits at a very low silver loading of 0.002% wt.

Table 1 shows the physicochemical and antimicrobial properties of AgNP-nanofiber systems prepared by the discussed methods. It can be observed that each of the four methods affects the resulted size of the incorporated AgNPs. Moreover, small particle sizes (<10 nm) can be achieved in all methods.

It should be noted that the data in Table 1 include the following: (1) inhibition zone diameter, which may not be comparable, or (2) results of distinct AgNP concentrations leading to approximately 100% inhibition of microorganism growth, which is also not representative. In the future, the minimal inhibitory concentration (MIC) and the inhibitory concentration (IC_{50}) should be presented as data; moreover, for this purpose, the microdilution test to evaluated antimicrobial activity should be used [37].

Also, it can be appreciated that information about the resulting AgNP size is not reported in some articles. The antimicrobial results are reported in different ways, making it difficult to compare studies.

4. Comparisons among Methods of Incorporation of AgNPs

Metal nanoparticles tend to aggregate in the polymer matrix during nanofiber formation, highlighting the need for new and better methods that allow better metal nanoparticle dispersion on the polymer nanofiber matrix [42] (entry 3). Another requirement is to reduce the number of reaction steps and reduce the use of toxic chemical agents to form AgNP/composite polymeric scaffolds. The search for a facile and ecofriendly method is an important task [86]. There is not a noticeable difference in AgNP size and antimicrobial activity for the studied methods; they all reported similar results (Tables 1 and 2). Hence, in our further discussion, we can focus on finding the method possessing the most advantages other than appropriate AgNP size.

Among the compared methods, the *direct blending method* is the easiest, more accessible, and most commonly

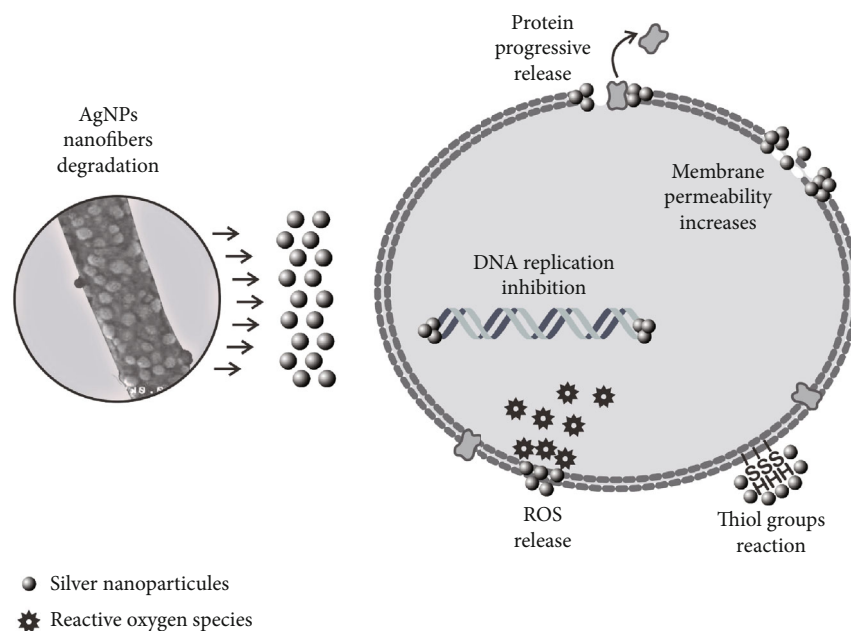


FIGURE 5: AgNP release from nanofibers and mechanisms of action of AgNPs on microbial cells.

used technique to incorporate AgNPs into nanofiber mats [35, 55]. It has been reported that the electrospinning conditions do not affect AgNP bioactivity on microbial cells; however, fiber-matrix encapsulation could reduce it [87]. Despite that, the lack of chemical treatment, irradiation, and thermal treatment made the direct blending method preferable compare to others that consume more time and energy [42] (entry 3). However, it has been described that the mechanical mixing of the AgNPs with the polymeric solution by the *direct blending method* affects the homogeneity of particle dispersion, facilitating their aggregation, increase viscosity of the polymeric solution, which increase the surface tension, complicating nanofiber formation [66] (entry 13).

Otherwise, comparing the *UV-irradiation method* with the *direct blending*, an initial burst release of the AgNPs incorporated into the nanofibers is observed only in the UV method. As mentioned above, this burst release was attributed to the silver ion's migration from the core to the nanofiber surface [45]. Moreover, in the *UV-reduction method*, the AgNP diameters are smaller with narrower distribution than other methods. In its turn, the size of AgNPs is an essential parameter of antimicrobial activity [62] (entries 8 and 16). AgNP/PVA nanofibers prepared by the UV irradiation method showed more effectivity against *S. aureus* than those prepared by the *thermal reduction method*. In the first case, after 30 minutes of incubation, no bacterial colonies were detected. In comparison, microbial colonies were detected in both treated and untreated AgNP/PVA scaffolds. The authors discussed the last result is ascribed to a higher dispersion diameter resulted from the AgNO_3 reduction from the thermal treatment in the PVA samples [62] (entries 8 and 16).

In the thermal reduction method, the size and spatial distribution of AgNPs can be tuned by varying the AgNO_3 solution concentration. The strategy to immobilizing and manipulating the size of the AgNPs on polymer nanofibers

may be extended to other particle systems for various applications such as catalysis, energy, sensing, photonic, and biomedical applications [88]. Unfortunately, this method has been observed that leaching of AgNPs in the initial stage can occur [62] (entries 8 and 16). However, UV irradiation prepared AgNPs are preferred over those loaded on electrospun poly(vinyl alcohol) (PVA) by heat treatment of AgNO_3 for its cytotoxic and microbicidal properties.

The *silver mirror reaction method* produces different morphologies of Ag nanostructures (quasispheres, wires, rod, right bipyramid, beam, spheres, cube, and octahedron) which cannot be predefined [66], limiting its use for the synthesis of a particular Ag nanostructure. However, to our knowledge, none of the methods compared in this review allow us to design the nanostructure. On the other hand, the *silver mirror reaction method* is easily controlled, and it takes place at ambient conditions but requires further processing (filtration, purification, and washing) [64] (entry 13). Nanofiber morphology has no significant differences if prepared by SMR or the *thermal reduction method* [47].

Hence, from the above analysis, we can conclude that all four considered methods presented difficulties in loading AgNPs into the nanofibers, but this does not impact the antimicrobial effectivity of the nanofiber/nanoparticle systems (Table 2). It would be interesting to compare the concentration of AgNO_3 is used and how much Ag is loaded. Still, at the moment, several studies do not evaluate the Ag loaded on the nanofibers, which does not allow to do these correlations.

5. Future Perspectives and Limitations

The properties as porosity, a high surface area/volume ratio, and porous interconnection that can be reached with electrospun polymeric nanofibers make them attractive in different

TABLE 2: Comparison of advantages and disadvantages of the methods for incorporation AgNPs in electrospun nanofibers.

Method	Advantage	Disadvantage	Ref.
<i>Direct blending method</i>	(i) Single-step process (ii) Polymeric solution is the reducing agent (iii) Tiny particle sizes obtained <10 nm (iv) Faster and simpler than other compared methods	(i) Stabilizing and protection agents are used to avoiding NP aggregation (ii) Posttreatment needed (purification, extractions, etc.) (iii) Lacking size homogeneity in dense matrices	[42, 64]
<i>UV-irradiation method</i>	(i) Not necessarily extra time in polymeric solution preparation (ii) No additional solvents are required (iii) Tiny particle sizes obtained <10 nm	(i) Limited to the use of UV-sensitive polymers (ii) Not recommendable the use irradiation greater than 380 nm (polymer degradation) (iii) Extra UV irradiation treatment (~3-24 h) (iv) When the irradiation time is prolonged, even though the formation of nanoparticles increases, the size also increases	[44–46, 60–62]
<i>Silver mirror reaction method</i>	(i) The reaction is at room temperature (ii) Facilitate the surface coating of big devices (iii) Coating of micro- and nanostructures such as nanofibers (iv) Formation of smooth coatings (v) Easy control (vi) The reducing agent can vary (vii) Tiny particle sizes obtained <10 nm	(i) The high volume of the reaction (ii) Posttreatments needed (purification, filtration; washing, vacuum drying) (iii) 2.5 h posttreatment after electrospinning (iv) Use of surfactants for stabilizing nanostructures (v) 12 h for solution preparation	[64, 66]
<i>Thermal reduction method</i>	(i) Easy to perform (ii) Uniform distribution of loaded AgNPs on the fibers (iii) Size and distribution of the AgNPs are controllable with the time and temperature applied (iv) Very small particle sizes obtained <10 nm	(i) Extra thermal irradiation treatment (~1-12 h) (ii) Limited to stable polymers at temperatures above 100°C (polyesters, natural polymers) (iii) Leaching of AgNPs	[47, 62, 70]

fields [89]. Thus, in the last years, applications for filtering, tissue engineering, wound dressing, drug delivery, and biosensors have been reported using electrospun nanofibers with inorganic particles [90]. However, several variables affect the electrospinning process. Such variables are not yet fully described [48].

The electrospinning method is also limited for parameters that have to be optimized. For example, the large-scale production may present polymer blockage, and electrospinning flux may alter the electric field. It has been reported that this can be fixed using a multirow component in the injection system [91]. Also, it is desired to control nanofiber thickness with collecting devices with different characteristics [9], such as centrifugal electrospinning, or surface-free systems [92]. Other improvement points are precision and reproducibility; for those, the control of temperature and humidity is essential [9]. Finally, stability and mechanical properties can be upgraded with new electrospinning formulations [92–94].

The microbicidal effect of silver has been related to Ag⁺ ion interaction with the cell membrane. It has been described that in AgNPs, Gram-negative bacteria inhibition depends on the concentration associated with cell wall damage [63], but a precise mechanism is still unknown. Still, more studies

have to be implemented to investigate the mechanism of the antimicrobial action of the AgNPs. Most importantly, it is necessary to develop the ideal method that does not present any of the troubles mentioned in this review.

The literature data analysis made in the present review indicates that at the present moment, there are numerous publications dedicated to the application of different methods of deposition of AgNPs on nanofibrous scaffolds. Nevertheless, these results are not enough to conclude which method is the most promising for the best control of Ag⁺ ion release. Research where all methods are applied in similar experimental conditions (the same silver nanoparticles type, including stabilizer, particle size, hydrodynamic diameter, and Ag concentration) is necessary to carry out to answer this question.

6. Conclusions

The analysis carried out in this work showed that the methods of AgNP incorporation into the electrospun nanofibers could alter the size of AgNPs, their distribution on the electrospun nanofibers, and their antimicrobial activity. The differences among the four analyzed methods also come from

the incorporation time, method difficulty, complexity, and cost of the equipment and solvents used. The latter is not determined by the technique but by the selected nanofiber polymer. Until now, polyacrylonitrile nanofibers are the most frequently chosen system.

We found that the preferred methods are *direct blending* and *UV irradiation*. The other two methods (*silver mirror reaction* and *thermal reduction*) are less used and less studied. It was found that the *UV treatment* and *thermal reduction methods* can manipulate the size and concentration of AgNPs by varying the time of exposition. The *direct blending* and *silver mirror reaction* methods cannot control the AgNPs size, and small-sized AgNPs can be incorporated. The silver mirror reaction method's advantage is that it is a unique technique that can cover large surfaces with AgNPs.

On the other hand, taking into account the presented data, it is proposed that the best method to control the release of Ag⁺ ions from the nanofibrous scaffolds is the SMR method because it already reported that the UV treatment and thermal reduction methods presented a leaching phenomenon after the AgNP loading on the fibers. In the case of the direct blending method, agglomerations of the AgNPs occur affecting controlled release. Moreover, the SRM method provides a homogeneous and well-defined distribution where the AgNP release can be controlled by optimizing the polymeric nanofiber's degradation.

Conjugation of well-known antimicrobial activity of AgNPs with electrospun nanofibers could take AgNP antimicrobial properties to their highest efficiency. However, up to now, the antimicrobial efficiency of AgNP-loaded nanofibers has not been explored thoughtfully. The mechanisms of antimicrobial action of AgNPs still need to be addressed. Finally, it is recommended to accompany the future performance of four methods discussed here with a comprehensive determination of physicochemical and antimicrobial characteristics of obtained AgNP-loaded nanofibers. This will allow making a more objective comparison of these methods.

Conflicts of Interest

The authors declare that there is no conflict of interest regarding the publication of this paper.

Acknowledgments

The team of Research Institute of Clinical and Experimental Lymphology—Branch of the Institute of Cytology and Genetics, Siberian Branch of Russian Academy of Sciences thanks to the Ministry of Education and Science of Russia (theme No. 0324-2019-0046). Dr. Alexey Pestryakov thanks Tomsk Polytechnic University Task Program “Science” project FSWW-2020-0011 and Sevastopol State University Task Program “Science” project No. FEFM-2020-0003 and Research grant 42-01-09/169/2021-4.

References

[1] H. Soliman, A. Elsayed, and A. Dyaa, “Antimicrobial activity of silver nanoparticles biosynthesised by *Rhodotorulasp.* strain

ATL72,” *Egyptian Journal of Basic and Applied Sciences*, vol. 5, no. 3, pp. 228–233, 2018.

- [2] M. Akter, M. T. Sikder, M. M. Rahman et al., “A systematic review on silver nanoparticles-induced cytotoxicity: physicochemical properties and perspectives,” *Journal of Advanced Research*, vol. 9, pp. 1–16, 2018.
- [3] H. Singh, J. Du, P. Singh, and T. H. Yi, “Extracellular synthesis of silver nanoparticles by *Pseudomonas* sp. THG-LS1.4 and their antimicrobial application,” *Journal of Pharmaceutical Analysis*, vol. 8, no. 4, pp. 258–264, 2018.
- [4] R. Kalaivani, M. Maruthupandy, T. Muneeswaran et al., “Synthesis of chitosan mediated silver nanoparticles (Ag NPs) for potential antimicrobial applications,” *Frontiers in Laboratory Medicine*, vol. 2, no. 1, pp. 30–35, 2018.
- [5] M. Behravan, A. Hossein Panahi, A. Naghizadeh, M. Ziaee, R. Mahdavi, and A. Mirzapour, “Facile green synthesis of silver nanoparticles using *Berberis vulgaris* leaf and root aqueous extract and its antibacterial activity,” *International Journal of Biological Macromolecules*, vol. 124, pp. 148–154, 2019.
- [6] S. Gurunathan, “Rapid biological synthesis of silver nanoparticles and their enhanced antibacterial effects against *Escherichia fergusonii* and *Streptococcus mutans*,” *Arabian Journal of Chemistry*, vol. 12, no. 2, pp. 168–180, 2019.
- [7] C. S. Nunes and P. Philipps-Wiemann, “Chapter 22 - formulation of enzymes,” in *Enzymes in Human and Animal Nutrition Principles and Perspectives*, C. S. Nunes and B. T. Vikas, Eds., Academic Press, Versailles, France, 1st ed. edition, 2018.
- [8] F. Khalili Amand and A. Esmaeili, “Investigating the properties of electrospun nanofibers made of hybriide polymer containing anticoagulant drugs,” *Carbohydrate Polymers*, vol. 228, p. 115397, 2020.
- [9] J. Quirós, K. Boltes, and R. Rosal, “Bioactive applications for electrospun fibers,” *Polymer Reviews*, vol. 56, no. 4, pp. 631–667, 2016.
- [10] V. Agarwal, D. Ho, D. Ho et al., “Functional reactive polymer electrospun matrix,” *ACS Applied Material and Interfaces*, vol. 8, no. 7, pp. 4934–4939, 2016.
- [11] M. Wang, T. Hai, Z. Feng, D.-G. Yu, Y. Yang, and S. W. Annie Bligh, “The relationships between the working fluids, process characteristics and products from the modified coaxial electrospinning of zein,” *Polymers*, vol. 11, no. 8, p. 1287, 2019.
- [12] L. D. Ghosh, A. Jain, N. R. Sundaresan, and K. Chatterjee, “Elucidating molecular events underlying topography mediated cardiomyogenesis of stem cells on 3D nanofibrous scaffolds,” *Materials Science and Engineering: C*, vol. 88, pp. 104–114, 2018.
- [13] V. Agarwal, F. M. Wood, F. Mark, and I. K. Swaminathan, “Polymeric nanofibre scaffold for the delivery of a transforming growth factor β 1 inhibitor,” *Australian Journal of Chemistry*, vol. 70, pp. 280–285, 2017.
- [14] A. Jain, M. Behera, V. Ravi, S. Mishra, N. R. Sundaresan, and K. Chatterjee, “Recapitulating pathophysiology of skeletal muscle diseases *in vitro* using primary mouse myoblasts on a nanofibrous platform,” *Nanomedicine: Nanotechnology, Biology and Medicine*, vol. 32, article 102341, 2021.
- [15] S. Sankar, C. S. Sharma, S. N. Rath, and S. Ramakrishna, “Electrospun nanofibres to mimic natural hierarchical structure of tissues: application in musculoskeletal regeneration,” *Journal of Tissue Engineering and Regenerative Medicine*, vol. 12, pp. e604–e619, 2018.

- [16] G. Sandri, S. Rossi, M. C. Bonferoni, C. Caramella, and F. Ferrari, *Technologies in Wound Dressing Applications. In Therapeutic Dressings and Wound Healing Applications*, J. Boateng, Ed., Wiley, United Kingdom, 2020.
- [17] S. R. K. Meka, S. Kumar Verma, V. Agarwal, K. Chatterjee, and K. Chatterjee, "In situ silication of polymer nanofibers to engineer multi-biofunctional composites," *Chemistry Select*, vol. 3, no. 13, pp. 3762–3773, 2018.
- [18] S. Sankar, C. S. Sharma, S. N. Rath, and S. Ramakrishna, "Electrospun fibers for recruitment and differentiation of stem cells in regenerative medicine," *Biotechnology Journal*, vol. 12, no. 12, article 1700263, 2017.
- [19] L. J. Villarreal-Gómez, R. Vera-Graziano, M. R. Vega-Ríos et al., "Biocompatibility evaluation of electrospun scaffolds of poly (L-lactide) with pure and grafted hydroxyapatite," *Journal of the Mexican Chemical Society*, vol. 58, no. 4, pp. 435–443, 2017.
- [20] L. J. Villarreal-Gómez, J. M. Cornejo-Bravo, R. Vera-Graziano, and D. Grande, "Electrospinning as a powerful technique for biomedical applications: a critically selected survey," *Journal of Biomaterials Science, Polymer Edition*, vol. 27, no. 2, pp. 157–176, 2016.
- [21] E. J. Torres-Martínez, J. M. Cornejo Bravo, A. Serrano Medina, G. L. Pérez González, and L. J. Villarreal Gómez, "A summary of electrospun nanofibers as drug delivery system: drugs loaded and biopolymers used as matrices," *Current Drug Delivery*, vol. 15, no. 10, pp. 1360–1374, 2018.
- [22] G. L. Pérez-González, L. J. Villarreal-Gómez, A. Serrano-Medina, E. J. Torres-Martínez, and J. M. Cornejo-Bravo, "Mucoadhesive electrospun nanofibers for drug delivery systems: applications of polymers and the parameters' roles," *International Journal of Nanomedicine*, vol. Volume 14, no. 1, pp. 5271–5285, 2019.
- [23] E. J. Torres-Martínez, G. L. Pérez-González, A. Serrano-Medina et al., "Drugs loaded into electrospun polymeric nanofibers for delivery," *Journal of Pharmacy and Pharmaceutical Sciences*, vol. 22, no. 1, pp. 313–331, 2019.
- [24] G. L. Pérez-González, L. J. Villarreal-Gómez, A. Olivares-Sarabia, R. Valdez, and J. M. Cornejo-Bravo, "Development, characterization, and in vitro assessment of multilayer mucoadhesive system containing dexamethasone sodium phosphate," *International Journal of Polymeric Materials and Polymeric Biomaterials*, vol. 1, pp. 1–13, 2020.
- [25] A. Macagnano and F. De Cesare, "17 - Electrospinning: a versatile technology to design biosensors and sensors for diagnostics," in *Electrospun Materials for Tissue Engineering and Biomedical Applications*, T. Uyar and B. T. Erich, Eds., Woodhead Publishing, 2017, *Electrospun Materials for Tissue Engineering and Biomedical Applications* Kny.
- [26] E. Sapountzi, M. Braiek, J.-F. Chateaux, N. Jaffrezic-Renault, and F. Lagarde, "Recent advances in electrospun nanofiber interfaces for biosensing devices," *Sensors*, vol. 17, no. 8, p. 1887, 2017.
- [27] H.-G. Wang, S. Yuan, D.-L. Ma, X.-B. Zhang, and J.-M. Yan, "Electrospun materials for lithium and sodium rechargeable batteries: from structure evolution to electrochemical performance," *Energy and Environmental Science*, vol. 8, no. 6, pp. 1660–1681, 2015.
- [28] J. G. López-Covarrubias, L. Soto-Muñoz, A. L. Iglesias, and L. J. Villarreal-Gómez, "Electrospun nanofibers applied to dye solar sensitive cells: a review," *Materials*, vol. 12, no. 19, p. 3190, 2019.
- [29] I. Tlili and T. A. Alkanhal, "Nanotechnology for water purification: electrospun nanofibrous membrane in water and wastewater treatment," *Journal of Water Reuse and Desalination*, vol. 9, no. 3, pp. 232–248, 2019.
- [30] H. Chen, M. Huang, Y. Liu, L. Meng, and M. Ma, "Functionalized electrospun nanofiber membranes for water treatment: a review," *Science of the Total Environment*, vol. 739, article 139944, 2020.
- [31] B. M. Sollier, M. Bonne, N. Khenoussi et al., "Synthesis and characterization of electrospun nanofibers of Sr-La-Ce oxides as catalysts for the oxidative coupling of methane," *Industrial & Engineering Chemistry Research*, vol. 59, no. 25, pp. 11419–11430, 2020.
- [32] S. Wen, M. Liang, R. Zou, Z. Wang, D. Yue, and L. Liu, "Electrospinning of palladium/silica nanofibers for catalyst applications," *RSC Advances*, vol. 5, no. 52, pp. 41513–41519, 2015.
- [33] B. Ding, M. Wang, X. Wang, J. Yu, and G. Sun, "Electrospun nanomaterials for ultrasensitive sensors," *Materials Today*, vol. 13, no. 11, pp. 16–27, 2010.
- [34] N. Aliheidari, N. Aliahmad, M. Agarwal, and H. Dalir, "Electrospun nanofibers for label-free sensor applications," *Sensors*, vol. 19, no. 16, p. 3587, 2019.
- [35] J. Yuan, J. Geng, Z. Xing, J. Shen, I.-K. Kang, and H. Byun, "Electrospinning of antibacterial poly (vinylidene fluoride) nanofibers containing silver nanoparticles," *Journal of Applied Polymer Science*, vol. 116, no. 2, pp. 668–672, 2009.
- [36] S. Ren, L. Dong, X. Zhang et al., "Electrospun nanofibers made of silver nanoparticles, cellulose nanocrystals, and polyacrylonitrile as substrates for surface-enhanced raman scattering," *Materials (Basel, Switzerland)*, vol. 10, no. 1, p. 68, 2017.
- [37] A. S. Álvarez-Suárez, S. G. Dastager, N. Bogdanchikova et al., "Electrospun fibers and sorbents as a possible basis for effective composite wound dressings," *Micromachines*, vol. 11, no. 4, p. 441, 2020.
- [38] K. E. M. C. K, B. P, T. S. A, and J. C. R. I, "Biocompatible silver nanoparticles/poly(vinyl alcohol) electrospun nanofibers for potential antimicrobial food packaging applications," *Food Packaging and Shelf Life*, vol. 21, article 100379, 2019.
- [39] A. C. Canalli Bortolassi, V. G. Guerra, M. L. Aguiar et al., "Composites based on nanoparticle and pan electrospun nanofiber membranes for air filtration and bacterial removal," *Nanomaterials*, vol. 9, no. 12, p. 1740, 2019.
- [40] J. Wang, L. Zhan, X. Zhang, R. Wu, L. Liao, and J. Wei, "Silver nanoparticles coated poly(L-lactide) electrospun membrane for implant associated infections prevention," *Frontiers in Pharmacology*, vol. 11, pp. 1–8, 2020.
- [41] S. Jin, J. Li, J. Wang et al., "Electrospun silver ion-loaded calcium phosphate/chitosan antibacterial composite fibrous membranes for guided bone regeneration," *International Journal of Nanomedicine*, vol. Volume 13, pp. 4591–4605, 2018.
- [42] Q. Shi, N. Vitichuli, J. Nowak et al., "One-step synthesis of silver nanoparticle-filled nylon 6 nanofibers and their antibacterial properties," *Journal of Materials Chemistry*, vol. 21, no. 28, pp. 10330–10335, 2011.
- [43] A. W. Jatoti, Y. K. Jo, H. Lee et al., "Antibacterial efficacy of poly(vinyl alcohol) composite nanofibers embedded with silver-anchored silica nanoparticles," *Journal of Biomedical Materials Research Part B: Applied Biomaterials*, vol. 106, no. 3, pp. 1121–1128, 2018.

- [44] W. K. Son, J. H. Youk, and W. H. Park, "Antimicrobial cellulose acetate nanofibers containing silver nanoparticles," *Carbohydrate Polymers*, vol. 65, no. 4, pp. 430–434, 2006.
- [45] P.-o. Rujitanaroj, N. Pimpha, and P. Supaphol, "Preparation, characterization, and antibacterial properties of electrospun polyacrylonitrile fibrous membranes containing silver nanoparticles," *Journal of Applied Polymer Science*, vol. 116, no. 4, pp. 1967–1976, 2010.
- [46] D.-N. Phan, N. Dorjjugder, Y. Saito et al., "The synthesis of silver-nanoparticle-anchored electrospun polyacrylonitrile nanofibers and a comparison with as-spun silver/polyacrylonitrile nanocomposite membranes upon antibacterial activity," *Polymer Bulletin*, vol. 77, no. 8, pp. 4197–4212, 2020.
- [47] A. W. Jatoi, I. S. Kim, and Q. Q. Ni, "A comparative study on synthesis of AgNPs on cellulose nanofibers by thermal treatment and DMF for antibacterial activities," *Materials Science and Engineering: C*, vol. 98, pp. 1179–1195, 2019.
- [48] Y. Shi, Y. Li, J. Zhang, Z. Yu, and D. Yang, "Electrospun polyacrylonitrile nanofibers loaded with silver nanoparticles by silver mirror reaction," *Materials Science and Engineering: C*, vol. 51, pp. 346–355, 2015.
- [49] D. Kharaghani, H. Lee, T. Ishikawa, T. Nagaishi, S. H. Kim, and I. S. Kim, "Comparison of fabrication methods for the effective loading of Ag onto PVA nanofibers," *Textile Research Journal*, vol. 89, no. 4, pp. 625–634, 2019.
- [50] P. Li, M. Zhang, X. Liu, Z. Su, and G. Wei, "Electrostatic assembly of platinum nanoparticles along electrospun polymeric nanofibers for high performance electrochemical sensors," *Nanomaterials*, vol. 7, no. 9, p. 236, 2017.
- [51] A. C. C. Bortolassi, S. Nagarajan, B. de Araújo Lima et al., "Efficient nanoparticles removal and bactericidal action of electrospun nanofibers membranes for air filtration," *Materials Science and Engineering: C*, vol. 102, pp. 718–729, 2019.
- [52] E. A. Skomorokhova, T. P. Sankova, I. A. Orlov et al., "Size-dependent bioactivity of silver nanoparticles: antibacterial properties, influence on copper status in mice, and whole-body turnover," *Nanotechnology, Science and Applications*, vol. 13, pp. 137–157, 2020.
- [53] Q. Shi, N. Vitichuli, J. Nowak et al., "Durable antibacterial Ag/polyacrylonitrile (Ag/PAN) hybrid nanofibers prepared by atmospheric plasma treatment and electrospinning," *European Polymer Journal*, vol. 47, no. 7, pp. 1402–1409, 2011.
- [54] Z. Xu, S. Mahalingam, J. L. Rohn, G. Ren, and M. Edirisinghe, "Physio-chemical and antibacterial characteristics of pressure spun nylon nanofibres embedded with functional silver nanoparticles," *Materials Science and Engineering C*, vol. 56, pp. 195–204, 2015.
- [55] Y. Gao, Y. Bach Truong, Y. Zhu, and I. Louis Kyratzis, "Electrospun antibacterial nanofibers: production, activity, and in vivo applications," *Journal of Applied Polymer Science*, vol. 131, no. 18, pp. 9041–9053, 2014.
- [56] S. K. Bhullar, D. G. Ruzgar, G. Fortunato et al., "A facile method for controlled fabrication of hybrid silver nanoparticle-poly(ϵ -caprolactone) fibrous constructs with antimicrobial properties," *Journal of Nanosciences and Nanotechnology*, vol. 19, no. 11, pp. 6949–6955, 2019.
- [57] R. Wang, Z. Wang, S. Lin et al., "Green fabrication of antibacterial polymer/silver nanoparticle nanohybrids by dual-spinneret electrospinning," *RSC Advances*, vol. 5, no. 50, pp. 40141–40147, 2015.
- [58] N. Tucker, K. Hofman, J. Stanger, M. Staiger, N. A. Hamid, and P. L. Torres, "The history of the science and technology of electrospinning from 1600 to 1995," in *International Symposium on New Frontiers in Fiber Materials Science, Conference Proceedings*, pp. 63–73, Charleston, South Carolina, USA, 2011.
- [59] M. He, M. Chen, Y. Dou et al., "Electrospun silver nanoparticles-embedded feather Keratin/Poly(vinyl alcohol)/Poly(ethylene oxide) antibacterial composite nanofibers," *Polymers*, vol. 12, no. 2, p. 305, 2020.
- [60] T. Nuge, K. Y. Tshai, S. S. Lim, N. Nordin, and M. E. Hoque, "Preparation and characterization of CU-, FE-, AG-, ZN- and NI- doped gelatin nanofibers for possible applications in antibacterial nanomedicine," *Journal of Engineering Science and Technology*, vol. 12, no. 1, pp. 68–81, 2017.
- [61] S. Liang, G. Zhang, J. Min, J. Ding, and X. Jiang, "Synthesis and antibacterial testing of silver/poly(ether amide) composite nanofibers with ultralow silver content," *Journal of Nanomaterials*, vol. 2014, Article ID 684251, 10 pages, 2014.
- [62] S. Lin, R. Z. Wang, Y. Yi et al., "Facile and green fabrication of electrospun poly(vinyl alcohol) nanofibrous mats doped with narrowly dispersed silver nanoparticles," *International Journal of Nanomedicine*, vol. 9, no. 1, pp. 3937–3947, 2014.
- [63] A. Chaudhary, A. Gupta, R. B. Mathur, and S. R. Dhakate, "Effective antimicrobial filter from electrospun polyacrylonitrile-silver composite nanofibers membrane for Conductive Environments," *Advanced Materials Letters*, vol. 5, no. 10, pp. 562–568, 2014.
- [64] D. Y. Lee, K.-H. Lee, B.-Y. Kim, and N.-I. Cho, "Silver nanoparticles dispersed in electrospun polyacrylonitrile nanofibers via chemical reduction," *Journal of Sol-Gel Science and Technology*, vol. 54, no. 1, pp. 63–68, 2010.
- [65] Y. Liu, D. Chunnuan, X. Lv, Z. Jia, S. Sun, and Y. Jianxiang, "Synthesis of silver nanofiber transparent electrodes by silver mirror reaction with electrospun nanofiber template," *Composite Interfaces*, vol. 26, pp. 1–10, 2021.
- [66] M. Rycenga, C. M. Cobley, J. Zeng et al., "Controlling the synthesis and assembly of silver nanostructures for plasmonic applications," *Chemical Reviews*, vol. 111, no. 6, pp. 3669–3712, 2011.
- [67] C. Chen, Y. Tang, B. Vlahovic, and F. Yan, "Electrospun polymer nanofibers decorated with noble metal nanoparticles for chemical sensing," *Nanoscale Research Letters*, vol. 12, no. 1, p. 451, 2017.
- [68] M. W. Munir and U. Ali, "Classification of electrospinning methods," in *Nanorods and Nanocomposites*, M. S. Ghamsari and S. Dhara, Eds., IntechOpen, 1st ed. edition, 2020.
- [69] C.-N. Lok, C.-M. Ho, R. Chen et al., "Silver nanoparticles: partial oxidation and antibacterial activities," *JBIC Journal of Biological Inorganic Chemistry*, vol. 12, no. 4, pp. 527–534, 2007.
- [70] H.-T. Chen, H.-L. Lin, I.-G. Chen, and C. Kuo, "Conducting silver networks based on electrospun Poly(Methyl methacrylate) and silver trifluoroacetate," *ACS Applied Materials & Interfaces*, vol. 7, no. 18, pp. 9479–9485, 2015.
- [71] A. Kędziora, M. Speruda, E. Krzyżewska, J. Rybka, A. Łukowiak, and G. Bugła-Płoskońska, "Similarities and differences between silver ions and silver in nanoforms as antibacterial agents," *International Journal of Molecular Sciences*, vol. 19, no. 2, p. 444, 2018.

- [72] N. Durán, M. Durán, M. B. de Jesus, A. B. Seabra, W. J. Fávaro, and G. Nakazato, "Silver nanoparticles: a new view on mechanistic aspects on antimicrobial activity," *Nanomedicine: Nanotechnology, Biology, and Medicine*, vol. 12, no. 3, pp. 789–799, 2016.
- [73] T. C. Dakal, A. Kumar, R. S. Majumdar, and V. Yadav, "Mechanistic basis of antimicrobial actions of silver nanoparticles," *Frontiers in Microbiology*, vol. 7, pp. 1–17, 2016.
- [74] S. Zhang, Y. Tang, and B. Vlahovic, "A review on preparation and applications of silver-containing nanofibers," *Nanoscale Research Letters*, vol. 11, no. 1, pp. 80–88, 2016.
- [75] H. Lv, S. Cui, Q. Yang et al., "AgNPs-incorporated nanofiber mats: relationship between AgNPs size/content, silver release, cytotoxicity, and antibacterial activity," *Materials Science and Engineering C*, vol. 118, p. 111331, 2021.
- [76] B. Le Ouay and F. Stellacci, "Antibacterial activity of silver nanoparticles: a surface science insight," *Nano Today*, vol. 10, no. 3, pp. 339–354, 2015.
- [77] D. Liang, Z. Lu, H. Yang, J. Gao, and R. Chen, "Novel asymmetric wettable AgNPs/chitosan wound dressing: in vitro and in vivo evaluation," *ACS Applied Materials & Interfaces*, vol. 8, no. 6, pp. 3958–3968, 2016.
- [78] D. Kharaghani, Y. Kee Jo, M. Q. Khan, Y. Jeong, H. J. Cha, and I. S. Kim, "Electrospun antibacterial polyacrylonitrile nanofiber membranes functionalized with silver nanoparticles by a facile wetting method," *European Polymer Journal*, vol. 108, pp. 69–75, 2018.
- [79] K. Zawadzka, K. Kaździoła, A. Felczak et al., "Surface area or diameter - which factor really determines the antibacterial activity of silver nanoparticles grown on TiO₂ coatings?," *New Journal of Chemistry*, vol. 38, no. 7, pp. 3275–3281, 2014.
- [80] Z. M. O. Rzayev, D. Erdönmez, K. Erkan, M. Şimşek, and U. Bunyatova, "Functional copolymer/organo-MMT nanoarchitectures. XXII. Fabrication and characterization of antifungal and antibacterial poly vinyl alcohol-co-vinyl acetate/ODA-MMT/AgNPs nanofibers and nanocoatings by e-spinning and c-spinning methods," *International Journal of Polymeric Materials and Polymeric Biomaterials*, vol. 64, no. 5, pp. 267–278, 2015.
- [81] A. Ivask, A. ElBadawy, C. Kaweeteerawat et al., "Toxicity mechanisms in Escherichia coli vary for silver nanoparticles and differ from ionic silver," *ACS Nano*, vol. 8, no. 1, pp. 374–386, 2014.
- [82] A. Ivask, I. Kurvet, K. Kasemets et al., "Size-dependent toxicity of silver nanoparticles to bacteria, yeast, algae, crustaceans and mammalian cells in vitro," *PLoS One*, vol. 9, no. 7, article e102108, 2014.
- [83] H. Palza, "Antimicrobial polymers with metal nanoparticles," *International Journal of Molecular Sciences*, vol. 16, no. 1, pp. 2099–2116, 2015.
- [84] I. L. Hsiao, Y. K. Hsieh, C. F. Wang, I. C. Chen, and Y. J. Huang, "Trojan-horse mechanism in the cellular uptake of silver nanoparticles verified by direct intra- and extracellular silver speciation analysis," *Environmental Science and Technology*, vol. 49, no. 6, pp. 3813–3821, 2015.
- [85] J. L. Castro-Mayorga, M. J. Fabra, L. Cabedo, and J. M. Lagaron, "On the use of the electrospinning coating technique to produce antimicrobial polyhydroxyalkanoate materials containing in situ-stabilized silver nanoparticles," *Nanomaterials*, vol. 7, no. 1, p. 4, 2017.
- [86] B. Pant, M. Park, and S. J. Park, "One-step synthesis of silver nanoparticles embedded polyurethane nano-fiber/net structured membrane as an effective antibacterial medium," *Polymers*, vol. 11, no. 7, p. 1185, 2019.
- [87] S. Zohoori, L. Karimi, and S. Ayaziyazdi, "A novel durable photoactive nylon fabric using electrospun nanofibers containing nanophotocatalysts," *Journal of Industrial and Engineering Chemistry*, vol. 20, no. 5, pp. 2934–2938, 2014.
- [88] S. Xiao, W. Xu, H. Ma, and X. Fang, "Size-tunable Ag nanoparticles immobilized in electrospun nanofibers: synthesis, characterization, and application for catalytic reduction of 4-nitrophenol," *RSC Advances*, vol. 2, no. 1, pp. 319–327, 2012.
- [89] J. Xue, J. Xie, W. Liu, Y. Xia, and D. Holland, "Electrospun nanofibers: new concepts, materials, and applications," *Accounts of Chemical Research*, vol. 50, no. 8, pp. 1976–1987, 2017.
- [90] S. Yu and N. V. Myung, "Minimizing the diameter of electrospun polyacrylonitrile (PAN) nanofibers by design of experiments for electrochemical application," *Electroanalysis*, vol. 30, no. 10, pp. 2330–2338, 2018.
- [91] J. Lev, M. Holba, M. Došek, L. Kalhotka, P. Mikula, and D. Kimmer, "A novel electrospun polyurethane nanofiber membrane – production parameters and suitability for wastewater (WW) treatment," *Water Science and Technology*, vol. 69, no. 7, pp. 1496–1501, 2014.
- [92] G. G. Chase, J. S. Varabhas, and D. H. Reneker, "New methods to electrospin nanofibers," *Journal of Engineered Fibers and Fabrics*, vol. 6, no. 3, pp. 32–38, 2011.
- [93] R. Sridhar, S. Sundarajan, A. Vanangamudi, G. Singh, T. Matsuura, and S. Ramakrishna, "Green processing mediated novel polyelectrolyte nanofibers and their antimicrobial evaluation," *Macromolecular Materials and Engineering*, vol. 299, no. 3, pp. 283–289, 2014.
- [94] B. Pant, M. Park, G. P. Ojha, D.-U. Kim, H.-Y. Kim, and S.-J. Park, "Electrospun salicylic acid/polyurethane composite nanofibers for biomedical applications," *International Journal of Polymeric Materials and Polymeric Biomaterials*, vol. 67, no. 12, pp. 739–744, 2018.

Corrigendum

Corrigendum to “Effects of Arsenic Trioxide-Loaded PLGA Nanoparticles on Proliferation and Migration of Human Vascular Smooth Muscle Cells”

Susu Zhao,¹ Zeqian Yu,² Yifen Zhang,¹ and Mei Lin ³

¹Department of Pathology, Affiliated Hospital of Nanjing University of Chinese Medicine, 210029 Nanjing, China

²Department of Hepatic-Biliary-Pancreatic Center, Zhongda Hospital, Southeast University, 210029 Nanjing, China

³Clinical Laboratory, Taizhou People's Hospital, Affiliated Hospital of Nanjing University of Chinese Medicine, 225300 Taizhou, China

Correspondence should be addressed to Mei Lin; l_mei@163.com

Received 14 February 2021; Accepted 14 February 2021; Published 31 July 2021

Copyright © 2021 Susu Zhao et al. This is an open access article distributed under the Creative Commons Attribution License, which permits unrestricted use, distribution, and reproduction in any medium, provided the original work is properly cited.

In the article titled “Effects of Arsenic Trioxide-Loaded PLGA Nanoparticles on Proliferation and Migration of Human Vascular Smooth Muscle Cells” [1], the author's identified errors in the legends of Figures 4 and 5, where “6 $\mu\text{mol/L}$ ” should be corrected to the 3 $\mu\text{mol/L}$ group as follows:

Figure 4: Results of Transwell cell migration assay. * $P < 0.05$, ** $P < 0.01$, and *** $P < 0.001$, compared with the control group; # $P < 0.05$ and ## $P < 0.01$, compared with the 1 $\mu\text{mol/L}$ group; & $P < 0.05$, compared with the 3 $\mu\text{mol/L}$ group.

Figure 5: Relative mRNA expression by RT-PCR. * $P < 0.05$, ** $P < 0.01$, and *** $P < 0.001$, compared with the control group; # $P < 0.05$ and ## $P < 0.01$, compared with the 1 $\mu\text{mol/L}$ group; & $P < 0.05$, compared with the 3 $\mu\text{mol/L}$ group.

The authors apologize for this error and confirm that it does not affect the conclusions of the article.

References

- [1] S. Zhao, Z. Yu, Y. Zhang, and M. Lin, “Effects of Arsenic Trioxide-Loaded PLGA Nanoparticles on Proliferation and Migration of Human Vascular Smooth Muscle Cells,” *Journal of Nanomaterials*, vol. 2021, Article ID 5575370, 8 pages, 2021.

Research Article

Effects of Arsenic Trioxide-Loaded PLGA Nanoparticles on Proliferation and Migration of Human Vascular Smooth Muscle Cells

Susu Zhao,¹ Zeqian Yu,² Yifen Zhang,¹ and Mei Lin ³

¹Department of Pathology, Affiliated Hospital of Nanjing University of Chinese Medicine, 210029 Nanjing, China

²Department of Hepatic-Biliary-Pancreatic Center, Zhongda Hospital, Southeast University, 210029 Nanjing, China

³Clinical Laboratory, Taizhou People's Hospital, Affiliated Hospital of Nanjing University of Chinese Medicine, 225300 Taizhou, China

Correspondence should be addressed to Mei Lin; l_mei@163.com

Received 14 February 2021; Revised 18 April 2021; Accepted 8 May 2021; Published 3 June 2021

Academic Editor: Luis Jesús Villarreal-Gómez

Copyright © 2021 Susu Zhao et al. This is an open access article distributed under the Creative Commons Attribution License, which permits unrestricted use, distribution, and reproduction in any medium, provided the original work is properly cited.

Background. To evaluate improvement of arsenic trioxide-loaded PLGA nanoparticles (As_2O_3 -PLGA-NPs) to Human Vascular Smooth Muscle Cells (HUVSMCs) *in vitro*. **Methods.** As_2O_3 -PLGA-NPs were synthesized and characterized by transmission electron microscopy (TEM), scanning electron microscope (SEM), and energy dispersive spectrometry (EDS), and the cumulative release rates of As_2O_3 -PLGA-NPs were measured *in vitro*; HUVSMCs were treated with As_2O_3 -PLGA-NPs *in vitro*. MTT assay and flow cytometry assay (FCM) were performed to examine the inhibitory effect of As_2O_3 -PLGA-NPs on HUVSMCs and compared with As_2O_3 solution at various concentrations. Optical microscope was used to observe the morphological change of HUVSMCs treated with As_2O_3 -PLGA-NPs. The expression of Bcl-2, Bax, and MMP-9 in HUVSMCs was detected by RT-PCR and Western blot (WB). **Results.** EDS confirmed that prepared nanoparticles contained elements of arsenic. The surface coating of the eluting stent of As_2O_3 -PLGA-NPs has the same characteristics with our self-prepared As_2O_3 -PLGA-NPs, and it also has a drug sustained-release character. Compared with the control group, cell proliferation and migration cell were significantly suppressed with concentration-dependent ($P < 0.05$, respectively). Meanwhile, in concentration-dependent, As_2O_3 -PLGA-NPs depressed mRNA and protein expression of Bcl-2 and MMP-9 and increased mRNA and protein expression of Bax. **Conclusion.** As_2O_3 -PLGA-NPs had an inhibitory effect on HUVSMCs' proliferation and migration, and it may work via regulating Bax, Bcl-2, and MMP-9 expression *in vitro*.

1. Introduction

Although percutaneous coronary intervention (PCI) plays an important role in the treatment of coronary artery disease, there is still a risk of stent restenosis [1]. Vascular smooth muscle cells (VSMCs) are a key part in intimal thickening of in-stent restenosis (ISR) [2, 3]. Arsenic compounds are natural substances that can effectively inhibit acute promyelocytic leukemia (APL) [4]. Related studies have shown that arsenic trioxide (As_2O_3) has a therapeutic effect on other types of malignant tumors [5–7]. As_2O_3 can effectively inhibit cell proliferation and has been widely used in clinical practice. The dosage forms of As_2O_3 were proposed [8, 9].

Drugs encapsulated in nanomaterials can effectively improve drug stability, release durability and biosafety, and reduce drug biodegradation. Polylactic-co-glycolic acid (PLGA) is a synthetic copolymer of poly (lactic acid) (PLA) and poly (glycolic acid) (PLGA). A large number of experimental studies have proved that PLGA is an important biomedical polymer material with good biodegradability and biocompatibility. It does not cause an obvious inflammatory reaction, immune reaction, and cytotoxic reaction [10]. PLGA has been approved by the US Food and Drug Administration (FDA) as a material for injection drugs, nanoparticles, implants, and other preparations and is widely used in the research of drug delivery system. Therefore, we choose PLGA

as the drug carrier. In this study, we prepared arsenic trioxide- (As_2O_3 -) loaded PLGA nanoparticles (As_2O_3 -PLGA-NPs), investigated their general properties and As_2O_3 bioactivity, and evaluated the effects of As_2O_3 -PLGA-NPs on proliferation and migration of Human Vascular Smooth Muscle Cells (HUVSMCs). To clarify the molecular mechanism of HUVSMCs apoptosis induced by trioxide-loaded PLGA nanoparticles, the expression of Bax, Bcl-2, and MMP-9 was examined.

2. Materials and Methods

2.1. Materials. As_2O_3 , DEPC, Triblue, HRP-labeled goat anti-mouse IgG secondary antibody, and 5-diphenyl-2H-tetrazoliumbromide (MTT) were supplied by Sigma Corporation (USA). HUVSMCs, bought from Sciencell Corporation (USA), were maintained in Smooth muscle cell medium (SMCM, also provided by Sciencell Corporation). AMV reverse transcriptase, DNTP, Oligo (dT) 18, Taq DNA polymerase, RNasin, RNase free DNase I, and 100bp DNA Molecular Weight Marker were purchased from Takara Biotechnology Corporation (Japan). GENMED-Bradford Protein Concentration Quantitative Kit was purchased from Pharmaceutical Technology Corporation (Shanghai, China). Relative antibody was supplied by ZSGB-BIO Engineering Corporation (Beijing, China).

2.2. Preparation of the As_2O_3 -PLGA-NPs and their Characteristics. Referencing our previous research, we prepared As_2O_3 -PLGA-NPs [11, 12]. After 10 μl suspension was aspirated, using transmission electron microscope (TEM), scanning electron microscopy (SEM), energy dispersive spectrometer (EDS), and computer color magic image analysis system to observe characteristics.

2.3. Determination of Drug Loading and Encapsulation Ratio of As_2O_3 . Appropriate amount of As_2O_3 -PLGA-NPs colloidal suspension was added at 4°C. After centrifugation at 15000 R/min for 30 min, the precipitate was washed three times with deionized water, and the supernatant was mixed. The precipitate was frozen in a vacuum to obtain the lyophilized powder, and then, a certain amount of deionized water was used to fix the volume. The amount of As_2O_3 in the precipitate (W1) and the amount of free As_2O_3 in the combined supernatant (W2) were determined by hydride generation atomic fluorescence spectrometry, and the amount of As_2O_3 in As_2O_3 - PLGA - NPs = W1, the total amount of As_2O_3 = W1 + W2. The drug loading and entrapment efficiency of the nanoparticles were calculated according to the following formula (W_{PLGA} was the amount of PLGA added):

$$\text{Drug loading}(\%) = W1/W_{\text{PLGA}} \times 100\%$$

$$\text{Encapsulation efficiency}(\%) = W1/(W1 + W2) \times 100\%$$

(1)

2.4. In Vitro Release Test. 5 mg of As_2O_3 -PLGA-NPs accurately weighed and dispersed in a final volume of 5 mL normal saline and, then, sealed in a pretreated dialysis bag. The bag was immersed in a conical bottle containing 30 mL saline

with constant rate stirring (50 r/min) at $37^\circ\text{C} \pm 1^\circ\text{C}$. The samples were taken at the same time point on the 1st, 2nd, 3rd, 4th, 5th, 6th, 7th, 8th, 9th, 10th, 11th, 12th, 13th, 14th, and 15th day, respectively. At the same time, the same amount of (1 mL) release medium was added to determine the content of As_2O_3 in the release solution, and the curve of time and cumulative release concentration was drawn.

2.5. Cell Culture. HUVSMCs were maintained in SMCM and cultured at 37°C in a 5% (v/v) CO_2 atmosphere. HUVSMCs in the logarithmic growth stage were taken in the experiment.

2.6. MTT Assay. HUVSMCs were seeded in a 96-well plate with 5,000 cells per well and, after 24 h incubation, were treated for 1-5 d by different methods as follows: (1) a negative control group (SMCM), (2) 1 $\mu\text{mol/L}$ As_2O_3 , (3) 1 $\mu\text{mol/L}$ As_2O_3 -PLGA-NPs, (4) 3 $\mu\text{mol/L}$ As_2O_3 , (5) 3 $\mu\text{mol/L}$ As_2O_3 -PLGA-NPs, (6) 6 $\mu\text{mol/L}$ As_2O_3 , and (7) 6 $\mu\text{mol/L}$ As_2O_3 -PLGA-NPs; then, 20 μl MTT (5 mg/mL) was added and continued to incubate for 4 h (37°C , 5% CO_2). Finally, 150 μl DMSO was added and shaking for 10 min. The absorbance was measured at 492 nm using a spectrophotometer. The following formula was used to calculate the cell viability percentage (VP) [13]:

$$\text{VP} = \text{OD of experimental group} / \text{OD of control group} \times 100\% \quad (2)$$

2.7. Flow Cytometry Assay. Cells were treated 24 h by four different groups as follows: (1) a negative control group (SMCM), (2) 1 $\mu\text{mol/L}$ As_2O_3 -PLGA-NPs, (3) 3 $\mu\text{mol/L}$ As_2O_3 -PLGA-NPs, and (4) 6 $\mu\text{mol/L}$ As_2O_3 -PLGA-NPs; after 24 h, cells were collected and washed in cold PBS (0.1 M, pH 7.2-7.4) three times, resuspended and fixed in 70% ethanol at 4°C for 10 min in the dark. According to the protocol of the kit for measuring cell apoptosis, the cell apoptosis rate of each group was detected by flow cytometry.

2.8. Inhibitory Effect of As_2O_3 -PLGA-NPs on HUVSMCs Migration Was Determined by Transwell Chamber Experiment. Logarithmic HUVSMCs were selected, and As_2O_3 -PLGA-NPs with different concentrations (excluding serum) were added to the experimental groups, to reach the final concentrations of 1 $\mu\text{mol/L}$, 3 $\mu\text{mol/L}$, and 6 $\mu\text{mol/L}$, adding culture medium to the blank control group. 200 μl cell suspension was inoculated on the Transwell insert (the pore size was 8 μm), and then, the upper chamber was put into the culture hole; the cells were cultured for 12 hours; the smooth muscle cells migrated to the subventricular surface of the filter membrane were photographed under a microscope and counted. The 5 cells under a high power field were taken from each sample.

2.9. Detection of Bcl-2, Bax, and MMP-9 Expressions by RT-qPCR. NP was added to HUVSMCs to reach the final administration concentrations of 3 $\mu\text{mol/L}$ and 6 $\mu\text{mol/L}$; SMCM was added to the control group. After 72 hours of culture, the total RNA was extracted by Trizol. The primer sequences of Bax, Bcl-2, and MMP-9 in RT-qPCR reaction and

TABLE 1: The relative sequence.

Gene name	F:(5'-3')	R:(5'-3')
Bcl-2	TGTGGCCTTCTTTGAGTTCG	TCACTTGTGGCTCAGATAGG 3
Bax	GCGTCCACCAAGAAGCTGAG	ACCACCCTGGTCTTGGATCC
MMP-9	GAGACCGGTGAGCTGGATAG	TACACGCGAGTGAAGGTGAG
GAPDH	AGCCTCAAGATCATCAGCAATG	TGTGGTCATGAGTCCTTCCACG

reference GAPDH gene were listed in Table 1, which was designed and synthesized by Sangon Biotech (Shanghai) Co., Ltd. The data detected and analyzed by IQ5TM Real-time PCR Detection System and expressed by $2^{-\Delta\Delta Ct}$.

2.10. Detection of Bcl-2, Bax, and MMP-9 Expressions by Western-Blot (WB). NP was added to HUVSMCs to reach the final administration concentrations of $3\ \mu\text{mol/L}$ and $6\ \mu\text{mol/L}$; SMCM was added to the control group. After 72 hours of culture, the HUVSMCs of each group were lysed and the total proteins of each group were extracted. The actual concentration of total protein extracted from each group was determined; total protein for each sample ($50\ \mu\text{g}$) was developed by 10% SDS-PAGE gel electrophoresis and Western blot, scanned by gel imaging system, and the images were saved and analyzed by Gel-pro32; the results were expressed by OD value.

2.11. Statistical Analysis. The data were shown as mean \pm SD, and the significance of difference with the control group was subject to the Poisson distribution and ANOVA variance analysis; $P < 0.05$ means the difference is statistically significant, and the statistical process was completed by statistical software SAS8.1 and SPSS17.0.

3. Results and Discussion

3.1. General Characteristics of NP. The prepared NP is a milky white colloid. There is no delamination deposition at 4°C for 12 h. NP has a slight delamination after 24 hours and can be suspended stably after ultrasonic processing for 1 min.

3.2. Electron Microscopic Observation. After ultrasonic dispersion, the prepared NP was observed by transmission electron microscope (Figure 1(a)) and scanning electron microscope (Figure 1(b)); it was nearly circular and had a certain electron density, showing dispersed spheres. The average particle size of NP prepared in this experiment is calculated to be $90 \pm 31\ \text{nm}$ by using the CMIAS98A image analysis system.

3.3. EDS Detection. Several visual fields under scanning electron microscope were selected, and the components of NP were analyzed by energy disperse spectroscopy (Figure 1(c)); it can be seen that it contains components of As, C, and O; the weight percentage content (wt%) of As was 3.25% and the atomic percentage content (At%) was 0.72%. Therefore, it can be confirmed that NP has been successfully prepared.

3.4. Dynamic Determination Results of As_2O_3 Release from PLGA NPs. The in vitro dynamic release of NP was investigated with saline as medium; the cumulative release rate of the drug reached 72.37% on the 4th day and 96.82% on the 15th day and gradually entered the platform stage (Figure 2).

3.5. MTT Results. The growth rates of As_2O_3 and NP (NP) with different concentrations on HUVSMCs were listed in Table 2. It was found in the experiment that both As_2O_3 and NP could inhibit the growth of HUVSMCs and produce certain cytotoxicity and showed an obvious time and concentration-dependent relationship ($P < 0.05$). MTT results showed that after $6\ \mu\text{M}$ NP treatment for 3 days, it had an inhibitory effect on the proliferation of HUVSMCs, while its toxicity was the least. The relative data was shown in Table 2.

3.6. Flow Cytometer Detection Results. The detection results of flow cytometer showed apoptosis rate of NP intervention group significantly increased ($P < 0.05$), and the apoptosis rate increased gradually with the increase of drug concentration. The data was shown in Figure 3.

3.7. Results of Transwell Cell Migration Assay. The results of Transwell showed a number of invasive cells in NP intervention group decreased significantly ($P < 0.05$, Figure 4), and NP inhibited migration of HUVSMCs in a concentration dependent manner.

3.8. Detection of Related mRNA Expression by RT-qPCR. Compared with the control group, Bcl-2 and MMP-9 genes in NP intervention group decreased significantly, while Bax gene significantly increased ($P < 0.05$, Figure 5), showing a significant concentration-effect relationship.

3.9. Detection of Related Protein Expression by WB. Compared with the control group, Bcl-2 and MMP-9 proteins in NP intervention group decreased significantly, while Bax protein significantly increased ($P < 0.05$, Figure 6), showing a significant concentration-effect relationship.

3.10. Discussion. In this experiment, referencing our previous research, emulsification evaporation technique was used to prepare NP, in which emulsion solvent was prepared by mechanical stirring or phacoemulsification of the two immiscible phases. The internal phase solvent was removed by evaporation, and the spherical material was precipitated and solidified into microspheres. The internal disperse phase solvent must have certain solubility and volatility in the external continuous phase. Under slow stirring condition, the internal disperse phase solvent diffuses to the external

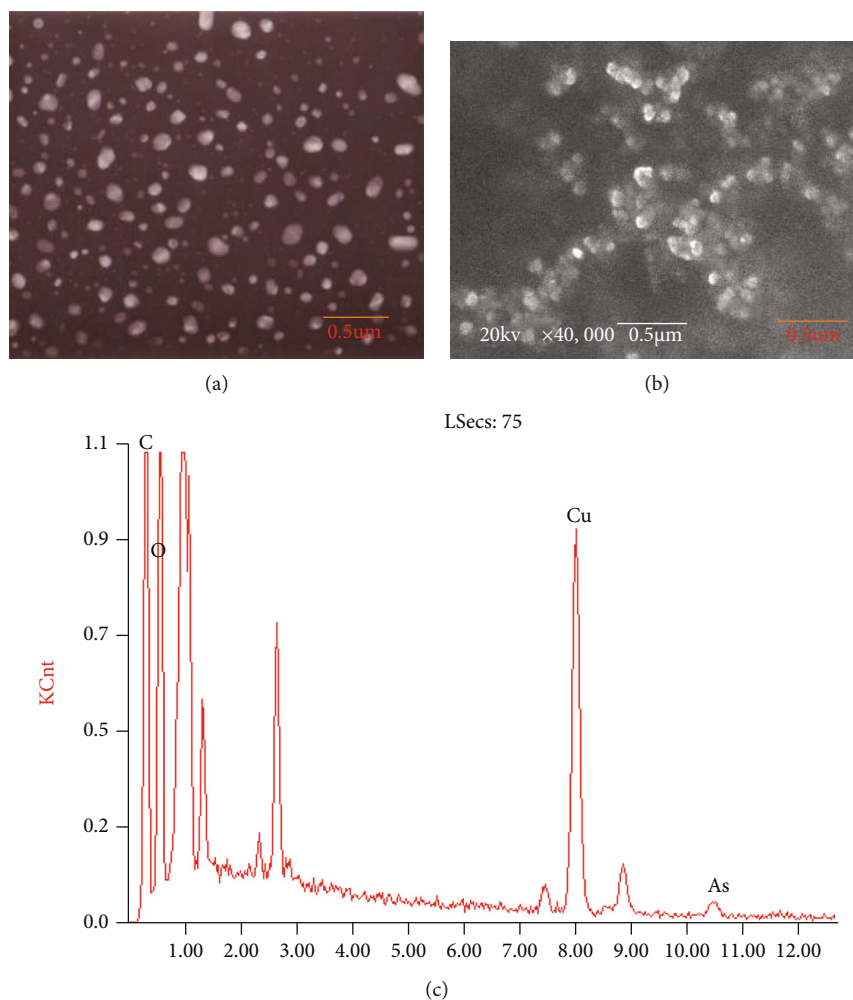


FIGURE 1: (a) TEM photos. (b) SEM photos. (c) Detection results of nano- $\text{As}_2\text{O}_3/\text{PLGA}$ by EDS.

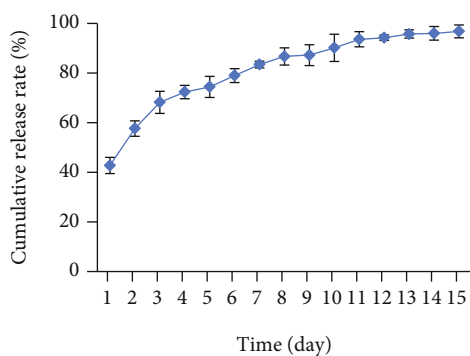


FIGURE 2: Cumulative release rate of As_2O_3 from nano- $\text{As}_2\text{O}_3/\text{PLGA}$.

phase, transports to the liquid level, and volatilizes into the air. The extraction-volatilization-extraction process was repeated, so that the carrier material in the internal dispersion phase precipitated to form a capsule, and the drug was wrapped therein until the microspheres were completely cured. In this experiment, the organic phase was PLGA/dichloromethane solution with As_2O_3 , and the aqueous phase was a PVA aqueous solution of a certain concentration; after the two phases were mixed, the emulsion was prepared by

magnetic stirring; with the gradual removal of dichloromethane by evaporation, the spherical nanomaterials were precipitated and freeze-dried to form nanomicrospheres.

At present, it is recognized that the mechanism of ISR formation is a key part in excessive proliferation induced by injury and migration of VSMCs to inner membrane in addition to elastic retraction and thrombosis of vascular wall after vasodilation. Therefore, the search for drugs that inhibit the proliferation and migration of VSMC has become a hot topic in the study of ISR [14]. In this experiment, the effects of NP and As_2O_3 of different concentrations on HUVMSCs were studied. Under inverted microscope, after HUVMSCs was treated with $3 \mu\text{mol/L}$ As_2O_3 for 24 h, the cells began to round and wrinkle, and cell number decreased significantly. MTT assay results of NP and As_2O_3 of different concentrations for the HUVMSCs showed that NP was a sustained release system with good biocompatibility and also had an antiproliferation potential. As_2O_3 and NP had inhibitory effect on growth of HUVMSCs in a time- and concentration-dependent manner. MTT assay results showed effect of As_2O_3 on HUVMSCs entered the platform stage on the 3rd day, but the inhibitory effect of the As_2O_3 of same concentration on the cells before entering the platform stage was almost

TABLE 2: The cell viability percentage of difference groups (%) (mean ± s).

Group	1d	2d	3d	4d	5d
Control	100	100	100	100	100
1 μM As ₂ O ₃	97.13 ± 0.64*	92.56 ± 0.81*	88.76 ± 2.07*	85.76 ± 0.93*	82.58 ± 5.34*
1 μM NP	99.42 ± 0.58*	96.24 ± 1.39*	90.32 ± 3.24*	84.23 ± 3.27*	79.36 ± 7.23*
3 μM As ₂ O ₃	63.27 ± 3.26*	56.73 ± 1.59*	39.78 ± 1.69*	36.92 ± 0.85*	26.64 ± 2.87*
3 μM NP	70.51 ± 1.74*	62.04 ± 0.78*	45.27 ± 0.81*#	37.84 ± 1.22*	21.39 ± 1.57*
6 μM As ₂ O ₃	46.38 ± 2.39*	30.28 ± 4.25*	12.58 ± 1.31*	7.23 ± 1.56*	6.24 ± 0.99*
6 μM NP	50.23 ± 6.81*	37.51 ± 2.23*	22.69 ± 2.43*#	6.42 ± 0.39*	5.13 ± 0.48*

*P < 0.05, compared with Control; #P < 0.05, compared with As₂O₃ group.

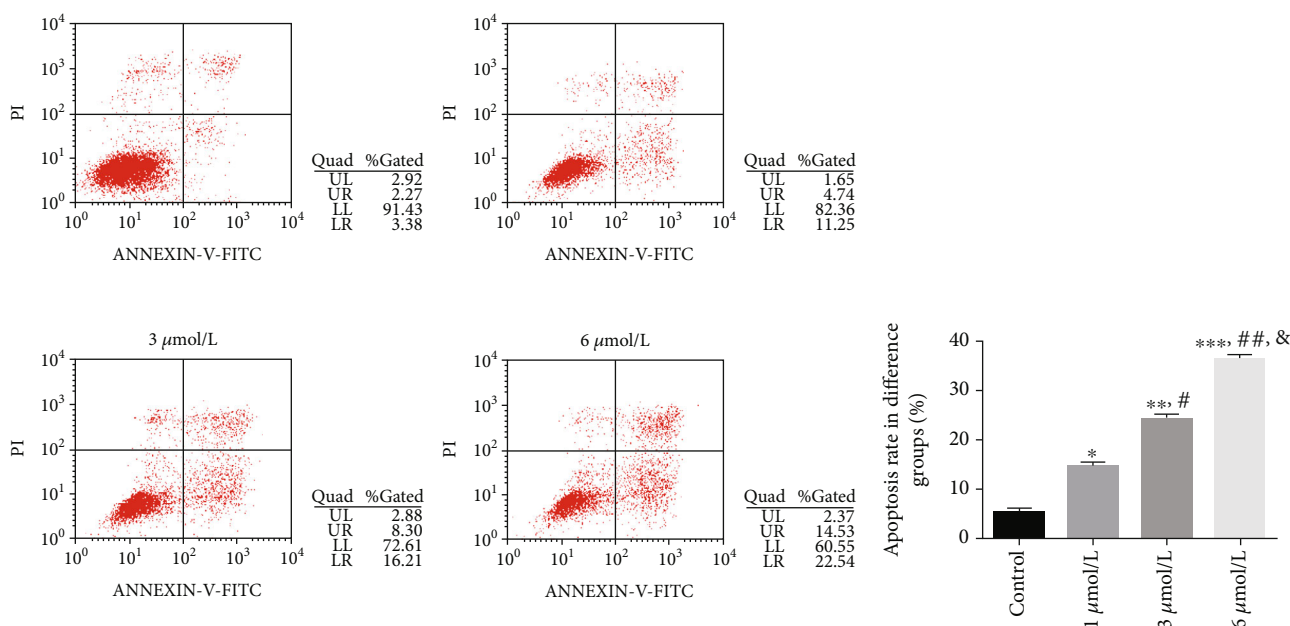


FIGURE 3: Flow cytometer detection results. *P < 0.05, **P < 0.01, ***P < 0.001, compared with the control group; #P < 0.05, ##P < 0.01, compared with 1 μmol/L group; &P < 0.05, compared with 3 μmol/L group.

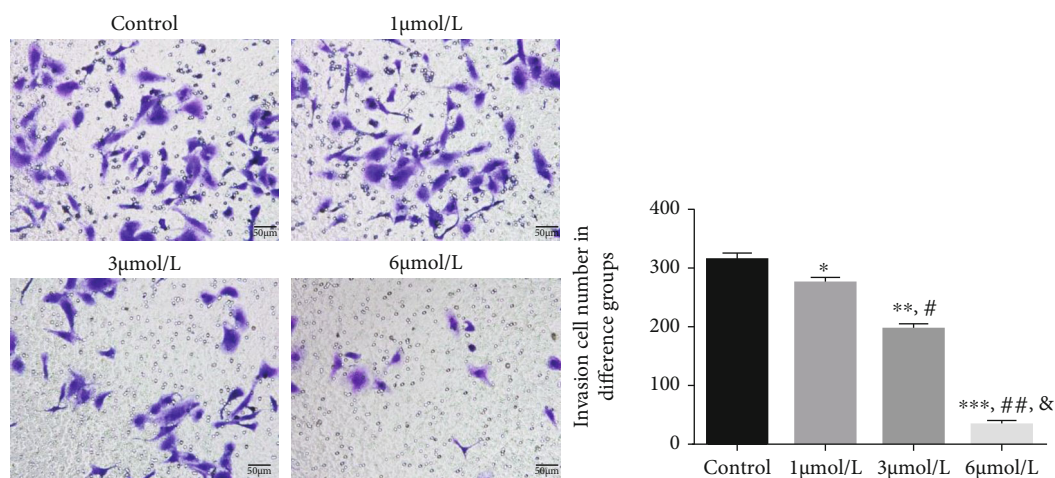


FIGURE 4: Results of Transwell cell migration assay. *P < 0.05, **P < 0.01, ***P < 0.001, compared with the control group; #P < 0.05, ##P < 0.01, compared with 1 μmol/L group; &P < 0.05, compared with 6 μmol/L group.

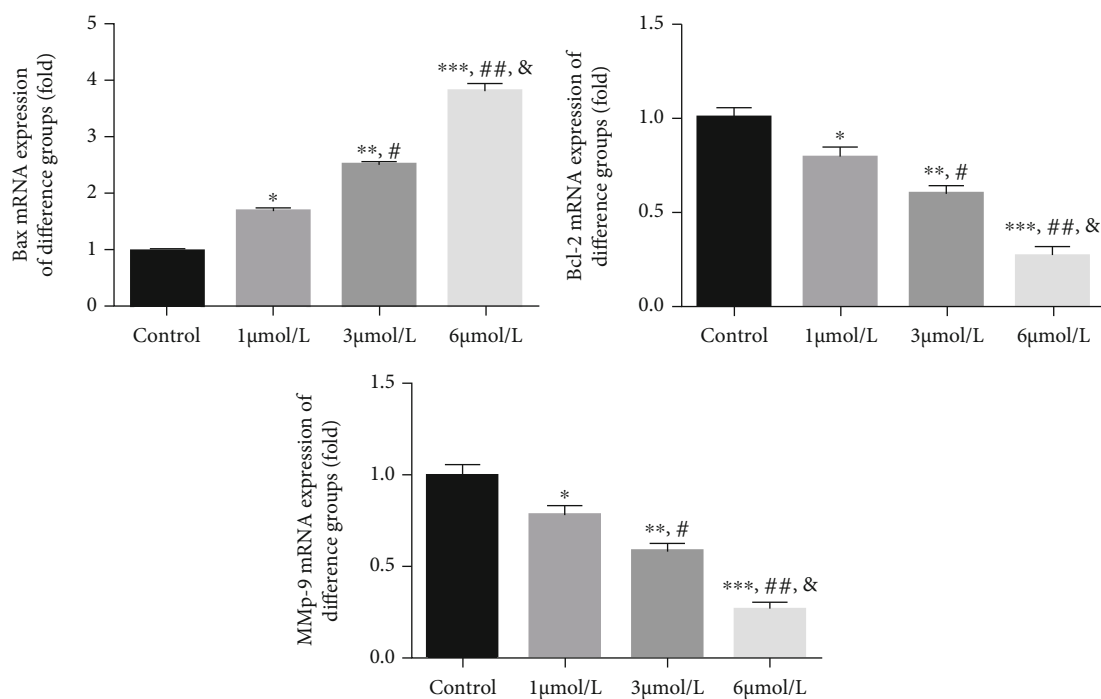


FIGURE 5: Relative mRNA expression by RT-PCR. * $P < 0.05$, ** $P < 0.01$, *** $P < 0.001$, compared with the control group; # $P < 0.05$, ## $P < 0.01$, compared with 1 $\mu\text{mol/L}$ group; & $P < 0.05$, compared with 6 $\mu\text{mol/L}$ group.

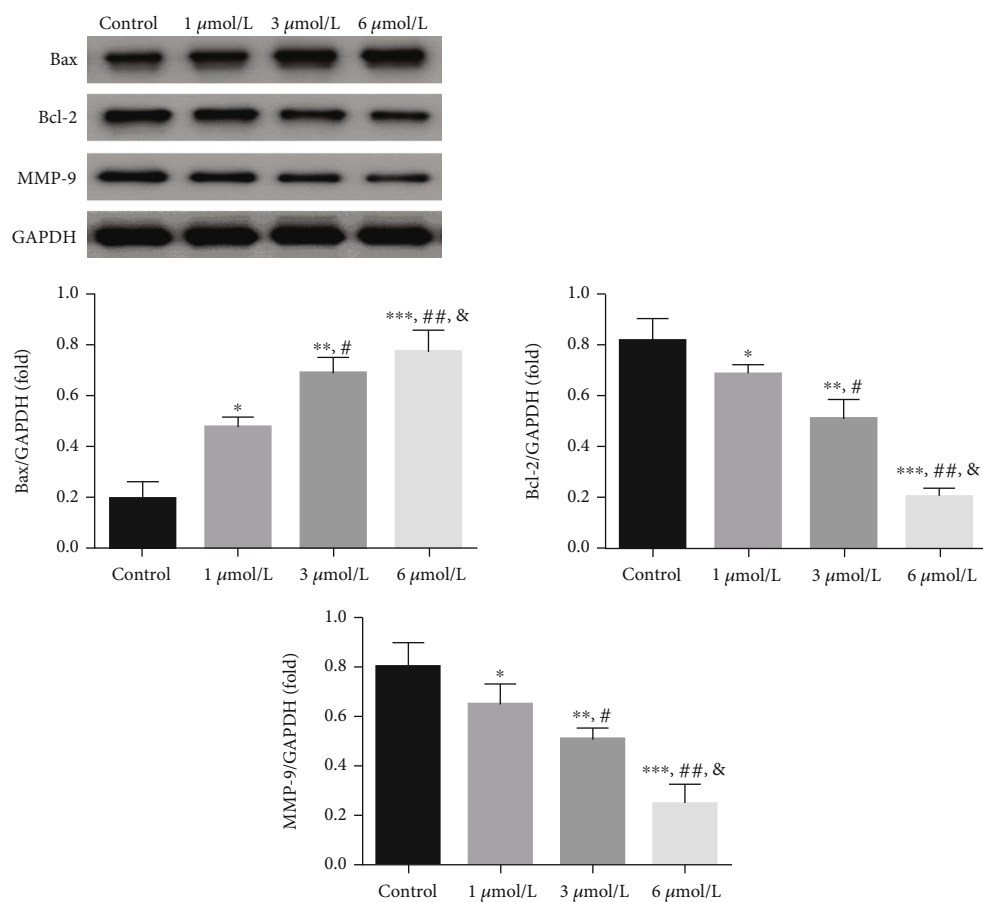


FIGURE 6: Relative protein expression by WB assay. * $P < 0.05$, ** $P < 0.01$, *** $P < 0.001$, compared with the control group; # $P < 0.05$, ## $P < 0.01$, compared with 1 $\mu\text{mol/L}$ group; & $P < 0.05$, compared with 3 $\mu\text{mol/L}$ group.

the same as that of NP on the 4th day with the cumulative drug release rate of 72.37%. This may be related to the physical and chemical properties of nanoparticles. When the material is processed to the nanoscale, due to the quantum size effect, the little size effect, and the surface effect, the nanoparticles will show the peculiar physical, chemical, and biological properties, which make the nanoparticles have some new characteristics and functions [15, 16]. To further investigate the mechanism of NP for inhibiting the proliferation and migration of HUVSMCs, the related proteins were detected.

Bcl-2 gene family is the most important related gene. Bcl-2 gene can resist apoptosis induced by chemotherapeutic drugs. Bax is a homologous protein of Bcl-2, and it can not only produce homopolymer but also produce heterodimer with Bcl-2, thus eliminating the antiapoptosis effect of Bcl-2 gene; in this respect, it can promote apoptosis; on the other hand, it may also weaken the upregulation of telomerase activity by Bcl-2 [17–19]. In this study, the results showed Bcl-2 and Bax expressions in HUVSMCs changed significantly after NP intervention, showing a significant concentration-effect relationship. It is inferred that the apoptosis induced by NP may be closely related to Bcl-2 and Bax.

Matrix metalloprotease (MMPs) mediates basement membrane and extracellular matrix degradation and cell migration [20, 21]. Moreover, MMP-9 is an important member of MMPs and is a key part in the degradation of collagen VI and other matrix proteins in basement membrane [22]. The results in this study showed MMP-9 gene and protein were significantly inhibited after NP intervention, which might be related to the inhibition effect of NP on HUSAMCs migration.

4. Conclusions

In conclusion, NP is an ideal slow release preparation, which can prolong the effective acting time of As_2O_3 on vascular smooth muscle cells and inhibit cell growth and induce apoptosis *in vitro*. It is also discussed that the molecular mechanism of NP inhibiting the proliferation and migration of HUVSMCs may be realized by regulating the expressions of Bcl-2, Bax, and MMP-9. This new dosage form is expected to become a drug coating on the surface of drug eluting stents in the future, which provides new idea and method for clinical prevention and treatment of restenosis in stents.

Data Availability

The figure and table data used to support the findings of this study are included within the article.

Conflicts of Interest

The authors declare no conflict of interest.

Acknowledgments

This research has been supported by the General medical research project of Jiangsu Health Commission (M2020062) and Hospital-level project of Jiangsu Province Hospital of Chinese Medicine (Y17010).

References

- [1] R. Hoffmann and G. S. Mintz, “Coronary in-stent restenosis—predictors, treatment and prevention,” *European Heart Journal*, vol. 21, no. 21, pp. 1739–1749, 2000.
- [2] M. S. Lee and G. Banka, “In-stent Restenosis,” *Interventional Cardiology Clinic*, vol. 5, no. 2, pp. 211–220, 2016.
- [3] D. G. Kokkinidis, S. W. Waldo, and E. J. Armstrong, “Treatment of coronary artery in-stent restenosis,” *Expert Review of Cardiovascular Therapy*, vol. 15, no. 3, pp. 191–202, 2017.
- [4] J. Ni, G. Chen, Z. Shen et al., “Pharmacokinetics of intravenous arsenic trioxide in the treatment of acute promyelocytic leukemia,” *Chinese Medical Journal*, vol. 111, no. 12, pp. 1107–1110, 1998.
- [5] Y.-H. Kang, M.-J. Yi, M.-J. Kim et al., “Caspase-Independent cell death by arsenic trioxide in human cervical cancer Cells,” *Cancer research*, vol. 64, no. 24, pp. 8960–8967, 2004.
- [6] M. Hoonjan, V. Jadhav, and P. Bhatt, “Arsenic trioxide: insights into its evolution to an anticancer agent,” *Journal of Biological Inorganic Chemistry*, vol. 23, no. 3, pp. 313–329, 2018.
- [7] Z. Diaz, M. Colombo, K. K. Mann et al., “Trolox selectively enhances arsenic-mediated oxidative stress and apoptosis in APL and other malignant cell lines,” *Blood*, vol. 105, no. 3, pp. 1237–1245, 2005.
- [8] Z. Yang, M. Yang, and J. Peng, “Evaluation of arsenic trioxide-loaded albumin nanoparticles as carriers: preparation and antitumor efficacy,” *Drug development and industrial pharmacy*, vol. 34, no. 8, pp. 834–839, 2008.
- [9] K. Ward, J. G. C. Cortés, and D. Stuckey, “Alginate as a support ligand for enhanced colloidal liquid apherin immobilization of proteins and drug delivery,” *Biotechnology and Bioengineering*, vol. 116, no. 12, pp. 3168–3178, 2019.
- [10] D. N. Kapoor, A. Bhatia, R. Kaur, R. Sharma, G. Kaur, and S. Dhawan, “PLGA: a unique polymer for drug delivery,” *Therapeutic delivery*, vol. 6, no. 1, pp. 41–58, 2015.
- [11] G. Amasya, U. Badilli, B. Aksu, and N. Tarimci, “Quality by design case study 1: design of 5-fluorouracil loaded lipid nanoparticles by the W/O/W double emulsion solvent evaporation method,” *European Journal of Pharmaceutical Sciences*, vol. 10, pp. 92–102, 2016.
- [12] T. K. Giri, C. Choudhary, A. Alexander, H. Badwaik, and D. K. Tripathi, “Prospects of pharmaceuticals and biopharmaceuticals loaded microparticles prepared by double emulsion technique for controlled delivery,” *Saudi Pharmaceutical Journal*, vol. 21, no. 2, pp. 125–141, 2013.
- [13] T. Mosmann, “Rapid colorimetric assay for cellular growth and survival: application to proliferation and cytotoxicity assays,” *Journal of Immunological Methods*, vol. 65, no. 1–2, pp. 55–63, 1983.
- [14] M. F. Brancati, F. Burzotta, C. Trani, O. Leonzi, C. Cuccia, and F. Crea, “Coronary stents and vascular response to implantation: literature review,” *Pragmatic and observational research*, vol. 13, no. 8, pp. 137–148, 2017.
- [15] H. Chen, X. Zheng, Y. Chen, M. Li, K. Liu, and X. Li, “Influence of copper nanoparticles on the physical-chemical properties of activated sludge,” *PLoS One*, vol. 9, no. 3, 2014.
- [16] J. Zhang, H. Tang, Z. Liu, and B. Chen, “Effects of major parameters of nanoparticles on their physical and chemical properties and recent application of nanodrug delivery system in targeted chemotherapy,” *International Journal of Nanomedicine*, vol. Volume 12, pp. 8483–8493, 2017.

- [17] C. J. Larsen, "The BCL2 gene, prototype of a gene family that controls programmed cell death (apoptosis)," *Annals Genetic*, vol. 37, no. 3, pp. 121–134, 1994.
- [18] Y. Zhang, X. Yang, X. Ge, and F. Zhang, "Puerarin attenuates neurological deficits via Bcl-2/Bax/cleaved caspase-3 and Sirt3/SOD2 apoptotic pathways in subarachnoid hemorrhage mice," *Biomed Pharmacother*, vol. 109, pp. 726–733, 2019.
- [19] C. Yao, X. Cao, Z. Fu et al., "Boschniakia rossica polysaccharide triggers laryngeal carcinoma cell apoptosis by regulating expression of Bcl-2, Caspase-3, and P53," *Medical science monitor*, vol. 29, no. 23, pp. 2059–2064, 2017.
- [20] H. Huang, "Matrix metalloproteinase-9 (MMP-9) as a cancer biomarker and MMP-9 biosensors: recent advances," *Sensors*, vol. 18, no. 10, p. 3249, 2018.
- [21] A. Hrabia, D. Wolak, and M. Kwaśniewska, "Expression of gelatinases (MMP-2 and MMP-9) and tissue inhibitors of metalloproteinases (TIMP-2 and TIMP-3) in the chicken ovary in relation to follicle development and atresia," *Theriogenology*, vol. 125, pp. 268–276, 2019.
- [22] P. Wang, L. D. Zhang, M. C. Sun, W. D. Gu, and H. Z. Geng, "Over-expression of mir-124 inhibits MMP-9 expression and decreases invasion of renal cell carcinoma cells," *European review for medical and pharmacological sciences*, vol. 22, no. 19, pp. 6308–6314, 2018.

Review Article

The Magnetic Nanomaterial Biofunctions in Cancer Diagnosis and Therapy

Xuefeng Bian,¹ Ting Guo ,² Ji Zhang,¹ Jianguo Xia,¹ Xiaoqian Feng,² Fujin Wang,² Mei Lin ,³ and Weizhong Tian ¹

¹Imaging Department, Taizhou People's Hospital Affiliated to Nantong University, Taizhou 225300, China

²Institute of Clinical Medicine, Taizhou People's Hospital Affiliated to Nantong University, Taizhou 225300, China

³Clinical Medical Laboratory, Taizhou People's Hospital Affiliated to Nantong University, Taizhou 225300, China

Correspondence should be addressed to Mei Lin; l_mei@163.com and Weizhong Tian; jstztwz@163.com

Xuefeng Bian and Ting Guo contributed equally to this work.

Received 9 March 2021; Accepted 5 May 2021; Published 2 June 2021

Academic Editor: Luis Jesús Villarreal-Gómez

Copyright © 2021 Xuefeng Bian et al. This is an open access article distributed under the Creative Commons Attribution License, which permits unrestricted use, distribution, and reproduction in any medium, provided the original work is properly cited.

Magnetic nanomaterials have recently emerged, playing an increasingly essential role in life science and biomedicine fields, and they exhibited promising potentials in cancer diagnosis and therapy. Also, their use as contrast agents improved various cancer diagnostic imaging sensitivities and accuracy. Magnetic nanomaterials are also exploited as targeted drug carriers to increase the sensitivity and reduce the side effects of chemotherapeutic drugs. Herein, we reviewed the preparation, characterization, and surface modification of various magnetic nanomaterials and their cancer diagnosis and therapy applications.

1. Introduction

Cancer remains the second most common cause of death, and its morbidity and mortality are increasing in China; this is mainly because most tumor onset is subtle and challenging to be detected in the early stage [1]. Most diagnosed cancer patients are already in advanced and late stages; this hinders requisite curative effect. Besides, the primary cancer treatment includes surgery, chemotherapy, and radiotherapy [2]. However, the complete removal of the tumor tissue through surgical treatment is intractable. Various side effects and adverse reactions often accompany radiotherapy and chemotherapy. Moreover, tumors could evolve metastasis and drug resistance during progression or recurrence, which dramatically reduces the subsequent treatment effect [3]. Therefore, it is pivotal to identify new cancer treatments and prognostic methods.

The magnetic nanomaterial has newly emerged; they are characterized by small particle size, superparamagnetism,

and surface modification ease [4]. Magnetic nanoparticles can be employed in different aspects, combined with biomolecules, fluorescent probes, and antitumor drugs; currently, they are used as magnetic resonance contrast agents, targeted drug delivery, and in magnetic fluid hyperthermia [5]. The Fe₃O₄ core/shell/crown functional magnetic nanomaterials have achieved good therapeutic results in bladder cancer in vitro [6]. The gadolinium-doped iron oxide nanoparticles (GdIO NPs) showed good potential in magnetic resonance imaging and achieved promising results in breast cancer treatment in vitro [7]. The superparamagnetic PEG-modified La_{1-x}Sr_xMnO₃ (LSMO) magnetic nanoparticles exhibited favorable potency in magnetic resonance imaging and tumor magnetic fluid hyperthermia [8].

Herein, concerning the recent research on magnetic nanomaterials in tumor therapy, the preparation, surface modification, characterization analysis of magnetic nanomaterials, and their applications in tumor-targeted therapy and diagnosis are briefly reviewed.

2. Preparation and Characterization of Magnetic Nanomaterials

2.1. Preparation of Magnetic Nanomaterials. Fe₃O₄ and γ -Fe₂O₃-based nanoparticles are currently applicable in living organisms; this nanoparticle composition is beneficial as the iron-containing cells can maintain the intracellular environment's stability by absorbing, storing, and excreting iron atoms [9]. Also, iron can be easily removed from the body, allowing a comparatively large iron dose since the oxidative stress reaction is absent. Iron oxide nanoparticles are high safe [10]. Preparing magnetic nanomaterials are divided into physical and chemical approaches; this includes grinding, ultrasonic, and plasma methods. Currently, the preparation methodology includes hydrothermal synthesis, sol-gel, and forced hydrolysis and thermal decomposition [11].

2.1.1. The Coprecipitation Method. The coprecipitation is a convenient and straightforward method to obtain iron oxide particles; this is achieved by adding an alkaline solution to a salt solution of iron (Fe²⁺/Fe³⁺) in an inert gas atmosphere at room temperature. Its preponderance is that large amounts of iron oxide nanoparticles can be synthesized one time. However, the size of the magnetic nanomaterials obtained by the coprecipitation method is challenging to control, where the particle diameter distribution is relatively dispersed and tricky to be consolidated [12].

2.1.2. Sol-Gel and Forced Hydrolysis Techniques. In the sol-gel approach, molecular precursors in the solution are hydroxylated and condensed to obtain the initial nanoparticle solution. The initial solution is further condensed and set to be polymerized to obtain a three-dimensional wet gel of the metal oxide network. The wet gel characteristics are highly dependent on the structural treatment of the sol preparation. The method has advantages: materials can be customized, the size of particles is homogenous, and the reaction temperature is relatively low [13]. The γ -Fe₂O₃ nanoparticles obtained by the sol-gel method can be embedded in an inert, inorganic, and transparent silica matrix with high-temperature resistance. Sugimoto et al. reported that nanostructured oxides with various structures and compositions could be obtained following different preparation conditions, precursor properties, ion source, and pH [14].

2.1.3. Thermal Decomposition Method. Thermal decomposition is a commonly used approach in the biomedical field to prepare precise nanoparticles. This method helps control the nanoparticles' size and morphology and control the yield [15]. Recently, there are two main types of thermal decomposition: first, oxidizing the metal carbonyl precursor in the air after or during thermal decomposition [16]. The second is precursor decomposition with a cationic metal without a reducing agent [17]. Many small-sized monodisperse nanomagnetic crystals can be synthesized by dissolving metal-organic compounds in a high-boiling organic solvent with stable surfactant and thermal decomposition. Sun et al. discovered the broad applications of the organometallic precursors of acetyl-acetone; these precursors included iron, manganese, and nickel acetylacetonate [18]. The surfactants

used in this approach are usually fatty acids, oleic acid, and hexadecyl-amine [19]. Hyeno et al. have experimentally demonstrated that decomposing organometallic compound precursors by thermal decomposition with surfactant can achieve small and even nanoparticles with good crystallinity and dispersibility. The ratio of organometallic compound precursors, solvents, surfactants, temperature, time, and oxidation are all keys to control the nanoparticles diameter and morphology accurately [20]. This approach has a significant drawback as the final product is organic soluble nanoparticles, limiting its application in the biological field. Moreover, the produced nanoparticles by thermal decomposition often require further surface treatment, and the reaction process is intricate and requires high temperature [21].

2.1.4. Hydrothermal Synthesis Method. In this method, the reaction needs to be done in a reactor or autoclave under high pressure and temperature, 2000 psi, 200°C., respectively. Laurent used the hydrothermal approach in the preparation of Fe₃O₄ nanoparticles [22]. Different nanoparticles have been prepared by hydrothermal synthesis as it has better crystallinity over other techniques. However, different hydrothermal synthesis conditions may cause different particle crystallinities and affect their magnetism. The well-crystallized particles are thinner, have a narrower surface layer and cation distribution space, and their superparamagnetic relaxation is low.

2.1.5. Microemulsion. The water molecules have a spherical shape in the water-in-oil microemulsion and are surrounded by the surfactant molecules. The microemulsions can function as cages to produce nanoparticles, reducing the average particle size during collision and aggregation [23]. Thus, the nanoparticles' size can be controlled and adjusted by changing the size of water droplets, determined by the molar ratio of water to surfactant. This method can be used to control the size of the synthesized nanomaterial within a specific range. However, since the nanoparticles' size and shape generally vary within a relatively large range, the produced nanoparticles may be spherical, rectangular, or tubular [24]. Besides, compared with other methods, such as thermal decomposition and coprecipitation, the nanoparticles prepared by the microemulsion technique are less efficient, and the synthesis process is too complicated. Therefore, the microemulsion approach is mainly used in the laboratory.

2.2. Characterization and Detection of Magnetic Nanomaterials. The nanomaterials are initially characterized by their size and shape; these are crucial indicators to validate their production process. The transmission electron microscopy and high-resolution transmission electron microscopy are used to determine the nanomaterials' size and shape, and they require an ultrathin specimen. Their output data comprises grouped diffracted beams called a phase-contrast image (Figure 1) [25].

The crystal characteristics of the magnetic nanomaterial can also be detected by 40Kv, 30 mA-Cu K α X-ray. The unique iron peak in the diffraction pattern demonstrates the irons as magnetic nanomaterials [26]. Ge and S used X-

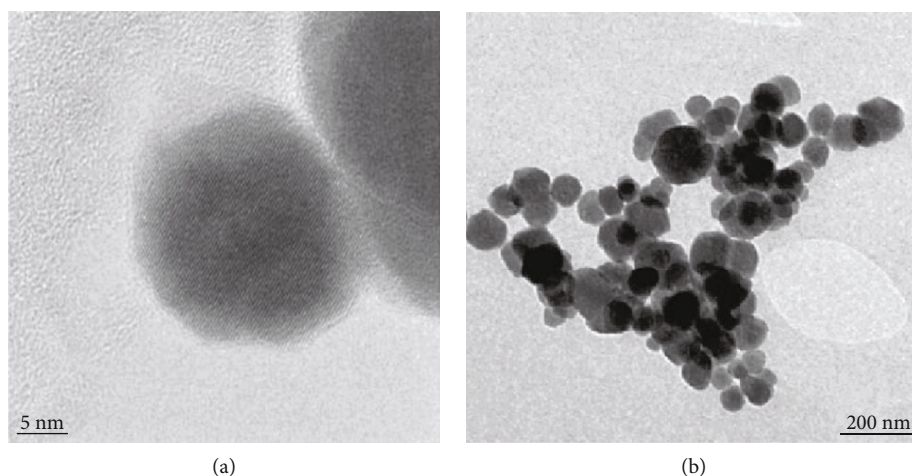


FIGURE 1: Nanomaterial's TEM image (a) and high-resolution TEM image (b).

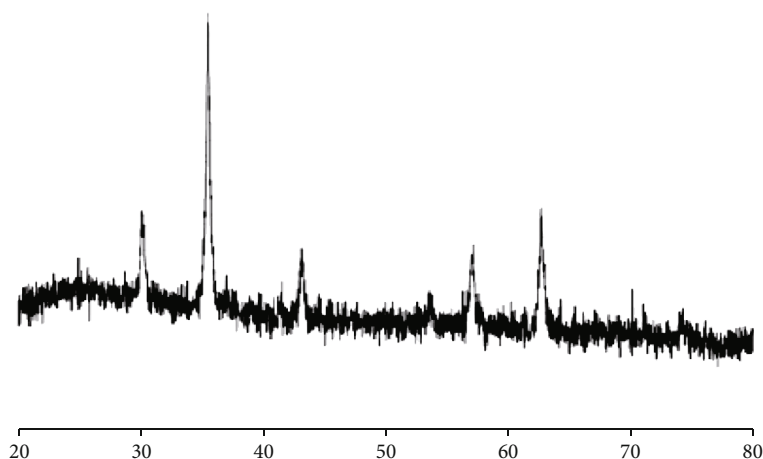


FIGURE 2: Typical map of iron oxide nanoparticles after analysis by X-ray diffraction.

ray diffraction to analyze the crystallization of magnetic nanoparticles in a powder state; they demonstrated that the magnetic nanoparticles without copolymer have six diffraction peaks at 2θ , 30.1, 35.4, 42.9, 52.7, 57.5, and 62.7 (Figure 2), indicating the presence of iron oxide at the corresponding peak [27].

The nanomaterial's magnetism is another critical characteristic. It is typically measured by a vibrating sample magnetometer, which can detect their magnetization changes with different field intensities. The nanomaterial's magnetism turns from the high baseline value to zero upon decreasing the applied field intensity. In that case, the iron oxide magnetic nanoparticles can be detected as a single crystal from the altered magnetic direction.

The chemical composition of the magnetic nanomaterials' functional ligands and polymers is determined using Fourier transform infrared spectroscopy. Bhattarai et al. detected a strong light emission from iron oxide nanoparticles in the low-frequency region (below 800 cm^{-1}) by Fourier transform infrared spectroscopy. Stabilizing the magnetic nanoparticles using cystic chitosan exhibited an alteration in the modified chitosan's infrared spectrum

due to the interaction with iron oxide nanoparticles [28]. This amide change of the light corresponding band spectrum from high energy to low energy indicates the nitrogen linkage of iron oxide nanoparticles to the modified chitosan.

3. Surface Modification of Magnetic Nanomaterials

The magnetic nanomaterial surface modification alleviates its cytotoxicity and improves their biocompatibility and binding capability to active molecules or compounds. Therefore, magnetic nanomaterial surface modification promotes it as a powerful tool in the biomedical field [29]. The main purpose of surface modification includes improving the stability of magnetic nanomaterials in vitro and in vivo and also minimizing residual magnetism. During the nanomaterial surface modification, the provided functional group on the surface enables further derivatization and enhances the solubility in various solvents, thereby broaden their applications [30]. Different nanomaterial surface modifications determine their antifouling property and hydrodynamic size; they also

TABLE 1: Commonly used surface modification materials for magnetic nanoparticles.

	Material	Properties	Application
High molecular polymer	Dextran [70]	Good biocompatibility and biodegradability	Stabilize the colloidal solution and increase the time of nanomaterial circulation in the blood
	Polyethylene glycol (PEG) [71]	With good hydrophilicity, it does not cause an immune response and antigen-antibody reaction	Reduce the phagocytosis time of nanomaterials by macrophages and increase the circulation time of nanomaterials in the blood
	Polyvinyl alcohol (PVA) [72]	Good hydrophilicity, biocompatibility, superior film, and gel-forming ability	Improve the stability of the colloidal solution
	Polyacrylic acid [73]	Good water solubility	Improve the biocompatibility of nanomaterials and help nanomaterials adhering
Surfactant [74]	Oleic acid, lauric acid, Dodecylphosphoric acid, cetylphosphonic acid, hexadecylphosphonic acid, alkanesulfonic acid, various phosphates, etc.	With good biocompatibility, it is safe and nontoxic. Although soluble in water, it can be soluble in various organic solvents.	Improve the stability and biocompatibility of nanomaterials
Inorganic coating	Silica [75]	Good biocompatibility, safe and nontoxic, chemically stable	The nanomaterials are prevented from degrading and coagulating in the organism, making it easier to connect functional groups
	Gold [76]	Biocompatibility, optical, and magnetic properties for biological applications	Improve the stability of magnetic nanoparticles and maintain the magnetic moment of magnetic nanomaterials
	Carbon [77]	Stable chemical properties, good thermal stability, and good biocompatibility	Improve the stability of magnetic nanomaterials, improve the oxidation resistance and acid resistance of magnetic nanoparticles

play an important role in their biokinetics and biodistribution in vivo [31]. For instance, the nanomaterial's overall particle size must be significantly small to avoid being engulfed by the reticuloendothelial system (RES), a vital nonspecific immune system formed by macrophages residing in tissues and relatively large to avoid kidney clearance. Besides, proper surface modification can reduce the magnetic nanomaterials' surface toxicity and enable them to be enriched in specific regions, a prerequisite in tumor diagnosis and targeted therapy [32]. Furthermore, the appropriate nanomaterials' surface modification exhibits precision characteristics when coated with targeting ligands such as proteins, peptides, antibodies, or other small molecules. This unique conjugation of the magnetic nanomaterial to specific ligands promotes identifying certain molecular markers on the surface of malignant cells, allowing the magnetic nanomaterials to be specifically enriched in the tumors, providing a strong basis for their use in tumor diagnosis and treatment [33]. Moreover, magnetic nanomaterial-small molecule coupling can increase the affinity between the magnetic nanomaterials and the corresponding surface receptors of malignant cells. For instance, folic acid receptors are overexpressed in different human tumors, including ovarian, lung, breast, endometrial, kidney, and colon cancer. The recent applicable materials in surface modification include high molecular polymers, surfactants, and inorganic coatings. See Table 1 for details [34].

4. Magnetic Nanomaterials Applications in Tumor Diagnosis

4.1. Magnetic Nanomaterial Applications in Magnetic Resonance Imaging. Magnetic resonance imaging (MRI) is a widely used noninvasive medical diagnostic technique. MR image has unique advantages in diagnosing various tumors such as liver cancer, cervical cancer, ovarian cancer, glioma, and other tumors [35]. Magnetic resonance imaging uses radio frequency (RF) electromagnetic waves to motivate nuclear materials with nonzero spins in a magnetic field—mainly hydrogen atoms—to generate nuclear magnetic resonance (NMR). The induction coil detection technology is used to obtain tissue relaxation information and proton density information (acquisition resonance signal). Finally, mathematical image reconstruction has been used in different techniques to construct magnetic resonance images [36]. During NMR imaging, the RF pulses are stopped to transmit the resonated hydrogen atom in the body. The relaxation process aims to restore the high energy nucleus to equilibrium, and the time experienced by this process is called the relaxation time. The relaxation time is divided into T1 and T2, where T1 is called longitudinal relaxation time, and T2 is called transverse relaxation time [37]. The currently used contrast agents are divided into T1 inhibitors such as paramagnetic metal ions Gd³⁺, Mn²⁺, etcetera, and

T2 inhibitors, including superparamagnetic and ferromagnetic substances. Due to the efficient magnetism of the magnetic nanomaterials, they have been broadly utilized in magnetic resonance imaging research. The superparamagnetic iron oxide (SPIOs) nanomaterials are famously used in MRI imaging; they significantly enhance the contrast of T2WI images. Currently, Daou et al. reported the use of nanoparticle alloys such as FePt and MnZnFe as MRI contrast agents [38].

4.2. Magnetic Nanomaterial Applications in PET-CT Imaging. Positron emission computed tomography (PET-CT) is a commonly used noninvasive clinical examination in the tumor diagnosis and prognosis. The chelated 2-fluoro-2-deoxy-D-glucose (18F-FDG) with small molecules or antibodies is a commonly used contrast agent [39]. In recent preclinical studies, the radioactive-labeled magnetic nanoparticles have been proved very promising in cancer diagnosis. It has three significant advantages compared with traditional imaging techniques: (1) the magnetic nanoparticles labeled with radioactive tracer possess precision targeting due to the EPR effect, (2) magnetic nanoparticles have a high surface to volume ratio, allowing the use of high-density radioactive labels, and (3) obtainable complementary multimodal imaging, for instance, utilizing different radionuclide nanoparticles in integrated imaging [40]. Pratt et al. found that chelating radionuclides on the surface of small and biocompatible magnetic nanoparticles improved the accuracy and specificity of early tumor diagnosis, also using the advantages of PET scan of displaying the changes in tissue functions [41].

4.3. Biofluorescence Imaging. Bioluminescence imaging obtains optical images given fluorescence characteristics changes. At the cellular level, fluorescent nanomaterials act as fluorescent probes enter the cells in both active transport and passive diffusion due to their small size; at the organism level, the nanoparticles enter the bloodstream, then exuded and enriched in the tumor lesion due to the high permeability of tumor blood vessels. CL et al. combined magnetic nanoparticles with fluorescent materials to prepare magnetic fluorescent nanocomposites that are both superparamagnetic and fluorescent. When the magnetic fluorescent nanocomposites are introduced into living cells, the fluorescence can be traced and controlled to be enriched at the desired location upon applying an external magnetic field, which dramatically improves the efficiency of cell imaging [42].

4.4. Hybrid Imaging Model. Different imaging techniques comprise certain advantages and disadvantages, and yet, there is no ideal technique. A single imaging technique cannot guarantee optimal performance in different cases. Nevertheless, hybrid imaging can integrate the advantages of several techniques to address the inherent limitations of a single imaging technique [43]. For instance, PET-CT is a renowned sensitive tumor diagnostic tool, while MRI can provide more anatomical information through high-resolution images [44]. Therefore, combining these two imaging techniques can provide higher sensitivity and more

detailed anatomical information in tumor diagnosis. Nanomaterials can possess precision targeting properties through surface modification and could be used as contrast agents in imaging technology. Tracking the contrast agent's enrichment in the body helps determine surgery scope and facilitate the procedure, i.e., employing fluorescence imaging. It can also ensure whether tumor tissues are entirely removed or not, i.e., performing MRI analysis. Besides, the tumors' occurrence and progression can be tracked and identified, i.e., utilizing PET-CT [45]. The recent hybrid imaging techniques are MRI/fluorescence imaging and PET-CT/MR imaging [46]. Therefore, diagnosis accuracy can be improved, and better cancer therapeutics can be developed.

5. Magnetic Nanomaterial Applications and Research in Tumor Therapy

Recently, radiotherapy and (or) chemotherapy are commonly used as initial treatment combined with surgery [47]. However, different factors, including genetic alterations, could promote tumor drug resistance by dysfunctioning the cellular transport mechanisms and reducing drug efficiency and cellular detoxification capability. These adverse effects restrict the administrated drug dosage to patients [48].

5.1. Magnetic Nanomaterial Applications as Drug Carriers. With the vigorous development of the nanotechnology, has more and more attention has been paid to nanocarriers. Nanoparticles have good biocompatibility and less immune reaction, coupling with other ligands or antibodies after easily into the organization or the specific antigen specificity and cell surface receptors, or be swallowed up by the target cell into the cell, the DNA of the implementation of transshipment. It is also released in cells with high gene transfer efficiency [49]. Magnetic nanoparticles, especially paramagnetic and superparamagnetic ferrite nanoparticles, have become an objective material in drug carriers' development [50]. The ferrite nanoparticles are primarily made of iron-containing particles or other active ingredients containing iron. It has been proven that ferrite nanoparticles exhibit decent biocompatibility and can be entirely metabolized. Moreover, it has robust and distinct drug-loading capabilities. Various antibodies, antigens, small molecules, polypeptides, and active proteins can be loaded on the modified nanoparticles' surface. Different examples can present the mode of action of the modified nanoparticles; for instance, through the antigen-antibody reaction in the body or under the guidance of an external magnetic field, these targeted antigen-loaded nanoparticles are enriched in the tumor lesions, concentrating the accumulation of the antibodies to the target tumor cells to achieve the optimal therapeutic potential [51]. Recently, the nanoparticle preparation process is relatively mature. A complex combination of tumor suppressor genes, antitumor monoclonal antibodies, and antitumor drugs such as doxorubicin, paclitaxel, and cisplatin, can be integrated to establish a distinct advantageous microcarrier system that possesses magnetism, bioapplicability, and capability to cross the blood-brain barrier. Following the previously mentioned basis of establishing microcarrier systems,

the “three-stage carrier rocket theory” is proposed to provide a basis for tumor-targeted therapy [52]. Magnetic nanomaterials are proposed in the 1970s as carriers in targeted therapeutics, which has been recently shown as an ideal application [53]. For instance, the MNP-HP-CP complex has been synthesized using magnetic nanoparticles (MNPs) coated with heparin (HP) and embedded with cisplatin (CP) by solvent evaporation and emulsification crosslinking. The MNP-HP-CP complex intake by human ovarian cancer cells CP70 promoted cell apoptosis [54]. These findings proved the feasibility of magnetic nanomaterials as drug carriers. It has also been shown that this magnetic nanomaterial composite is biocompatible, minimally cytotoxic, and sustains the release of cisplatin [55].

Although paclitaxel is an essential drug in ovarian cancer treatment, its high administrated dose may cause severe allergic reactions and dramatically limits its therapeutic effect [56]. On the other hand, the polyethylene glycol- (PEG-) triethoxysilane (APTES)- (PA-) modified magnetic nanomaterial packed with paclitaxel and doxorubicin precisely delivered the paclitaxel and doxorubicin to tumor cells, alleviating adverse side effects and sustaining the drug concentration in the tumor tissue [57] and increasing the therapeutic effect of paclitaxel.

5.2. Magnetic Nanomaterial Applications in Tumor Hyperthermia. Tumor hyperthermia refers to heat augmentation tumor treatment. Tumor hyperthermia is renowned as the fifth therapeutic approach after surgery, radiotherapy, chemotherapy, and immunotherapy [58]. It employs physical energy to elevate a particular or whole-body heat so that the tumor tissue temperature rises to a certain level and duration. Within specific time and temperature, tumor cells die without affecting healthy cells due to the different temperature tolerance between healthy and tumor cells [59]. When the temperature range is 40-42°C, the tumor cell fluidity is enhanced, the structure is weakened, and the viability is lost. High temperature injuriously affects the tumor cells' endoplasmic reticulum, lysosomal membrane, and mitochondrial membrane, promoting cell death. The high temperature also inhibits the polymerase and ligase activity, repressing the synthesis of nucleic acids. Besides, the tumors' surrounding blood vessels are characterized by abundant blood flow, abnormal vascular structure, twisted blood vessel shape, and high blood flow resistance and enable blood vessel thrombosis or occlusion. During hyperthermia, healthy and tumor tissues' temperature increases; however, because of the optimal blood circulation in healthy tissues rather than tumor tissues, the heat poorly dissipated and eventually rises, killing tumor cells. Jordan et al. reported the unprecedented use of magnetic nanoparticles in tumor hyperthermia and proposed magnetic fluid hyperthermia (MFH) conceptualization [60]. The magnetism and adequate water solubility of magnetic fluids fostered its uses in clinical applications. Applying an external alternating magnetic field (AMF) over magnetic nanoparticles converts the magnetic energy into heat and steadily increases local tumor tissue temperature, thereby suppressing tumor cell growth [61]. Studies have shown that compared to pacli-

taxel cytotoxicity under normal body temperature, 30 minutes of constant heating at 43°C can significantly increase paclitaxel cytotoxicity by 10-100 times [62]. Secord et al. reported that the PEG-modified liposome nanoparticle-adriamycin complex combined with abdominal hyperthermia exhibited better precision, outcome, and drug uptake in tumor tissues [63].

5.3. Magnetic Nanomaterial Applications in Photodynamic Tumor Therapy. Photodynamic therapy is a new therapeutic technique that combines photosensitizer with the corresponding illuminant to destroy tumor tissue through selective photodynamic reactions [64]. The photosensitizer is the key for photodynamic therapy. Conventional photosensitizers include porphyrins, chlorin, and bacteriochlorin/phthalocyanines. However, due to low hydrophilicity and possible aggregation, traditional photoactive molecules are limited in biomedical applications. It is thus urgent to improve the photosensitizers' water solubility and biocompatibility [65].

The emergence of nanomaterials provides a new aspect in developing photoactive molecules. They can be used as new carriers for photoactive molecules and improving the photosensitizers' biocompatibility. Moreover, the self-targeting nanomaterial enables sufficient photosensitizer enrichment in the tumor tissue, improving tumor therapeutic effects, and reducing the photosensitizer's adverse effects [66]. Recently, gold nanomaterials, carbon-based nanomaterials, and silica nanomaterials are the major substances in photodynamic therapy. These nanomaterials have a high drug-loading capacity and can efficiently boost tumor photothermal therapy [67]. Besides, photodynamic therapy, chemotherapy, hyperthermia, and other tumor therapies can be integrated by constructing multifunctional nanomaterials to achieve multitherapeutic synergy, which is favorable in cancer treatment [68].

6. Prospect

The constant nanotechnology and magnetic nanomaterial development have made significant progress in cancer diagnostics and therapeutics. Magnetic nanomaterials are widely used in MRI/PET-CT imaging, antitumor drug carriers, magnetic fluid hyperthermia, and different fields. However, their application remains preclinical and yet to be applicable in clinical trials [69]. Primarily, we need a comprehensive study on the multifunctional magnetic nanomaterials' biosafety, distribution, long-term toxicity, synthesis, elemental composition, size, surface modification, and metabolism in vivo. With the rapid development of magnetic nanomaterials, nanotechnology, and biotechnology, magnetic nanomaterials can be widely used in cancer diagnosis and treatment in the future.

7. Conclusion

Magnetic nanoparticles not only have the general characteristics of nanoparticles but also have magnetic properties, which have become the research focus in the field of nanomedicine in recent years. Magnetic nanoparticles are widely

used in biomedicine, drug gene delivery, magnetic resonance imaging, molecular probe, tumor detection, tumor therapy, and other fields due to their unique properties. With the development of nanotechnology, magnetic nanoparticles will be more widely used in tumor diagnosis and treatment.

Conflicts of Interest

The authors declare that they have no conflict of interest in this work.

Authors' Contributions

Xuefeng Bian and Ting Guo contributed equally to this work.

Acknowledgments

The work is financially supported by the National Natural Science Foundation of China (81571797), Social Development Plan of Taizhou, China (TS202004), the Natural Science Foundation of Nanjing University of Chinese Medicine (XZR2020093), China, Taizhou People's Hospital Medical Innovation Team Foundation, China (CXTDA201901), and Scientific Research Foundation of Taizhou People's Hospital, China (ZL202023).

References

- [1] Global Burden of Disease Cancer Collaboration, "Global, Regional, and National Cancer Incidence, Mortality, Years of Life Lost, Years Lived With Disability, and Disability-Adjusted Life-Years for 29 Cancer Groups, 1990 to 2017," *JAMA Oncology*, vol. 5, no. 12, pp. 1749–1768, 2019.
- [2] P. Muller, S. Walters, M. P. Coleman, and L. Woods, "Which indicators of early cancer diagnosis from population-based data sources are associated with short-term mortality and survival?," *Cancer Epidemiology*, vol. 56, pp. 161–170, 2018.
- [3] I. Lilienthal and N. Herold, "Targeting molecular mechanisms underlying treatment efficacy and resistance in osteosarcoma: a review of current and future strategies," *International Journal of Molecular Sciences*, vol. 21, no. 18, p. 6885, 2020.
- [4] M. Aflori, "Smart nanomaterials for biomedical applications—a review," *Nanomaterials (Basel)*, vol. 11, no. 2, p. 396, 2021.
- [5] S. Caspani, R. Magalhães, J. P. Araújo, and C. T. Sousa, "Magnetic Nanomaterials as Contrast Agents for MRI," *Materials*, vol. 13, no. 11, p. 2586, 2020.
- [6] Y.-P. Wang, Y.-T. Liao, C.-H. Liu et al., "Trifunctional Fe₃O₄/CaP/alginate core-shell-corona nanoparticles for magnetically guided, pH-responsive, and chemically targeted chemotherapy," *ACS Biomaterials Science & Engineering*, vol. 3, no. 10, pp. 2366–2374, 2017.
- [7] N. D. Thorat, R. A. Bohara, S. A. M. Tofail et al., "Superparamagnetic Gadolinium Ferrite Nanoparticles with Controllable Curie Temperature - Cancer Theranostics for MR-Imaging-Guided Magneto-Chemotherapy," *European Journal of Inorganic Chemistry*, vol. 2016, pp. 4586–4597, 2016.
- [8] N. D. Thorat, R. A. Bohara, and V. Malgras, "Multimodal Superparamagnetic Nanoparticles with Unusually Enhanced Specific Absorption Rate for Synergetic Cancer Therapeutics and Magnetic Resonance Imaging," *ACS Applied Materials & Interfaces*, vol. 8, no. 23, pp. 14656–14664, 2016.
- [9] H. Shimoshige, Y. Nakajima, H. Kobayashi et al., "Formation of Core-Shell Nanoparticles Composed of Magnetite and Samarium Oxide in *Magnetospirillum magneticum* Strain RSS-1," *PLoS one*, vol. 12, no. 1, p. e0170932, 2017.
- [10] A. P. Plan Sangnier, S. Preveral, A. Curcio et al., "Targeted thermal therapy with genetically engineered magnetite : Photothermia is far more efficient than magnetic hyperthermia," *Journal of Controlled Release*, vol. 279, pp. 271–281, 2018.
- [11] P. Yáñez-Sedeño, A. González-Cortés, S. Campuzano, and J. M. Pingarrón, "Multimodal/Multifunctional Nanomaterials in (Bio)electrochemistry: Now and in the Coming Decade," *Nanomaterials*, vol. 10, no. 12, p. 2556, 2020.
- [12] J. Wojnarowicz, T. Chudoba, and W. Lojowski, "A review of microwave synthesis of zinc oxide nanomaterials: reactants, process parameters and morphologies," *Nanomaterials (Basel)*, vol. 10, no. 6, p. 1086, 2020.
- [13] E. Barrios, D. Fox, Y. Y. L. Sip et al., "Nanomaterials in Advanced, High-Performance Aerogel Composites: A Review," *Polymers*, vol. 11, no. 4, p. 726, 2019.
- [14] H. J. Deng and Z. L. Lei, "Preparation and characterization of hollow Fe₃O₄/SiO₂@PEG-PLA nanoparticles for drug delivery," *Composites: Part B*, vol. 54, pp. 194–199, 2013.
- [15] D. W. Ye, Y. Li, and N. Gu, "Magnetic labeling of natural lipid encapsulations with iron-based nanoparticles," *Nano Research*, vol. 11, no. 6, pp. 2970–2991, 2018.
- [16] H. Lee, J. Han, H. Shin, H. Han, K. Na, and H. Kim, "Combination of chemotherapy and photodynamic therapy for cancer treatment with sonoporation effects," *Journal of Controlled Release*, vol. 283, pp. 190–199, 2018.
- [17] J. Lu, J. Sun, F. Li et al., "Highly Sensitive Diagnosis of Small Hepatocellular Carcinoma Using pH-Responsive Iron Oxide Nanocluster Assemblies," *Journal of the American Chemical Society*, vol. 140, no. 32, pp. 10071–10074, 2018.
- [18] T. Ojha, V. Pathak, Y. Shi et al., "Pharmacological and physical vessel modulation strategies to improve EPR-mediated drug targeting to tumors," *Advanced Drug Delivery Reviews*, vol. 119, pp. 44–60, 2017.
- [19] K. Mylkie, P. Nowak, P. Rybczynski, and M. Ziegler-Borowska, "Polymer-Coated Magnetite Nanoparticles for Protein Immobilization," *Materials*, vol. 14, no. 2, p. 248, 2021.
- [20] H. Jiang, H. Wu, Y. L. Xu, J. Z. Wang, and Y. Zeng, "Preparation of galactosylated chitosan/tripolyphosphate nanoparticles and application as a gene carrier for targeting SMMC7721 cells," *Journal of Bioscience and Bioengineering*, vol. 111, no. 6, pp. 719–724, 2011.
- [21] P. Pradhan, J. Giri, F. Rieken et al., "Targeted temperature sensitive magnetic liposomes for thermo-chemotherapy," *Journal of Controlled Release*, vol. 142, no. 1, pp. 108–121, 2010.
- [22] S. Laurent, D. Forge, M. Port et al., "Magnetic iron oxide nanoparticles: synthesis, stabilization, vectorization, physicochemical characterizations, and biological applications," *Chemical Reviews*, vol. 108, no. 6, pp. 2064–2110, 2008.
- [23] M. Kumagai, T. K. Sarma, H. Cabral et al., "Enhanced in vivo magnetic resonance imaging of tumors by PEGylated iron-oxide-gold core-shell nanoparticles with prolonged blood circulation Properties," *Macromolecular Rapid Communications*, vol. 31, no. 17, pp. 1521–1528, 2010.
- [24] M. Liang, A. Yang, Y. Zhu, and S. Sun, "Effect of nanoparticles' size and shape on thermodynamics properties of PI/SiO₂

- Nanocomposites,” *Nano brief reports and reviews*, vol. 15, no. 03, p. 2050041, 2020.
- [25] C. Liu, X. Wu, T. Klemmer, N. Shukla, and D. Weller, “Reduction of sintering during annealing of FePt nanoparticles coated with iron oxide,” *Chemistry of Materials*, vol. 17, no. 3, pp. 620–625, 2005.
- [26] H. R. Rajabi, R. Naghiha, M. Kheirizadeh, H. Sadatfaraji, A. Mirzaei, and Z. M. Alvand, “Microwave assisted extraction as an efficient approach for biosynthesis of zinc oxide nanoparticles: Synthesis, characterization, and biological properties,” *Materials Science and Engineering: C*, vol. 78, pp. 1109–1118, 2017.
- [27] S. Ge, X. Shi, K. Sun et al., “Facile Hydrothermal Synthesis of Iron Oxide Nanoparticles with Tunable Magnetic Properties,” *The Journal of Physical Chemistry C*, vol. 113, no. 31, pp. 13593–13599, 2009.
- [28] S. R. Bhattarai, R. B. Kc, S. Y. Kim et al., “N-hexanoyl chitosan stabilized magnetic nanoparticles: implication for cellular labeling and magnetic resonance imaging,” *J. Nanobiotechnology*, vol. 6, no. 1, p. 1, 2008.
- [29] G. Wang, S. Gao, R. Tian et al., “Theranostic hyaluronic acid-iron micellar nanoparticles for magnetic-field-enhanced in vivo cancer chemotherapy,” *Chem Med Chem.*, vol. 13, no. 1, pp. 78–86, 2018.
- [30] J. K. Lewis, J. C. Bischof, I. Braslavsky et al., “The Grand Challenges of Organ Banking: Proceedings from the first global summit on complex tissue cryopreservation,” *Cryobiology*, vol. 72, no. 2, pp. 169–182, 2016.
- [31] Y. B. Zhou, Z. M. Tang, C. L. Shi, S. Shi, Z. Qian, and S. Zhou, “Polyethylenimine functionalized magnetic nanoparticles as a potential non-viral vector for gene delivery,” *Journal of Materials Science-Materials in Medicine.*, vol. 23, no. 11, pp. 2697–2708, 2012.
- [32] F. Fan, J. Sun, B. Chen et al., “Rotating magnetic field-controlled fabrication of magnetic hydrogel with spatially disk-like microstructures,” *Science China Materials*, vol. 61, no. 8, pp. 1112–1122, 2018.
- [33] H. Shokrollahi and A. Khorramdin, “Magnetic resonance imaging by using nano-magnetic particles,” *Journal of Magnetism and Magnetic Materials*, vol. 369, no. 11, pp. 176–183, 2014.
- [34] X. Shi, S. H. Wang, S. D. Swanson et al., “Dendrimer-Functionalized Shell-crosslinked Iron Oxide Nanoparticles for In-Vivo Magnetic Resonance Imaging of Tumors,” *Advanced Materials*, vol. 20, no. 9, pp. 1671–1678, 2008.
- [35] J. Park, N. R. Kadasala, S. A. Abouelmagd et al., “Polymer-iron oxide composite nanoparticles for EPR-independent drug delivery,” *Biomaterials*, vol. 101, pp. 285–295, 2016.
- [36] A. H. Rezayan, M. Mousavi, S. Kheirjou, G. Amoabediny, M. S. Ardestani, and J. Mohammadnejad, “Monodisperse magnetite (Fe₃O₄) nanoparticles modified with water soluble polymers for the diagnosis of breast cancer by MRI method,” *Journal of Magnetism and Magnetic Materials*, vol. 420, no. 15, pp. 210–217, 2016.
- [37] T. J. Daou, G. Pourroy, J. M. Greneche, A. Bertin, D. Felder-Flesch, and S. Begin-Colin, “Water soluble dendronized iron oxide nanoparticles,” *Dalton Transactions*, vol. 23, pp. 4442–4449, 2009.
- [38] Z. Liu, S. Tabakman, K. Welsher, and H. Dai, “Carbon nanotubes in biology and medicine: In vitro and in vivo detection, imaging and drug delivery,” *Nano Research*, vol. 2, no. 2, pp. 85–120, 2009.
- [39] C. M. Tempany, K. H. Zou, S. G. Silverman, D. L. Brown, A. B. Kurtz, and B. J. McNeil, “Staging of Advanced Ovarian Cancer: Comparison of Imaging Modalities—Report from the Radiological Diagnostic Oncology Group,” *Radiology*, vol. 215, pp. 761–767, 2000.
- [40] E. C. Pratt, T. M. Shaffer, and J. Grimm, “Nanoparticles and radiotracers: advances toward radionanomedicine,” *Wiley Interdisciplinary Reviews: Nanomedicine and Nanobiotechnology*, vol. 8, no. 6, pp. 872–890, 2016.
- [41] C. Yu, J. Zhai, Z. Li, M. Wan, M. Gao, and L. Jiang, “Water-assisted self-assembly of polyaniline/Fe₃O₄ composite honeycomb structures film,” *Thin Solid Films*, vol. 516, no. 15, pp. 5107–5110, 2008.
- [42] I. Venugopal, S. Pernal, A. Duproz, J. Bentley, H. Engelhard, and A. Linninger, “Magnetic field-enhanced cellular uptake of doxorubicin loaded magnetic nanoparticles for tumor treatment,” *Materials Research Express*, vol. 3, no. 9, p. 095010, 2016.
- [43] K. Wu, S.-H. Liao, C.-H. Liu et al., “Functionalized magnetic iron oxide/alginate core-shell nanoparticles for targeting hyperthermia,” *International Journal of Nanomedicine*, vol. 10, pp. 3315–3328, 2015.
- [44] M. P. Arachchige, S. S. Laha, A. R. Naik, K. T. Lewis, R. Naik, and B. P. Jena, “Functionalized nanoparticles enable tracking the rapid entry and release of doxorubicin in human pancreatic cancer cells,” *Micron*, vol. 92, pp. 25–31, 2017.
- [45] Y. Cui, M. Zhang, F. Zeng, H. Jin, Q. Xu, and Y. Huang, “Dual-targeting magnetic PLGA nanoparticles for codelivery of paclitaxel and curcumin for brain tumor therapy,” *ACS APPLIED MATERIALS & INTERFACES.*, vol. 8, no. 47, pp. 32159–32169, 2016.
- [46] L. Yang, Y. T. Tseng, G. Suo et al., “Photothermal therapeutic response of cancer cells to aptamer-gold nanoparticle-hybridized graphene oxide under NIR illumination,” *ACS Applied Materials & Interfaces*, vol. 7, no. 9, pp. 5097–5106, 2015.
- [47] C. Costa, F. Brandão, M. J. Bessa et al., “In vitro cytotoxicity of superparamagnetic iron oxide nanoparticles on neuronal and glial cells. Evaluation of nanoparticle interference with viability tests,” *Journal of Applied Toxicology*, vol. 36, no. 3, pp. 361–372, 2016.
- [48] M. Lin, J. X. Huang, J. Zhang et al., “The therapeutic effect of PEI-Mn_{0.5}Zn_{0.5}Fe₂O₄ nanoparticles/pEgr1-HSV-TK/GCV associated with radiation and magnet-induced heating on hepatoma,” *Nanoscale*, vol. 5, no. 3, pp. 991–1000, 2013.
- [49] S. M. Dadfar, K. Roemhild, N. I. Drude et al., “Iron oxide nanoparticles: Diagnostic, therapeutic and theranostic applications,” *Advanced Drug Delivery Reviews*, vol. 138, pp. 302–325, 2019.
- [50] Y. Liu, F. Yang, C. Yuan et al., “Magnetic Nanoliposomes as In Situ Microbubble Bombers for Multimodality Image-Guided Cancer Theranostics,” *ACS Nano*, vol. 11, no. 2, pp. 1509–1519, 2017.
- [51] Y. Zhang, X. Liu, E. Peng et al., “Facile synthesis of water-dispersible magnetite nanorings from surfactant-free hematite nanorings,” *Micro & Nano Letters*, vol. 11, no. 12, pp. 814–818, 2016.
- [52] K. J. Yong, C. Gao, J. S. J. Lim et al., “Oncofetal gene SALL4 in aggressive hepatocellular carcinoma,” *New England Journal of Medicine*, vol. 368, no. 24, pp. 2266–2276, 2013.
- [53] C. Sanchez, “Advanced nanomaterials: A domain where chemistry, physics and biology meet,” *Comptes Rendus Chimie*, vol. 13, no. 1–2, pp. 1–2, 2010.

- [54] J. Xiong, "SALL4: Engine of Cell Stemness," *Current Gene Therapy*, vol. 14, no. 5, pp. 400–411, 2014.
- [55] Z. Shen, T. Chen, X. Ma et al., "Multifunctional Theranostic Nanoparticles Based on Exceedingly Small Magnetic Iron Oxide Nanoparticles for T1-Weighted Magnetic Resonance Imaging and Chemotherapy," *ACS Nano*, vol. 11, no. 11, pp. 10992–11004, 2017.
- [56] S. S. Zeng, T. Yamashita, M. Kondo et al., "The transcription factor SALL4 regulates stemness of EpCAM-positive hepatocellular carcinoma," *Journal of Hepatology*, vol. 60, no. 1, pp. 127–134, 2014.
- [57] C. Wu, Y. Shen, M. Chen, K. Wang, Y. Li, and Y. Cheng, "Recent Advances in magnetic nanomaterial-based mechanotransduction for cell fate regulation," *Advanced Materials*, vol. 30, no. 17, p. 1705673, 2018.
- [58] M. Fiorillo, A. F. Verre, M. Iliut et al., "Graphene oxide selectively targets cancer stem cells, across multiple tumor types: Implications for non-toxic cancer treatment, via "differentiation-based nano-therapy," *Oncotarget*, vol. 6, no. 6, pp. 3553–3562, 2015.
- [59] Z. Wang, J. Tan, C. McConville et al., "Poly lactic-co-glycolic acid controlled delivery of disulfiram to target liver cancer stem-like cells," *Nanomedicine: Nanotechnology, Biology and Medicine*, vol. 13, no. 2, pp. 641–657, 2017.
- [60] H. Sun, S. He, B. Wen, W. Jia, E. Fan, and Y. Zheng, "Effect of Biejiajian Pills on Wnt signal pathway molecules β -catenin and GSK-3 β and the target genes CD44v6 and VEGF in hepatocellular carcinoma cells," *Nan Fang Yi Ke Da Xue Xue Bao*, vol. 34, no. 10, pp. 1454–1458, 2014.
- [61] Y.-Y. Lu, J.-J. Wang, X.-K. Zhang, W.-B. Li, and X.-L. Guo, "1118-20, an indazole diarylurea compound, inhibits hepatocellular carcinoma HepG2 proliferation and tumour angiogenesis involving Wnt/ β -catenin pathway and receptor tyrosine kinases," *Journal of Pharmacy and Pharmacology*, vol. 67, no. 10, pp. 1393–1405, 2015.
- [62] Z. Gao, Y. Hou, J. Zeng et al., "Tumor Microenvironment-triggered Aggregation of Antiphagocytosis^{99m}Tc-Labeled Fe₃O₄nanoprobes for enhanced tumor imaging in vivo," *Advanced Materials*, vol. 29, no. 24, p. 1701095, 2017.
- [63] X. Ke, Y. Zhao, X. Lu et al., "TQ inhibits hepatocellular carcinoma growth in vitro and in vivo via repression of Notch signaling," *Oncotarget*, vol. 6, pp. 32610–32621, 2015.
- [64] R. Dhanasekaran, I. Nakamura, C. Hu et al., "Activation of the transforming growth factor- β /SMAD transcriptional pathway underlies a novel tumor-promoting role of sulfatase 1 in hepatocellular carcinoma," *Hepatology*, vol. 61, no. 4, pp. 1269–1283, 2015.
- [65] H. Zhang, X. L. Liu, Y. F. Zhang et al., "Magnetic nanoparticles based cancer therapy: Current status and applications," *Science China. Life Sciences*, vol. 61, no. 4, pp. 400–414, 2018.
- [66] M. Niederberger, "Multiscale nanoparticle assembly: From particulate precise manufacturing to colloidal processing," *Advanced Functional Materials*, vol. 27, no. 47, p. 1703647, 2017.
- [67] L. Deng, J. H. Stafford, S.-C. Liu et al., "SDF-1 Blockade Enhances Anti-VEGF Therapy of Glioblastoma and Can Be Monitored by MRI," *Neoplasia*, vol. 19, no. 1, 2016.
- [68] Y. Li, Y. Deng, X. Tian et al., "Multi-pronged design of light-triggered nanoparticles to overcome cisplatin resistance for efficient ablation of resistant tumor," *ACS Nano*, vol. 9, no. 10, pp. 9626–9637, 2015.
- [69] L. P. Singh, S. K. Srivastava, R. Mishra, and R. S. Ningthoujam, "Multifunctional hybrid nanomaterials from water dispersible CaF₂:Eu³⁺, Mn²⁺ and Fe₃O₄ for luminescence and hyperthermia application," *Journal of Physical Chemistry C*, vol. 118, no. 31, pp. 18087–18096, 2014.
- [70] H. Unterweger, L. Dézsi, J. Matuszak et al., "Dextran-coated superparamagnetic iron oxide nanoparticles for magnetic resonance imaging: evaluation of size-dependent imaging properties, storage stability and safety," *International Journal of Nanomedicine*, vol. 13, pp. 1899–1915, 2018.
- [71] M. Ebadi, S. Bullo, K. Buskaran, M. Z. Hussein, and S. Fakurazi, "Synthesis and properties of magnetic nanotheranostics coated with polyethylene glycol/5-fluorouracil/layered double hydroxide," *International Journal of Nanomedicine*, vol. 14, pp. 6661–6678, 2019.
- [72] A. Krzywicka and E. Megiel, "Silver-polystyrene (Ag/PS) nanocomposites doped with polyvinyl Alcohol (PVA)-fabrication and bactericidal activity," *Nanomaterials (Basel)*, vol. 10, no. 11, p. 2245, 2020.
- [73] J. Lojk, V. B. Bregar, M. Rajh et al., "Cell type-specific response to high intracellular loading of polyacrylic acid-coated magnetic nanoparticles," *International Journal of Nanomedicine*, vol. 10, pp. 1449–1462, 2015.
- [74] A. Rajan, M. Sharma, and N. K. Sahu, "Assessing magnetic and inductive thermal properties of various surfactants functionalised Fe₃O₄ nanoparticles for hyperthermia," *Scientific Reports*, vol. 10, no. 1, p. 15045, 2020.
- [75] J.-H. Lee, S.-M. You, K. Luo, J.-S. Ko, A.-H. Jo, and Y.-R. Kim, "Synthetic ligand-coated starch magnetic microbeads for selective extraction of food additive silicon dioxide from commercial processed food," *Nanomaterials (Basel)*, vol. 11, no. 2, p. 532, 2021.
- [76] T. Nguyen, F. Mhammeri, and S. Ammar, "Iron Oxide and Gold Based Magneto-Plasmonic Nanostructures for Medical Applications: A Review," *Nanomaterials*, vol. 8, no. 3, p. 149, 2018.
- [77] X. Yuan, X. Zhang, S. Lu, Y. Wei, and X. Wei, "Cellular Toxicity and Immunological Effects of Carbon-based Nanomaterials," *Particle and Fibre Toxicology*, vol. 16, no. 1, 2019.

Research Article

Evaluation of Inflammatory and Calcification after Implantation of Bioabsorbable Poly-L-Lactic Acid/Amorphous Calcium Phosphate Scaffolds in Porcine Coronary Arteries

Gaoke Feng ^{1,2,3}, Chaoshi Qin,⁴ Fei Sha,⁵ Yongnan Lyu,^{1,2,3} Jinggang Xia,⁶ and Xuejun Jiang ^{1,2,3}

¹Department of Cardiology, Renmin Hospital of Wuhan University, Wuhan 430060, China

²Cardiovascular Research Institute, Wuhan University, Wuhan 430060, China

³Hubei Key Laboratory of Cardiology, Wuhan 430060, China

⁴Department of Cardiology, Tangdu Hospital, Fourth Military Medical University, Xi'an 710038, China

⁵Department of Vascular Surgery, Wang Jing Hospital, China Academy of Chinese Medical Sciences, Beijing 100102, China

⁶Department of Cardiology, Xuanwu Hospital, Capital Medical University, Beijing 100053, China

Correspondence should be addressed to Gaoke Feng; 123fgk@163.com and Xuejun Jiang; xjjiang@tom.com

Received 1 November 2020; Revised 1 January 2021; Accepted 9 January 2021; Published 23 January 2021

Academic Editor: Luis Jesús Villarreal-Gómez

Copyright © 2021 Gaoke Feng et al. This is an open access article distributed under the Creative Commons Attribution License, which permits unrestricted use, distribution, and reproduction in any medium, provided the original work is properly cited.

Purpose. Our previous research has confirmed that the addition of nano-amorphous calcium phosphate (ACP) materials can improve the support of poly-L-lactic acid (PLLA) vascular scaffolds. Based on this, we continued to explore the effect of novel bioresorbable scaffold composed of PLLA and ACP nanoparticles on inflammation and calcification of surrounding tissues after scaffold implantation in porcine coronary artery. **Methods.** PLLA/ACP scaffolds in the experimental group and PLLA scaffolds in the control group were implanted into the coronary arteries of small pigs. Serum levels of C-reactive protein (CRP), calcium (Ca), and alkaline phosphatase (ALP) were measured before implantation and at 1, 6, 12, and 24 months after operation. Intravascular ultrasonography (IVUS) was performed to evaluate the vascular calcification score. The scaffold and surrounding tissues were hematoxylin-eosin staining for inflammation score. The scaffold and surrounding tissues were stained with NF- κ B and ALP, and the positive expression index was calculated. Western blot was used to detect the expression of IL-6 and BMP-2 in the tissues around the scaffold. **Results.** There was no statistically significant difference between the two groups in CRP, calcium, and ALP at preimplant, 1 month, 6 months, 12 months, and 24 months ($P > 0.05$). The inflammation score, NF- κ B positive expression index, and calcification score in the PLLA/ACP group were lower than that in the PLLA group at 12 months and 24 months ($P < 0.05$). The ALP positive expression index in the PLLA/ACP group was lower than that in the PLLA group at 6 months, 12 months, and 24 months ($P < 0.05$). Western blot results showed that the IL-6 expression level in the PLLA/ACP group was significantly lower than that in the control group at 6 months, 12 months, and 24 months ($P < 0.05$). The expression of BMP-2 in the PLLA/ACP group was significantly lower than that in the control group at 12 months and 24 months ($P < 0.05$). **Conclusion.** The PLLA/ACP composite scaffold has good biocompatibility. The incorporation of nanoscale ACP can reduce the inflammatory response caused by the acid metabolites of PLLA scaffolds, reduce the expression of procalcification factors in the body, and inhibit tissue calcification. The PLLA/ACP composite scaffold provides reliable guidance for the application and development of degradable vascular scaffold.

1. Introduction

Bioabsorbable scaffold is the mainstream direction of interventional therapy for coronary heart disease. At present, the

bioabsorbable scaffolds represented by PLLA have a promising prospect in clinical practice on the basis of their biodegradable ability and support performance. However, poly-L-lactic acid material (PLLA) has its own limitations,

and its support performance is less than that of metal scaffold [1, 2]. Besides, during the degradation of PLA materials *in vivo*, it may produce lactic acid, an acid metabolite, which may cause long term and chronic stimulation to the tissue around the scaffold. Consequently, it may induce and aggravate inflammatory reaction and delay vascular healing [3]. Considering the above interpretations, it may eventually lead to slow development of PLLA scaffold and the de-listing of Abbott BVS scaffold [4]. In order to improve the biocompatibility and mechanical properties of PLLA, our study for the first time added nano-scale amorphous calcium phosphate (ACP) into PLLA to form a new-type vascular scaffold blended by bioceramic and polymer. ACP is a bioceramic material featured by high hardness, good biological activity, good biocompatibility, and strong cell affinity [5, 6]. Previous experiment of our research group proved that PLLA/ACP scaffold has better support performance than PLLA scaffold [7, 8]. However, it remains to be clarified whether long-term composite scaffold implantation can cause inflammation and calcification of vascular tissues around the scaffold. In this study, PLLA scaffold and biological scaffold synthesized with calcium phosphate were implanted into porcine coronary artery to observe and explore their effects on inflammation and calcification of vessels around the scaffold.

2. Materials and Methods

2.1. Scaffold Preparation. The host material of PLLA/ACP scaffold is the complex consisting of PLLA, and ACP. ACP (Ca/P = 1 : 1, size < 150 nm) was homogeneously mixed with PLLA powder (MW = 250,000 g/mol, Purac Biomaterials, Lincolnshire, IL, USA) with a ratio of PLLA/ACP at 98/2 (*w/w*) using a speed mixer (SpeedMixer™ DAC 600). The mixture was dried at around 60°C overnight prior to extrusion in a single screw extruder (Genca Engineering Inc., Saint Petersburg FL). The extruded tubes were laser-automated according to design specifications (3.0 mm diameter × 13 mm length × 150 μm width), and one radiopaque metal marker was incorporated one on each end. All scaffolds were crimped on 3.0 mm × 15 mm balloon catheters and sterilized with gamma radiation prior to implantation. The PLLA scaffold (3.0 mm diameter × 13 mm length × 150 μm width) was used for the control group; both the production process and the design of PLLA scaffold are as same as the PLLA/ACP scaffold [9].

2.2. Animal Preparation and Scaffold Implantation. Twenty-four minipigs aging 12-20 months and weighing 25-30 kg (no limitation in gender) were used in the experiment. The pigs were fed separately for more than 1 month before the experiment and orally administrated with 300 mg/d aspirin enteric-coated tablets and 75 mg/d clopidogrel hydrogen sulfate tablets 3 days before the experiment. Animal study protocol was approved by Institutional Animal Care Committee at Renmin Hospital of Wuhan University. All procedures involving animal use were conformed to the "Guide for the Care and Use of Laboratory Animals" published by the US National Institutes of Health [10].

Drinking water and food were deprived 12 hours before surgery. Basic anesthesia was performed by intramuscular injection of ketamine hydrochloride, midazolam, and scopolamine. Intraoperative anesthesia was achieved by intravenous anesthesia of ketamine combined with propofol. A 6F sheath was inserted into the femoral artery, the guide wire was pulled out, and 6,000 U heparin was injected. The angiographic catheter was inserted along the guide wire and hooked to the coronary artery, and multiposition angiography was performed. Two straight vascular segments of the left anterior descending branch, the left coronary circumflex branch, and the middle segment of the right coronary artery were randomly selected as the scaffold placement sites. Each pig was implanted with two PLLA/ACP scaffolds or two PLLA scaffolds. Three days after surgery, 1.6 million U penicillin BMP-2ium was intramuscularly injected to prevent infection. Aspirin enteric-coated tablets (100 mg) and clopidogrel hydrogen sulfate tablets (75 mg) were orally administrated continuously until the end point.

2.3. Hematological Examination. By venipuncture, 2 ml blood was collected for hematological examination before and 1, 6, 12, and 24 months after scaffold implantation. Serum levels of C-reactive protein (CRP, mg/l), calcium (Ca, mmol/L), and alkaline phosphatase (ALP, U/L) were measured using an automatic biochemistry analyzer (AU5400, Siemens, Germany) according to the manufacturer's instructions.

2.4. Intravascular Ultrasound. At each time point after angiography, 20 μg nitroglycerin was intracoronarily injected. The intravascular ultrasound (IVUS) catheter was inserted into the distal vessel at least 10 mm away from the scaffold along the guide wire, and then, the IVUS catheter was withdrawn automatically at 0.5 mm/s to record images. Image recording was performed every 2-3 mm to determine the relative position of the IVUS catheter and angiographic images. All IVUS images were recorded and saved for subsequent off-line analysis. Each scaffold segment was divided into three segments in average: proximal, middle, and distal scaffold segment. Single-frame image of each segment was evaluated using vascular calcification score (Table 1). In each segment, the frame with the highest score was selected for calcification scoring, and finally, the average of three segments was used as the calcification score of this scaffold.

2.5. Animal Sampling and Pathological Examination. Three pigs in each group were sacrificed at the 1st, 6th, 12th, and 24th month after scaffold implantation, respectively. The scaffold segment was taken out, and partial tissue around the stented coronary was isolated and put into liquid nitrogen for cryopreservation for next molecular biological detection. The stented coronary sample was fixed with 10% formalin solution and embedded in paraffin.

The scaffold segment specimens were divided into proximal reference vessel, proximal scaffold, middle scaffold, distal scaffold, and distal reference vessel. The hard tissue was sliced using a slicer, and 5 sections were selected from each part for hematoxylin-eosin (HE) staining. Under a light

TABLE 1: Evaluation criteria for peri-strut coronary calcification score.

Degree/extent	<25%	≥25%, <50%	≥50%, <75%	≥75%
a	1	2	3	4
b	2	3	4	4
c	3	4	4	4

The calcification score is evaluated based on the degree and extent of calcification of the vessel wall structure by IVUS. Degree 0 = no calcification was found; a = internal elastic plate calcification of the blood vessel wall; b = calcification involved the medial membrane of the blood vessel; c = calcification involved the external elastic plate of the blood vessel wall. The extent (25%, 50%, 75%) refers to the portion of the circumference of the artery involved.

microscope, four quadrantic visual fields were selected from each section for observation. Under a microscope (magnification, $\times 40$ and $\times 200$), the inflammatory reaction around the scaffold was evaluated using inflammation score (Table 2).

In some sections, NF- κ B was stained with immunohistochemistry to observe the inflammatory reaction, and some were subjected to ALP staining by immunohistochemistry to observe the calcification around the scaffold. Four visual fields were photographed in each section, and the percentage and average optical density of positive cells in the visual fields were randomly measured using the Image-pro Plus 6.0 image analysis system. Finally, positive expression = the percentage of positive cells \times average optical density $\times 100$.

2.6. Molecular Biological Detection. At the same time, the tissue around the scaffold was homogenated and detected by Western blot. The optical intensity of the electrophoretic band of IL-6 and BMP-2 was analyzed by a gel scanner. The expression levels of IL-6 and BMP-2 in muscle tissue were determined by the ratio of the optical intensity of the electrophoretic band of IL-6 and BMP-2 to the optical intensity of the electrophoretic band of β -actin, respectively.

2.7. Statistical Analysis. All results were analyzed by two independent observers. Data were presented as mean value \pm standard deviation (SD). The differences between two groups were compared using independent two-sample *t*-test. The differences between time points were tested for the statistical significance using ANOVA followed by Tukey's test. $P < 0.05$ was considered statistically significant. All statistical analyses were performed with SPSS version 19.0 (Statistical Product and Service Solutions Ltd.).

3. Results

3.1. General Condition. All the 24 pigs survived healthy until the end point of sampling, and no major adverse cardiovascular events such as thrombus and myocardial infarction occurred after scaffold implantation.

No statistically significant differences were found in CRP, Ca, or ALP contents in blood between the two groups before and 1, 6, 12, and 24 months after scaffold implantation ($P > 0.05$, Table 3). The results demonstrated that neither PLLA scaffold nor PLLA/ACP scaffold caused obvious

TABLE 2: Evaluation criteria for peri-strut inflammation score.

Degree/extent	<25%	≥25%, <50%	≥50%, <75%	≥75%
a	1	2	3	4
b	2	3	4	4
c	3	4	4	4

The peri-strut inflammation score is based on the degree of inflammation and extent of the circumference of the artery involved. Degree 0 = not present; a = scattered inflammatory cells; b = small and segmental aggregates of inflammatory cells; c = larger aggregates widespread or circumferentially distributed. The extent (<25%, 25%-50%, and >50%) refers to the portion of the circumference of the artery involved. In general, inflammation scores of 1 and 2 denote excellent local biocompatibility, namely, if neutrophils are not seen. An inflammation score of 3 or 4 may denote a biocompatibility issue, especially if neutrophils or large numbers of lymphocytes are present. Large proportions of eosinophils and lymphocytes may be indicative of a hypersensitivity response.

inflammatory reaction or calcification in the pigs after implantation [11].

3.2. Local Inflammation. In the PLLA group, at the 1st, 6th, 12th, and 24th month after scaffold implantation, HE staining showed that with the extension of implantation time, increasing infiltrated inflammatory cells were found around the PLLA scaffold (Figure 1). Inflammation scores increased gradually after scaffold implantation ($P < 0.05$, Figure 2). The IL-6 expression in the homogenate increased gradually after scaffold implantation ($P < 0.05$, Figure 2), and the IL-6 expression at the 6th, 12th, and 24th months after scaffold implantation was significantly higher than that at the 1st month after implantation ($P < 0.05$, Figure 2). At the 1st, 6th, 12th, and 24th month after scaffold implantation, NF- κ B staining results showed that inflammatory cells were found around the PLLA scaffold (Figure 3).

In the PLLA/ACP group, no significant difference was found in the IL-6 expression among different time points after scaffold implantation ($P > 0.05$, Figure 2). There were a small amount of inflammatory cells around the scaffold at each time point, but the inflammation score, NF- κ B positive index, and IL-6 expression had no significant differences at each time point ($P > 0.05$).

The infiltration of peripheral inflammatory cells in the PLLA group was significantly more obvious than that in the PLLA/ACP group (Figure 1). Inflammation score in the PLLA group was significantly higher than that in the PLLA/ACP group at the 12th and 24th months after scaffold implantation ($P < 0.05$, Table 4). The positive expression of NF- κ B in the tissue and cells around the PLLA scaffold was significantly higher than that in the PLLA/ACP group at the 12th and 24th month after scaffold implantation ($P < 0.05$, Table 4). At the 6th, 12th, and 24th months after scaffold implantation, the IL-6 expression in the PLLA group was significantly higher than that in the PLLA/ACP group ($P < 0.05$, Figure 2).

3.3. Local Calcification. In the PLLA/ACP group, at the 1st, 6th, 12th, and 24th months after scaffold implantation revealed that ALP-rich cells were found around the PLLA scaffold (Figure 4). ALP positive index, BMP-2 expression,

TABLE 3: Serum level of CRP, Ca, and ALP.

	Preimplant	1 month	6 months	12 months	24 months
CRP (mg/l)					
PLLA	4.34 ± 1.39	4.73 ± 1.06	4.93 ± 0.97	5.16 ± 1.02	5.72 ± 1.49
PLLA/ACP	4.49 ± 1.37	4.64 ± 0.71	5.65 ± 0.84	5.24 ± 1.14	5.34 ± 1.14
<i>P</i> values	0.85	0.87	0.20	0.90	0.63
Ca (mmol/L)					
PLLA	1.36 ± 0.37	1.12 ± 0.31	1.16 ± 0.53	1.18 ± 0.35	1.28 ± 0.37
PLLA/ACP	1.36 ± 0.32	1.08 ± 0.26	1.11 ± 0.28	1.14 ± 0.41	1.21 ± 0.60
<i>P</i> values	0.98	0.80	0.85	0.85	0.81
ALP (U/L)					
PLLA	307.15 ± 60.08	307.68 ± 47.98	321.26 ± 59.22	313.33 ± 62.01	351.08 ± 47.21
PLLA/ACP	316.28 ± 54.45	288.93 ± 51.85	334.39 ± 54.07	354.44 ± 52.64	308.42 ± 59.26
<i>P</i> values	0.98	0.80	0.85	0.85	0.81

Data are presented as mean ± standard deviation. *P* values: PLLA/ACP group compared with PLLA group.

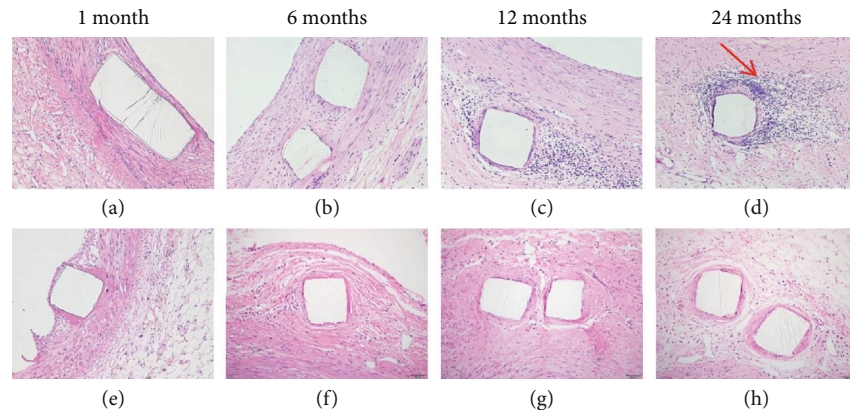


FIGURE 1: Hematoxylin-eosin staining. Histological cross-sections of the stented porcine coronary arteries from 1 month to 24 months ($\times 200$). (a–d) PLLA scaffolds and (e–h) PLLA/ACP scaffolds. Note the remarkable vascular wall swelling, tissue inflammation with PLLA scaffold (red arrows).

and calcification scores increased gradually after scaffold implantation, and ALP positive index, BMP-2 expression, and calcification scores increased gradually after scaffold implantation, and the BMP-2 expression at the 6th, 12th, and 24th month after scaffold implantation was significantly higher than that at the 1st month after scaffold implantation ($P < 0.05$). In the PLLA/ACP group, no significant difference was found in ALP positive index and BMP-2 expression among different time points after scaffold implantation ($P > 0.05$, Figure 2).

The ALP positive expression around the PLLA scaffold was significantly higher than that in the PLLA/ACP group at the 6th, 12th, and 24th month after scaffold implantation ($P < 0.05$, Table 4). At the 12th and 24th month after scaffold implantation, the BMP-2 expression in the PLLA group was significantly higher than that in the PLLA/ACP group ($P < 0.05$, Figure 2). IVUS data showed no significant difference in calcification score between the two groups at the 1st and 6th month after scaffold implantation but higher calcification score in the PLLA group than the PLLA/ACP group at

the 12th and 24th month after scaffold implantation ($P < 0.05$, Table 5).

4. Discussion

Nano-scale ACP is a biodegradable inorganic bioceramic material that has been widely used in biological and medical fields. ACP belongs to calcium phosphate family, which is a natural calcium and phosphate reservoir existed widely in nature. ACP is a calcium phosphate mineral that is nontoxic and harmless to the human body with weak alkaline property, possessing good hydrophilicity, tissue compatibility, and mechanical support as well [12, 13]. The major purpose of the addition of ACP is to increase the mechanical support performance of PLLA scaffold and reduce the thickness of the scaffold. It is expected to reduce the inflammatory reaction caused by acidic products during the degradation of PLLA scaffolds. However, considering ACP as a natural calcium and phosphate reservoir, it requires to be further explored whether long-term implantation of ACP may cause or

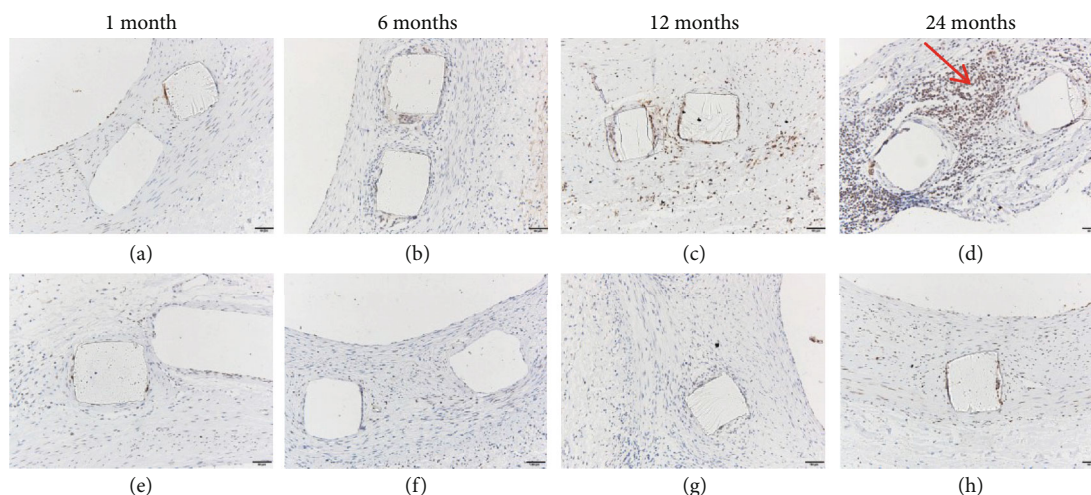


FIGURE 2: Immunohistochemistry staining of NF- κ B, positive cells with the PLLA scaffold (a–d) and with the PLLA/ACP scaffold (e–h). Note the significantly lower expression of NF- κ B in the PLLA/ACP stented artery (e–h) compared with that of the PLLA stented artery (a–d) (the red arrows show positive cells. $\times 200$).

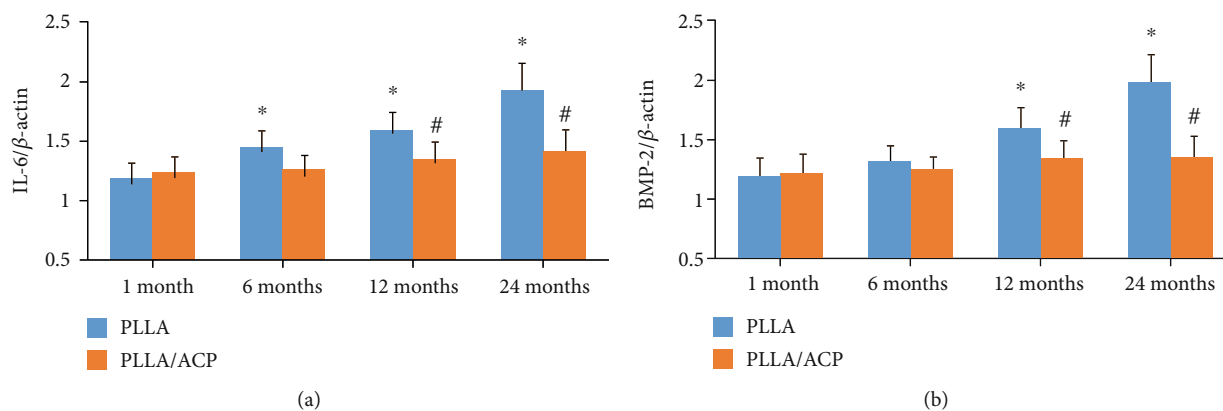


FIGURE 3: Western blotting analysis of coronary arteries treated with PLLA scaffolds and PLLA/ACP scaffolds for 24 months. The expression of IL-6 in the PLLA group was significantly higher than the PLLA/ACP group at 12 months and 24 months (a). The expression of BMP-2 in the PLLA group was significantly higher than the PLLA/ACP group at 6 months, 12 months, and 24 months (b). $P^* < 0.05$ means the PLLA group compared with the PLLA/ACP group. $P\# < 0.05$ means that the data for 6 months, 12 months, and 24 months are compared with the data for 1 month.

promote calcification of tissues around the scaffold, affect the recovery of coronary systolic and diastolic function, even accelerate the formation of new atherosclerotic plaques of the diseased vessel in the scaffolding segment, thus resulting in serious end-stage cardiac events to patients with coronary heart disease. In this study, PLLA and PLLA/ACP scaffolds were implanted into porcine coronary arteries to explore the effect of PLLA/ACP scaffolds on inflammation and calcification of surrounding tissues at 1, 6, 12, and 24 months.

According to the results of this study, there was no significant difference in the content of CRP, calcium, and alkaline phosphatase between groups at 1, 6, 12, and 24 months after scaffold implantation, and there was no significant difference in the results of each group at each time point. It suggested that the two kinds of bioabsorbable scaffolds had no influence in systemic inflammation and calcification of experimental animals. In the aspect of inflammatory response,

with the prolonged duration of scaffold implantation, the scaffold was continuously degraded and absorbed, showing increasingly more infiltration of inflammatory cells around the scaffold in the PLLA group, accompanied by gradual increase in inflammatory score, NF- κ B positive expression index, and IL-6 expression level, which were obviously higher than those in the PLLA/ACP group at 12 and 24 months after implantation. It indicated that the addition of nano-scale ACP can significantly reduce local inflammatory response caused by PLLA scaffold degradation [14].

Furthermore, for calcification reaction, the scaffold was constantly degraded and absorbed with the prolonged duration of scaffold implantation. Besides, there were a growing number of calcification related reactive protein accumulation and potential calcification around PLLA scaffold. Meanwhile, calcification score, ALP positive expression index, and BMP-2 expression level increased gradually in the PLLA group and

TABLE 4: Pathology results.

	1 month	6 months	12 months	24 months
Inflammation scores				
PLLA	0.79 ± 0.41	1.33 ± 0.56	1.63 ± 0.58	1.92 ± 0.58
PLLA/ACP	0.80 ± 0.54	1.04 ± 0.46	1.13 ± 0.34	1.25 ± 0.53
<i>P</i> values	0.75	0.06	<0.01	<0.01
NF-κB positive index				
PLLA	27.97 ± 3.27	36.74 ± 4.24	42.49 ± 4.22	53.75 ± 5.63
PLLA/ACP	28.42 ± 3.81	32.59 ± 3.70	34.21 ± 6.51	37.41 ± 7.24
<i>P</i> values	0.82	0.10	0.03	<0.01
ALP positive index				
PLLA	39.61 ± 8.39	51.45 ± 6.21	61.32 ± 7.43	87.80 ± 9.29
PLLA/ACP	40.07 ± 10.08	43.21 ± 5.86	45.58 ± 6.14	51.71 ± 7.75
<i>P</i> values	0.93	0.04	<0.01	<0.01

Data are presented as mean ± standard deviation. *P* values: PLLA/ACP group compared with PLLA group.

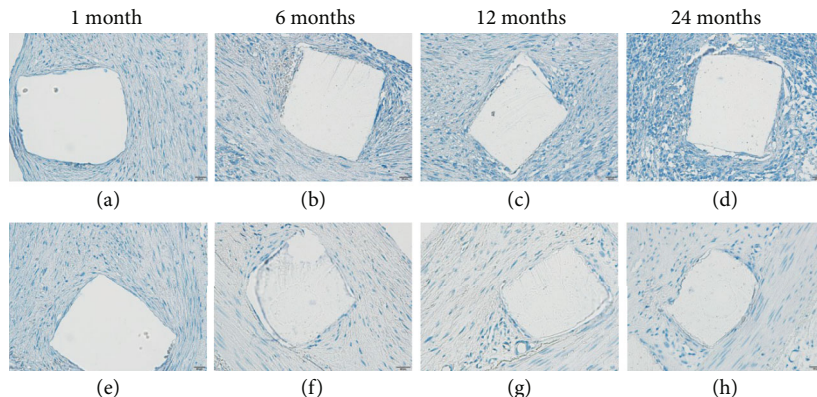


FIGURE 4: Immunohistochemistry staining of ALP, positive cells with the PLLA scaffold (a–d) and with the PLLA/ACP scaffold (e–h). Note the significantly lower expression of MMP-9 in the PLLA/ACP stented artery (e–h) compared with that of the PLLA stented artery (a–d) (×400).

TABLE 5: Calcification scores measured by IVUS.

	1 month	6 months	12 months	24 months
PLLA	0.17 ± 0.38	0.67 ± 0.48	1.21 ± 0.59	1.58 ± 0.50
PLLA/ACP	0.13 ± 0.34	0.50 ± 0.51	0.83 ± 0.48	1.04 ± 0.46
<i>P</i> values	0.69	0.17	0.02	<0.01

Data are presented as mean ± standard deviation. *P* values: PLLA/ACP group compared with PLLA group.

were significantly higher than those in the PLLA/ACP group at 12 and 24 months after implantation. In this regard, the addition of nano-scale ACP can significantly reduce the potential calcification of local tissue caused by PLLA scaffold degradation. One of the important factors of abnormal calcification of the body's soft tissues is the microinflammatory response, in which the chronic microinflammatory response of blood vessels leads to the formation of atherosclerosis. In the late stage of implantation of PLLA scaffold material, the expression levels of calcification-promoting factor alkaline

phosphatase and BMP-2 in the tissue homogenate were higher than those of the PLLA/ACP scaffold material group, which indicates that PLLA scaffold material has certain calcification effect.

One of the important factors of abnormal calcification of soft tissue is the microinflammatory reaction, in which the chronic microinflammatory reaction of blood vessels leads to the formation of atherosclerosis that can also promote the abnormal calcification of soft tissue [15, 16]. The process of calcification promoted by microinflammatory reaction can be divided into three stages. To be specific, in the initial stage, inflammatory factors released by microinflammatory reaction and infiltrated monocyte/macrophage promote the formation of calcification factors in tissues. In the middle stage, the combination of microinflammatory response and calcification-promoting factor can transform histocytes into osteoblasts, secrete and release matrix vesicles, promote cell apoptosis, and release apoptotic bodies [17, 18]. In the case of high concentration of calcium and phosphorus, matrix vesicles and apoptotic bodies promote the formation of

hydroxyapatite and provide new focal points for its nucleation, thus forming microcalcification. In the later stage, the microinflammatory reaction further upregulates calcification-promoting factor, downregulates calcification-inhibiting factor, and promotes mineralization of stromal vesicles, resulting in the development of obvious tissue calcification from microcalcification [19].

With the addition of a small amount of ACP, it can be transformed into essential elements such as Ca and P through normal metabolism of human body and can bond with human tissue to form hydroxyl (-OH) group, generate a natural weak alkaline environment, neutralize acidic metabolites of PLLA, facilitate cell adhesion and growth, and thus reduce the occurrence of scaffold thrombosis and restenosis. In the process of alleviating inflammatory reaction, ACP also inhibits the potential effect of promoting calcification of PLLA degradable scaffolds. In view of the possible mechanisms, firstly, the local tissue develops acidic microinflammatory reaction that promotes calcification subsequently during the decomposition of PLLA, while the addition of weakly basic ACP material neutralizes acidic microinflammatory reaction of PLLA, thus reducing calcification. Secondly, ACP has a strong hydrophilicity [20, 21], which is conducive to the growth of cells, reducing cell apoptosis, thus decreasing the site of hydroxyapatite nucleation. Thirdly, the ratio of calcium to phosphorus in ACP is 1:1, with less content of calcium in ACP compared with other calcium phosphates with high ratio of calcium to phosphorus. Meanwhile, PLLA and ACP are mixed in the ratio of 98:2, forming a new bioabsorbable PLLA/ACP material that has less content of calcium and phosphorus, which can reduce the risk of calcification in the absence of high concentration of calcium and phosphorus.

5. Conclusions

To sum up, the novel bioabsorbable PLLA/ACP scaffolds have good histocompatibility and mild inflammatory response. In our study, the incorporation of small-dose ACP can reduce the acidic inflammatory response of PLLA scaffolds, which can not only maintain the formation of calcification in surrounding tissues but also inhibit tissue calcification by reducing the content of calcification-promoting factors in vivo.

5.1. Limitations and Future Studies. First, the coronary arteries of the experimental minipigs did not have atherosclerosis, and the inflammatory and calcification responses during vascular repair may be different from humans. Second, a relatively small sample size may affect the results of statistical analysis. We will carry out related research on the changes of ACP and PLLA materials on the biochemical environment around tissues. Our next step is to further extend to the atherosclerosis model and to detect and evaluate the effects of PLLA/ACP bioabsorbable scaffolds on the inflammation and calcification of surrounding tissues in the coronary intimal injury model.

Data Availability

All results were analyzed by two independent observers. Data were presented as mean value \pm standard deviation (SD). The differences between two groups were compared using independent two-sample *t*-test. The differences between time points were tested for the statistical significance using ANOVA followed by Tukey's test. $P < 0.05$ was considered statistically significant. All statistical analyses were performed with SPSS version 19.0 (Statistical Product and Service Solutions Ltd.).

Conflicts of Interest

The authors declare that they have no conflicts of interest.

Acknowledgments

The study was supported by grants from the Wuhan Youth Science and Technology Chenguang Plan (2017050304010280), the NSFC Guidance fund project of the Renmin Hospital of Wuhan University (RMYD2018M24), and the Natural Science Foundation of Hubei Province (2020CFB238).

References

- [1] Y. Sekimoto, H. Obara, K. Matsubara, N. Fujimura, H. Harada, and Y. Kitagawa, "Comparison of early vascular morphological changes between bioresorbable poly-L-lactic acid scaffolds and metallic stents in porcine iliac arteries," *Organogenesis*, vol. 13, no. 2, pp. 29–38, 2017.
- [2] Z. Lan, Y. Lyu, J. Xiao et al., "Novel biodegradable drug-eluting stent composed of poly-L-lactic acid and amorphous calcium phosphate nanoparticles demonstrates improved structural and functional performance for coronary artery disease," *Journal of Biomedical Nanotechnology*, vol. 10, no. 7, pp. 1194–1204, 2014.
- [3] S. Bangalore, H. G. Bezerra, D. G. Rizik et al., "The state of the absorb bioresorbable scaffold: consensus from an expert panel," *JACC: Cardiovascular Interventions*, vol. 10, no. 23, pp. 2349–2359, 2017.
- [4] D. Mahtta and I. Y. Elgendy, "Everolimus-eluting bioresorbable vascular scaffolds: learning from the past to improve the future," *Minerva Cardioangiologica*, vol. 67, no. 4, pp. 288–305, 2019.
- [5] D. R. Bienek and D. Skrtic, "Utility of amorphous calcium phosphate-based scaffolds in dental/biomedical applications," *Biointerface research in applied chemistry*, vol. 7, no. 1, pp. 1989–1994, 2017.
- [6] Q. W. Fu, Y. P. Zi, W. Xu et al., "Electrospinning of calcium phosphate-poly (d,l-lactic acid) nanofibers for sustained release of water-soluble drug and fast mineralization," *International Journal of Nanomedicine*, vol. Volume 11, pp. 5087–5097, 2016.
- [7] T. Dinh Nguyen, G. Feng, X. Yi et al., "Six-month evaluation of novel bioabsorbable scaffolds composed of poly-L-lactic acid and amorphous calcium phosphate nanoparticles in porcine coronary arteries," *Journal of Biomaterials Applications*, vol. 33, no. 2, pp. 227–233, 2018.
- [8] G. Feng, J. Xiao, Y. Bi et al., "12-month coronary angiography, intravascular ultrasound and histology evaluation of a novel

- fully bioabsorbable poly-L-lactic acid/amorphous calcium phosphate scaffolds in porcine coronary arteries,” *Journal of Biomedical Nanotechnology*, vol. 12, no. 4, pp. 743–752, 2016.
- [9] D. Gu, G. Feng, G. Kang et al., “Improved biocompatibility of novel biodegradable scaffold composed of poly-L-lactic acid and amorphous calcium phosphate nanoparticles in porcine coronary artery,” *Journal of Nanomaterials*, vol. 2016, 8 pages, 2016.
- [10] National Research Council (US) Committee for the Update of the Guide for the Care and Use of Laboratory Animals, *Guide for the Care and Use of Laboratory Animals*, National Academies Press (US), Washington (DC), 8th edition, 2011.
- [11] H. Li, K. Sun, R. Zhao et al., “Inflammatory biomarkers of coronary heart disease,” *Frontiers in Bioscience*, vol. 10, no. 1, pp. 185–196, 2018.
- [12] J. N. O’Donnell, J. M. Antonucci, and D. Skrtic, “Amorphous calcium phosphate composites with improved mechanical properties,” *Journal of Bioactive and Compatible Polymers*, vol. 21, no. 3, pp. 169–184, 2016.
- [13] G. Feng, T. Dinh Nguyen, X. Yi et al., “Evaluation of long-term inflammatory responses after implantation of a novel fully bioabsorbable scaffold composed of poly-L-lactic acid and amorphous calcium phosphate nanoparticles,” *Journal of Nanomaterials*, vol. 2018, 9 pages, 2018.
- [14] J. D. Beck, K. L. Moss, T. Morelli, and S. Offenbacher, “Periodontal profile class is associated with prevalent diabetes, coronary heart disease, stroke, and systemic markers of C-reactive protein and interleukin-6,” *Journal of Periodontology*, vol. 89, no. 2, pp. 157–165, 2018.
- [15] L. Chen, H. Deng, H. Cui et al., “Inflammatory responses and inflammation-associated diseases in organs,” *Oncotarget*, vol. 9, no. 6, pp. 7204–7218, 2017.
- [16] M. Alique, R. Ramírez-Carracedo, G. Bodega, J. Carracedo, and R. Ramírez, “Senescent microvesicles: a novel advance in molecular mechanisms of atherosclerotic calcification,” *International Journal of Molecular Sciences*, vol. 19, no. 7, p. 2003, 2018.
- [17] K. Benz, K. F. Hilgers, C. Daniel, and K. Amann, “Vascular calcification in chronic kidney disease: the role of inflammation,” *International Journal of Nephrology*, vol. 2018, 4310377 pages, 2018.
- [18] P. S. Gade, R. Tulamo, K. W. Lee et al., “Calcification in human intracranial aneurysms is highly prevalent and displays both atherosclerotic and nonatherosclerotic types,” *Arteriosclerosis, Thrombosis, and Vascular Biology*, vol. 39, no. 10, pp. 2157–2167, 2019.
- [19] A. Sakamoto, R. Virmani, and A. V. Finn, “Coronary artery calcification: recent developments in our understanding of its pathologic and clinical significance,” *Current Opinion in Cardiology*, vol. 33, no. 6, pp. 645–652, 2018.
- [20] J. N. O’Donnell, G. E. Schumacher, J. M. Antonucci, and D. Skrtic, “Structure-composition-property relationships in polymeric amorphous calcium phosphate-based dental composites,” *Materials (Basel)*, vol. 2, no. 4, pp. 1929–1954, 2009.
- [21] S. Allegrini Jr., A. C. da Silva, M. Tsujita, M. B. Salles, S. A. Gehrke, and F. J. C. Braga, “Amorphous calcium phosphate (ACP) in tissue repair process,” *Microscopy Research and Technique*, vol. 81, no. 6, pp. 579–589, 2018.

Research Article

In Vivo Evaluation of the Antitumor and Immunogenic Properties of Silver and Sodium Dichloroacetate Combination against Melanoma

Zaida Torres-Cavazos,¹ Moisés Armides Franco-Molina ,²
Silvia Elena Santana-Krímskaya,² Cristina Rodríguez-Padilla,² Jorge Ramsy Kawas-Garza,¹
Gustavo Hernández-Vidal,¹ Gustavo Moreno-Degollado,¹ and Diana Elisa Zamora-Ávila¹

¹Posgrado Conjunto de las Facultades de Agronomía y Medicina Veterinaria y Zootecnia, Universidad Autónoma de Nuevo León, Ave. Universidad S/N, Cd. Universitaria, San Nicolás de los Garza, N. L., CP 66455, Mexico

²Laboratorio de Inmunología y Virología, Unidad C, Facultad de Ciencias Biológicas, Universidad Autónoma de Nuevo León, Ave. Universidad S/N, Cd. Universitaria, San Nicolás de los Garza, N. L., CP 66455, Mexico

Correspondence should be addressed to Moisés Armides Franco-Molina; moyfranco@gmail.com

Received 13 July 2020; Revised 28 September 2020; Accepted 14 October 2020; Published 7 November 2020

Academic Editor: Yanis Toledano Magaña

Copyright © 2020 Zaida Torres-Cavazos et al. This is an open access article distributed under the Creative Commons Attribution License, which permits unrestricted use, distribution, and reproduction in any medium, provided the original work is properly cited.

Our main focus was to evaluate the efficacy of silver and sodium dichloroacetate as dual-function agents to be used in melanoma treatment. This strategy is designed to increase the activity of these two compounds that affect DNA integrity and the mitochondria at different levels. Furthermore, we evaluated if the cell death mechanism induced by our treatments was immunogenic cell death. To evaluate antitumor efficacy, we assessed tumor volume and production of tumor necrosis factor- α , nuclear factor κ B (both by ELISA), and nitric oxide levels (Nitrate/Nitrite colorimetric assay kit); for immunogenic cell death, we evaluated the release of danger-associated molecular patterns using immunohistochemistry and flow cytometry, as well as an *in vivo* challenge. Our results showed that the combination of colloidal silver and sodium dichloroacetate is more effective than each treatment alone and that the antitumor mechanism is not through immunogenic cell death. Furthermore, this study can broadly contribute to the development of dichloroacetate-loaded silver nanoparticles and to the design targeted pharmacological formulations to fight melanoma as well as other types of cancer.

1. Introduction

Targeted therapies have increased the chances of survival for people with melanoma [1]; however, cancer cells present within the tumor favor different metabolic pathways [2]; as a consequence, the tumor eventually becomes resistant to targeted therapies, especially the ones designed against a single target [3].

The development of silver-based therapies is a promising tool in cancer treatment. Silver ions and silver nanoparticles induce oxidative stress, mitochondrial membrane dysfunction, DNA damage, and cytokines upregulation [4]. The exact action mechanism varies depending on the physical and chemical properties of the nanoparticle and the type of

cancer [5]. Furthermore, the clinical use of colloidal silver for bactericidal and antiviral purposes proves that this treatment is safe [6, 7].

Sodium dichloroacetate (DCA) is a pyruvate analog which interferes with tumor-associated glycolysis (Warburg effect), decreases cancer malignancy, and reduces lactate production by altering cancer cell metabolic pathways [8]. A decrease in lactate counteracts the acidic state of tumoral microenvironment, reducing tumor growth and metastasis [8]. WZB117, a bis-hydroxybenzoate, 2-deoxy-d-glucose, metformin, and DCA reduce glycolysis and block glucose uptake in cancer cells. Under low intracellular glucose levels, biosynthetic pathways, such as nucleotides and amino acids genesis, are interrupted due to a shortage of intermediate

molecules, putting a break on cell proliferation. Despite of its use as monotherapy or combined with chemotherapy, few or none adverse effects have been reported [9].

Because of these activities, we evaluated immunogenic cell death as a possible action mechanism, owing to the increasing number of studies that demonstrate that cellular and mitochondrial danger-associated molecular patterns (DAMPs) can be actively released when exposed to external stimuli [10]. The release of alarmins (Hsp70, HSP90, calreticulin, HMGB1, ATP, DNA, and RNA) and tumor neoantigens induce a tumor-specific immune response that eliminates live cancer cells and residual tumor tissue, avoiding cancer recurrence [11].

The main focus of this study was to use silver and DCA as dual-function agents that affect the DNA integrity and mitochondria activity in order to increase the antitumor response in melanoma treatment. Furthermore, this study could serve as a starting point for the next level developmental stage of dichloroacetate-loaded silver nanoparticles targeted pharmaceutical formulation.

2. Materials and Methods

2.1. Reagents. Penicillin-streptomycin solution, Ficoll-Hypaque solution, trypsin-EDTA solution, RPMI-1640 medium, Dulbecco's Modified Eagle's Medium (DMEM/F-12), and 1% antibiotic-antimycotic solution were obtained from Life Technologies GIBCO, Grand Island, NY, USA. Fetal bovine serum (FBS) was purchased from Sigma-Aldrich (St. Louis, MO).

2.2. Cell Culture. B16F10 murine melanoma cell line was purchased from American Type Culture Collection (ATCC, Manassas, VA, USA). Cells were grown and maintained in Dulbecco's Modified Eagle's Medium supplemented with 10% fetal bovine serum (FBS) and 1% penicillin-streptomycin solution at 37°C and 5% CO₂ atmosphere.

2.3. Cell Viability. Cells (5×10^3 cells/well) were plated on 96 flat-bottom well plates and incubated for 24 h at 37°C in 5% CO₂ atmosphere. After incubation, culture medium was removed, and Ag (0.8mM to 6.5×10^{-5} mM) or DCA (75mM/ml to 750mM/ml) diluted in the same medium were added. The plates were then incubated for 4h at 37°C and 5% CO₂ atmosphere. Thereafter, the supernatant was removed, and cells were washed twice with DMEM/F-12 medium. Cell viability was determined by the resazurin (Alamar Blue) method, and cytotoxicity was expressed as the concentration of 50% cell growth inhibition (LD₅₀). Results were given as the mean \pm standard deviation (SD) of three independent experiments. The LD₅₀ of each treatment was used in further experiments.

2.4. Cell Death Determination. For cell death determination, we followed the methodology described by Rodríguez-Salazar et al. [12]. Briefly, B16F10 cells (1×10^5) were seeded into 12-well plates and cultured overnight in 5% CO₂ at 37°C. Cells were treated with AgC (LD₅₀) or DCA (LD₅₀) or a combination of AgC (LD₂₅) + DCA (LD₂₅) for 5h. Following treatment, cells were collected and

washed with phosphate-buffered saline (PBS) and resuspended in 100 μ l of 1 \times binding buffer (0.1M Hepes pH 7.4, 1.4M NaCl, and 25 mM CaCl₂; Sigma-Aldrich; Merck KGaA, Darmstadt, Germany) supplemented with APC-conjugated Annexin V (5 μ l/sample) and propidium iodide (1 μ l/sample), incubated on at 4°C, and kept in the dark for 15 min. Flow cytometry analysis was performed using an Accuri C6 cytometer; the BD Accuri C6 Software version 1.0.264.21 was used for data analysis (both BD Biosciences, San Jose, CA, USA).

2.5. Animals. Female C57BL/6 mice aged 6 and 10 weeks with a body weight around 23 (± 2) g were purchased from the Harlan Laboratories (Mexico City, Mexico). The mice were kept at 25–29°C and a 12h light to 12h dark cycle. Food and water were provided *ad libitum*. The experimental protocol was approved by the Ethics Review Committee for Animal Experimentation of the Biological Sciences Faculty, Autonomous University of Nuevo Leon (San Nicolas de los Garza, Mexico).

2.6. Tumor Implantation and Treatment Administration. Tumors were induced subcutaneously by injecting 1×10^6 B16F10 cells in 200 μ l of phosphate buffered saline (PBS) solution. Seven days after B16F10 cell transplantation, a noticeable tumor mass appeared, and mice were distributed randomly into four groups (five mice per group). The control group received only saline solution. The DCA group received 50mg/kg of DCA, whereas the Ag group received 28mg/kg of Ag. Saline solution, Ag, and DCA were administrated by peritumor route, daily, for 21 days. Finally, the Ag + DCA group received the same of doses Ag and DCA by peritumor route every other day, alternating between treatments. Tumor length and width were measured weekly, and tumor volume was determined using the equation: $L \times W^2$, where L is the longest side and W is the shortest side. Animals were euthanized at the study endpoint (21 days), and the tumors were excised for further experiments.

2.7. ELISA for Active NF- κ B p65 Subunit. To measure NF- κ B p65 subunit activation, nuclear extracts were prepared from 3×10^6 tumor cells, using a Nuclear Extract Kit according to the manufacturer's protocol. Levels of nuclear p65 concentrations were determined by a sensitive ELISA assay (TRANS-AM, Active Motif, Rixensart, Belgium).

2.8. TNF- α and NO Production. Tumors were macerated with RPMI and the supernatant collected and adjusted at a concentration of protein by BSA and stored at -20°C for evaluation. TNF- α was measured in the tumor supernatant by enzyme-linked immunosorbent assays (TNF alpha Mouse ELISA Kit; Invitrogen; Thermo Fisher Scientific; Viena, Austria). All assay procedures were performed according to the manufacturer's protocol.

Nitrate/Nitrite assay kit was used to measure the levels of NO in the tissue homogenates of the tumor followed the protocol established by the manufacturer (Nitrate/Nitrite colorimetric assay kit; Cayman Chemical, USA).

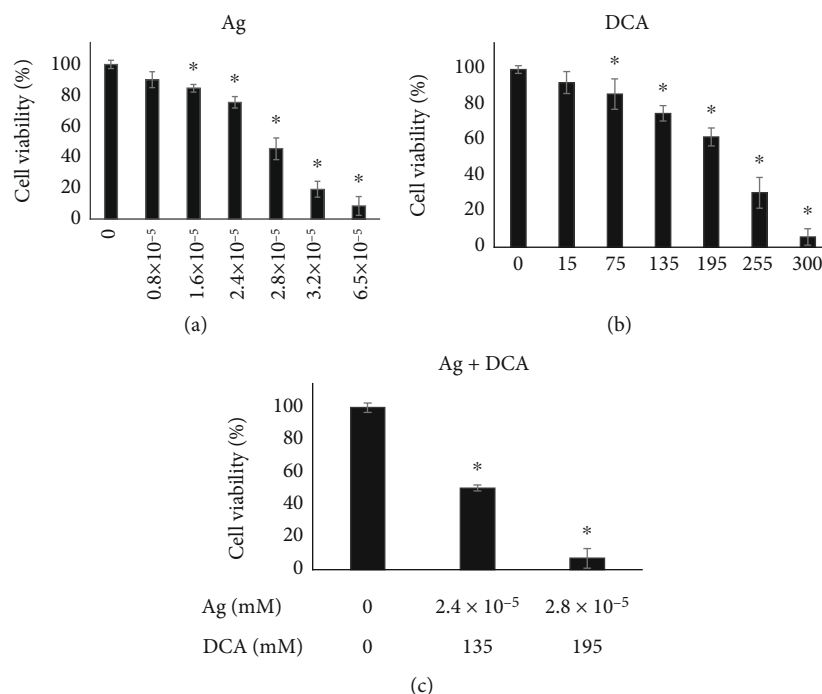


FIGURE 1: Cell viability of B16F10 cells. B16F10 cells were cultured in 96-well plates (5×10^3 cells/well) at 37°C and 5% CO_2 for 24 hours. Then, cells were treated with Ag ($0 - 6.5 \times 10^{-5}$ mM), DCA (0-300 mM), or Ag + DCA ($0 - 2.8 \times 10^{-5}$ mM and 0-195 mM, respectively) for 4 hours. Cell viability was determined with the resazurin assay; briefly, treatments were removed, and cells were incubated with the resazurin reagent (20% v/v) for 1 hour; past this time, fluorescence of converted resorufin was determined at 530nm excitation wavelength and 590 emission wavelength. Increased fluorescent signal was quantified as cell viability. Graph bars show the mean of three independent experiments \pm standard deviation. Statistical difference ($p \leq 0.05$) was determined with the Dunnett post hoc test. There is statistical difference between the control and labelled bars in the graph (*).

2.9. Immunocytochemistry for HMGB1, HSP70, and HSP90 Determination. Cells (100×10^3 cells/well) were seeded on glass cover slips at 37°C and 5% CO_2 for 24 hours. After this, cells were treated with Ag LD_{50} (2.8×10^{-5} mM), DCA LD_{50} (195 mM), or Ag + DCA LD_{50} (2.8×10^{-5} mM and 135 mM, respectively) at 37°C and 5% CO_2 for 4 hours. Subsequently, cells were fixed with methanol, blocked with normal horse serum (2.5%) (Vector Laboratories, ABC Kit) for 20 minutes, and incubated for 4 hours with Santa Cruz (Santa Cruz, CA, USA) mouse monoclonal antibodies against HMGB1 (sc-56698), HSP70 (sc-24), or HSP90 (sc-7947), all used in a 1:1000 dilution. Then, cells were incubated with HRP-biotinylated anti-mouse/rabbit IgG (Vector Laboratories, ABC Kit) for 1 hour and Avidin-DH solution (Vector Laboratories, ABC Kit) for 30 minutes; DAB (3,3'-diaminobenzidine) was added afterwards. DAB chromogen produces a brown reaction in the presence of peroxidase (HRP). Slides were counterstained with Mayer's hematoxylin, dehydrated in an alcohol-xylol gradient, and mounted with Entellan® (synthetic resin) onto glass slides. Untreated B16F10 cells were used as HMGB1, HSP70, and HSP90 basal expression control. The HMGB1, HSP70, and HSP90 expression (DAB staining intensity) was performed using the Fiji (ImageJ) software version 2.0 as described by Patera (2019). Data are presented as DAB optical density ($=\log(\text{max intensity}/\text{mean intensity})$) of five sections per slide. Three independent experiments were performed.

2.10. Flow Cytometry for Calreticulin Determination. Cells (50×10^3 cells/well) were seeded on ultra-low-attachment, 24-well plates at 37°C and 5% CO_2 . After this, cells were treated with Ag LD_{50} (2.8×10^{-5} mM), DCA LD_{50} (195 mM), or Ag + DCA LD_{50} (2.4×10^{-5} mM and 135 mM, respectively) at 37°C and 5% CO_2 for 4 hours. Subsequently, cells were recovered and stained with calreticulin polyclonal antibody conjugated with phycoerythrin for 1 hour at 37°C and 5% CO_2 . Cells were washed with PBS+bovine serum albumin (BSA) (1% w/v) and resuspended in $200\mu\text{l}$ of PBS. Events were acquired in the Accouri C6 flow cytometer (BD Biosciences, San Jose, CA, USA).

2.11. In Vivo Antitumor Vaccination Experiments. For cell lysate preparation, we followed the protocol described by Rodríguez-Salazar et al. [12] with minor modifications. Briefly, B16F10 cells (5×10^6) were treated *in vitro* with Ag (LD_{50}) or DCA (LD_{50}) or the Ag (LD_{25}) + DCA (LD_{25}) combination for 5h. Following this, the cells were centrifuged at $260 \times g$ for 10min and washed twice with PBS. Finally, cells were resuspended in $200\mu\text{l}$ PBS and inoculated subcutaneously into the left flank of the mouse. After 7 days, mice were challenged with 5×10^5 live B16F10 cells resuspended in $200\mu\text{l}$ of PBS via subcutaneous injection into the right flank. Tumor incidence and growth were measured every day at the two injection sites for 30 days with a digital caliper. Tumor volume was calculated using the formula: $V = (L \times W^2)/2$,

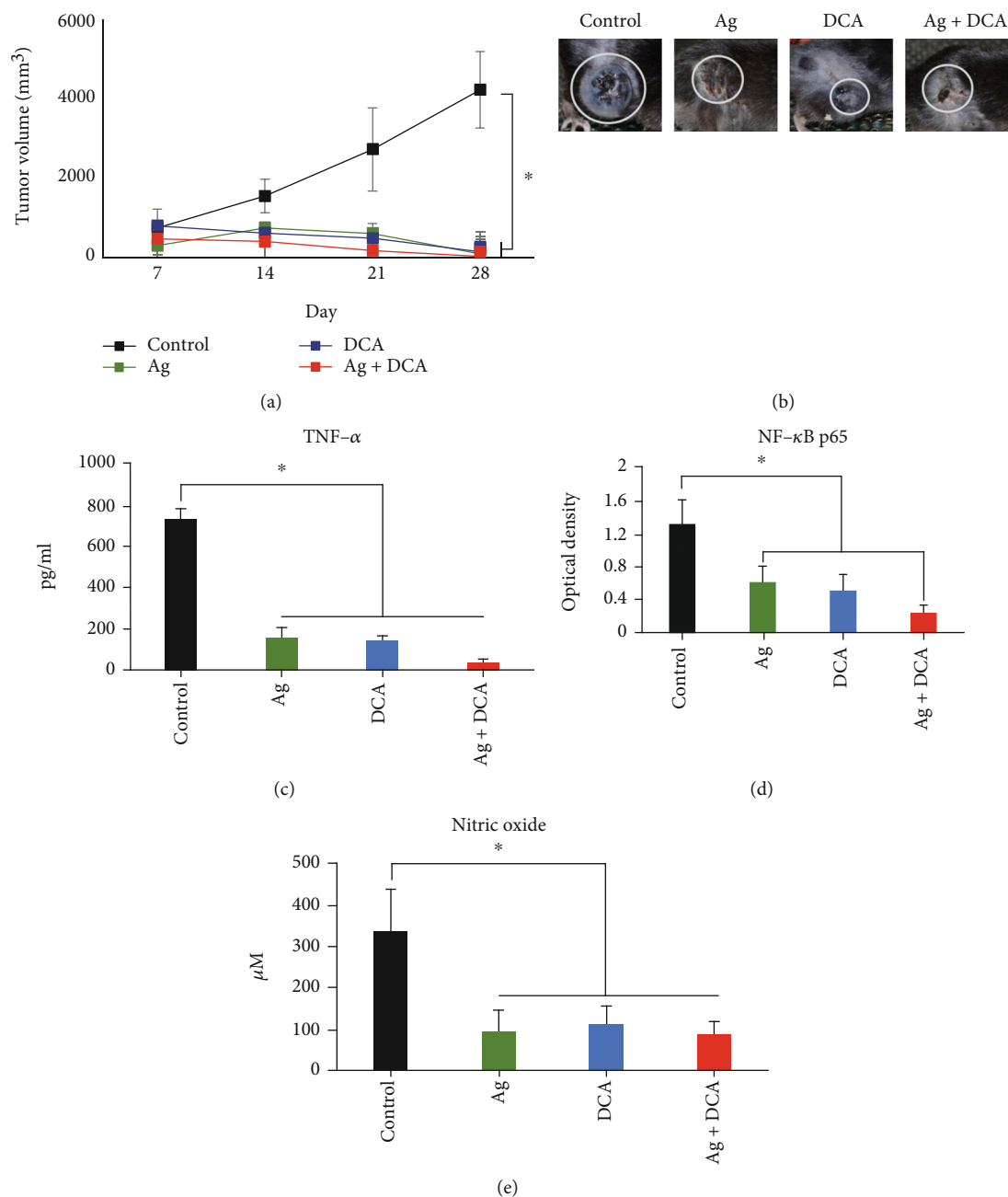


FIGURE 2: Tumor regression in melanoma tumor-bearing mice treated with Ag + DCA. B16F10 viable cells (0.5×10^6) were injected into the left flank of C57BL/6 mice. Mice were randomly distributed into 4 experimental groups: untreated (control) or treated with Ag (28mg/kg), DCA (500mg/kg), or Ag (28mg/kg) + DCA (500mg/kg). Tumor growth was monitored daily until mice sacrifice and determined with the equation: tumor volume = $(L \times W^2)/2$, where L is the longest side and W is the shortest side (a). Representative photographs of tumors or remaining lesions from mice of each group are shown (b). Graph bar represents the mean \pm standard deviation of TNF- α (c), NF- κ B p65 (d), and nitric oxide (e) levels of three mice per group. There is statistical difference ($p \leq 0.05$) between bars labelled with (*).

where V is the tumor volume, L is the tumor length, and W is the tumor width, same formula as previously used by Rodríguez-Salazar et al. [12].

2.12. *Statistical Analysis.* Statistical analysis was performed using a one-way analysis of variance (ANOVA) followed by Dunnett's test, unless otherwise stated. Statistically significant difference was considered at $p < 0.05$. All experiments were performed in triplicate.

3. Results

3.1. *DCA-Ag Decreased the Cellular Viability of Melanoma B16F10 Cells.* The treatment of Ag or DCA induced a cell viability decrease of B16F10 cells in a dose-dependent manner when compared with the control ($p < 0.01$) (Figures 1(a) and 1(b)). DL_{25} (2.4×10^5 mM) and DL_{50} (2.8×10^5) were determined for Ag (Figure 1(a)); DL_{25} (135mM) and DL_{50} (195 mM) were also determined for DCA (Figure 1(b)).

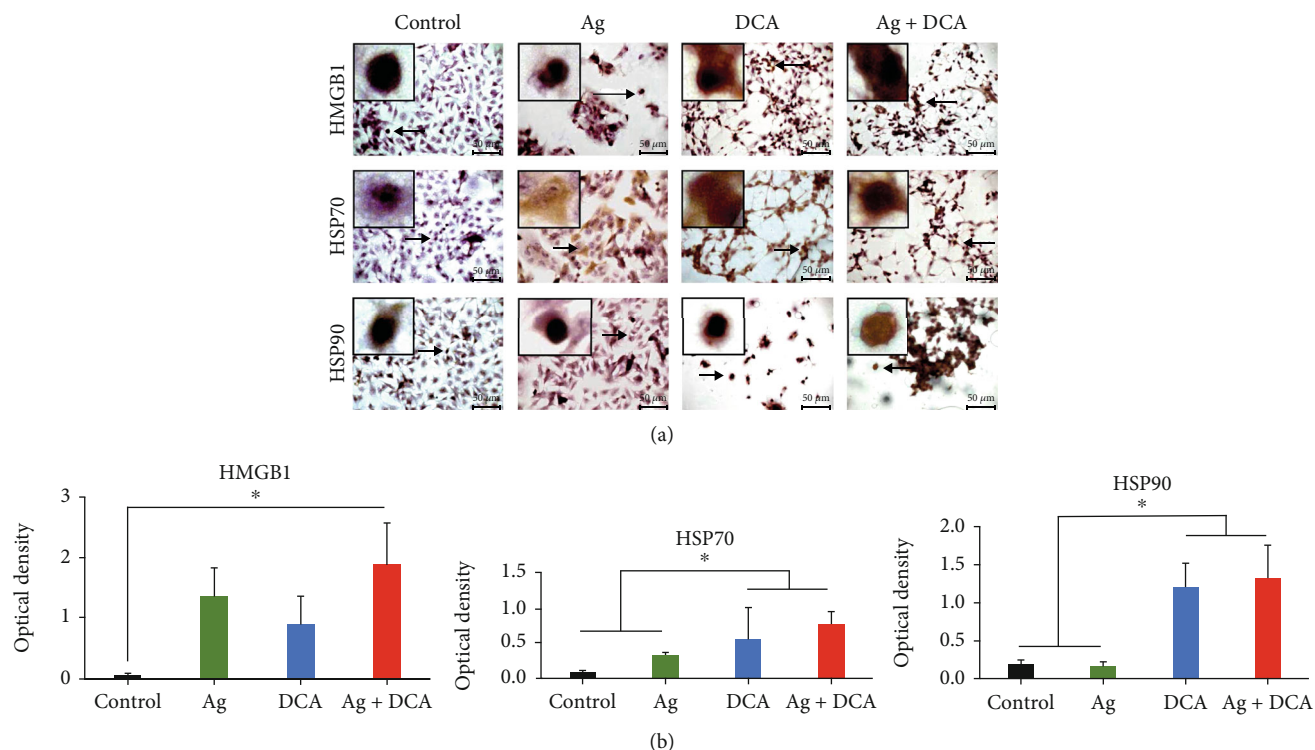


FIGURE 3: Immunocytochemistry of B16F10 cells. B16F10 cells were cultured in 6-well plates (100×10^3 cells/well) on glass cover slips at 37°C and 5% CO_2 for 24 hours. Then, cells were treated with Ag (2.8×10^{-5} mM), DCA (195 mM), or Ag + DCA (2.4×10^{-5} mM and 135 mM, respectively) for 4 hours and fixed with 100% methanol. Primary antibodies for HMGB1, HSP70, and HSP90 were applied, followed by HRP secondary antibody and ABC substrate kit (Vector Laboratories, Burlingame, CA). The cells were counterstained with hematoxylin (Vector), mounted onto slides, and imaged at 40x. Positive protein expression is evidenced by the presence of brown stain in the cell nucleus, cytoplasm, or both and quantified with the image analyzer software Fiji (ImageJ) version 2.0. Representative images of three independent experiments are shown (a). There is no statistical difference ($p \leq 0.05$) between bars labelled with the (*) in the graph (b).

Lower doses of Ag and DCA were required in the combinational setting to achieve DL_{25} and DL_{50} (Figure 1(c)).

3.2. Ag-DCA Induced Tumor Regression. The administration of Ag, DCA, and Ag + DCA induced tumor volume regression ($p < 0.05$) in a time-dependent manner, observing a better effect in mice treated with Ag + DCA treatment (Figure 2(a)).

3.3. Ag, DCA, and Ag + DCA Treatments Decreased $\text{TNF-}\alpha$, $\text{NF-}\kappa\text{B}$, and Nitric Oxide. All treatments significantly decreased ($p < 0.05$) $\text{TNF-}\alpha$ production (Figure 2(c)), $\text{NF-}\kappa\text{B}$ activity (Figure 2(d)), and nitric oxide (NO) production when compared to the control group; significant difference was not observed between treated groups (Figures 2(c)–2(e)).

3.4. HMGB1, HSP70, and HSP90 Expression and Localization in B16F10 Cells Treated with Ag, DCA, or Ag + DCA. HMGB1, HSP70, and HSP90 localization were determined by microscopy (Figure 3(a)). In control conditions, HMGB1, HSP70, and HSP90 were undetectable or localized to the nucleus (Figure 3(a)). Ag treatment mobilized HSP70 to the cytoplasm and cell membrane, DCA treatment mobilized HMGB1 and HSP70 to the cytoplasm and cell membrane, and AgDCA combined treatment mobilized HMGB1,

HSP70, and HSP90 to the cytoplasm and cell membrane (Figure 3(a)).

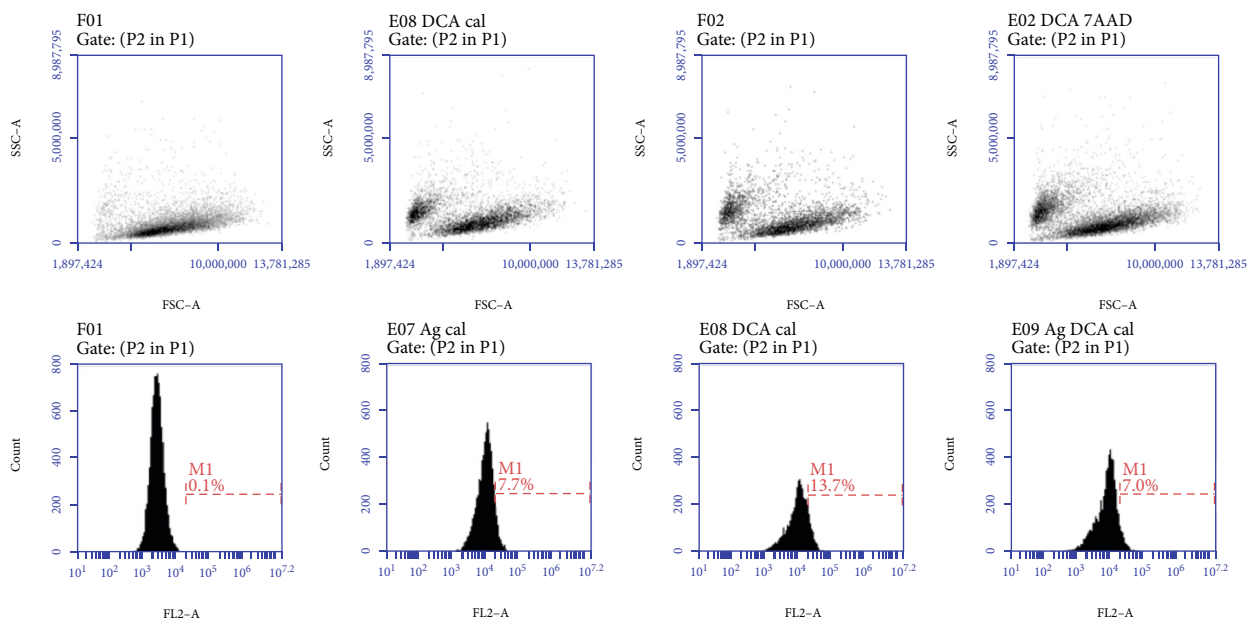
All treatments significantly increased ($p < 0.05$) HMGB1 and HSP70 expression; however, only DCA and Ag + DCA significantly increased ($p < 0.05$) HSP90, as compared to the control (untreated B16F10 cells) (Figure 3(b)).

3.5. Calreticulin Exposure in Ag, DCA, or Ag + DCA Treated Cells. Ag, DCA, and Ag + DCA treatments do not induce calreticulin surface exposure in B16F10 cells, as compared to the control (B16F10 untreated cells) (Figures 4(a) and 4(b)).

3.6. Ag, DCA, or Ag + DCA Do Not Induce Immunogenic Cell Death. B16F10 cells lysed with Ag, DCA, and AgDCA do not prevent tumor implantation in C57BL/6 mice (Figures 5(a)–5(d)).

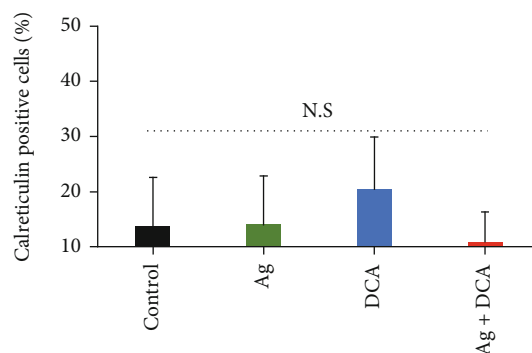
4. Discussion

The cytotoxic effect of colloidal silver (Ag), sodium dichloroacetate (DCA), and their combination was evaluated against B16F10 murine melanoma cells. Our results show that Ag has antiproliferative effects against B16F10 cells, as previously reported by our research group [13]. Further reports of the cytotoxic activity of silver against melanoma cells refer to silver nanoparticles, although the proposed toxicity



(a)

Calreticulin



(b)

FIGURE 4: Calreticulin surface exposure in B16F10 cells. B16F10 cells were cultured in 24-well plates (50×10^3 cells/well) at 37°C and $5\% \text{CO}_2$ for 24 hours. Then, cells were treated with Ag (2.8×10^{-5} mM), DCA (19mM), or Ag + DCA (2.4×10^{-5} mM and 135mM, respectively) for 4 hours. Calreticulin exposure was determined by flow cytometry. The figure shows (a) size versus granularity representative dot plots of the analyzed cell population (above) and cell count versus stain intensity representative histograms. (b) Positive stain average cell percentage \pm standard deviation of three independent experiments. There is no statistical difference ($p \leq 0.05$) between bars as determined by one-way ANOVA and the Tukey post hoc test.

mechanism remains the same [14]. DCA also exhibited an antiproliferative effect against melanoma cells. In a similar manner, Rivera-Lazarín et al. reported a dose-dependent viability decrease in B16F10 cells treated with DCA [15].

The cytotoxic activity of Ag and DCA increased when used as a combined treatment. This was expected since the combination of two or more agents is a cornerstone for cancer treatment; it allows to target key pathways simultaneously, achieving an efficacy increase [16].

After observing the increased cytotoxic effect, we evaluated whether our results correlated with an *in vivo* antitumor activity. At the tumor level, the generation of necrosis was noted; it is worth mentioning that the lesions completely healed in all cases of tumor elimination. Skin lesions can occur due to the overexpression of tumor necrosis factor alpha [17]. Our results revealed higher levels of TNF- α in

untreated melanomas and a significant decrease of this factor in response to all of our treatments. TNF- α correlates with melanoma aggressiveness and metastatic potential *in vivo* [18], and its overexpression has been reported in advanced primary melanomas by Rossi et al. [19].

It is important to mention that TNF- α is a pleiotropic cytokine, and its proapoptotic effects against cancer cells have been widely described [20]; however, melanoma cells resist TNF- α -induced apoptosis through NF- κ B and nitric oxide [21].

In this study, our results showed NF- κ B and nitric oxide decrease in mice treated with Ag, DCA, or the combination of both, correlating with tumor regression. Wang et al. reported that NF- κ B suppresses TNF- α -mediated apoptosis through the activation of the antiapoptotic proteins TRAF1, TRAF2, c-IAP1, and c-IAP2 [22]. On the

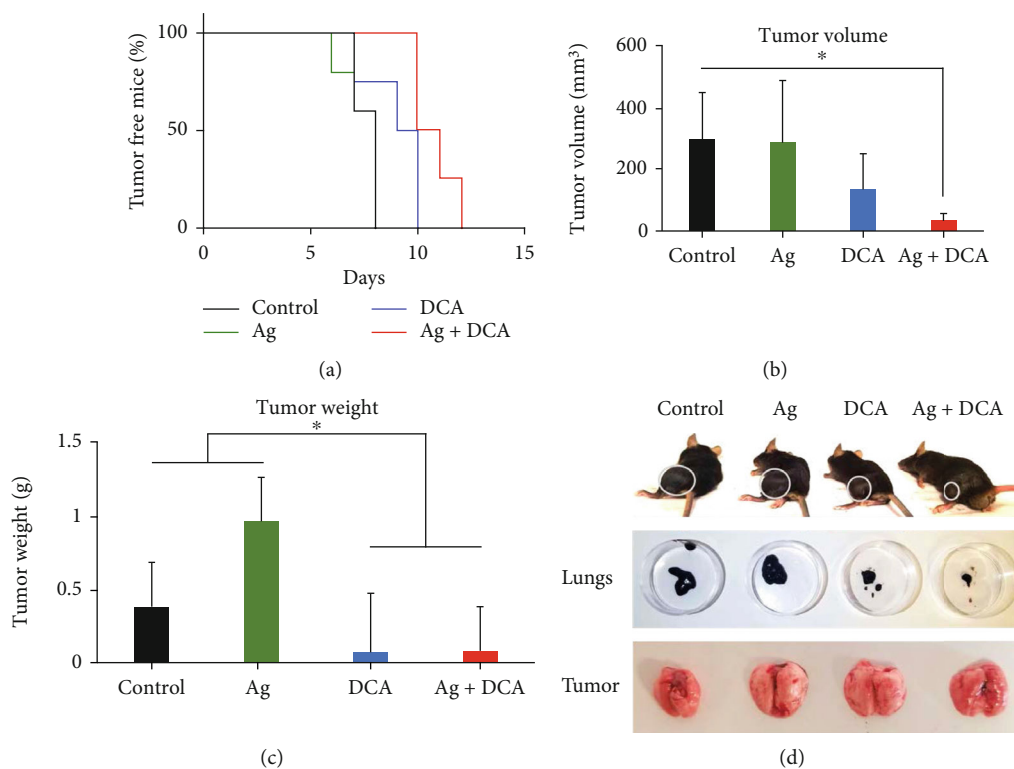


FIGURE 5: Tumor implantation in vaccinated mice. C57BL/6 mice were randomly divided into 4 groups: mice without immunization (control) and mice immunized with B16F10 cells (5×10^6) lysed with Ag (6.5×10^{-5} mM), DCA (300 mM), or Ag + DCA (2.8×10^{-5} mM and 195 mM, respectively). Seven days after immunization, mice were challenged with 0.5×10^6 B16F10 viable cells injected into the left flank. Tumor appearance was monitored daily by palpation, and on the day of the sacrifice, tumor volume was determined with the equation: tumor volume = $(L \times W^2)/2$, where L is the longest side and W is the shortest side. The image shows the percentage of mice without tumor (tumor free mice) (a), tumor volume (b), and weight (c) on day 12 after the challenge, and a representative mouse, tumor, and lungs of each group. (d) There is no statistical difference ($p \leq 0.05$) between bars labelled with the (*) in the graph.

other hand, Salvucci et al. reported nitric oxide production in human melanoma cells, and blocking this production induces cell death in human melanoma [23]. Specifically, nitric oxide inhibits at least seven caspases through s-nitrosylation [24].

Despite our observations, it is important to mention that TNF- α , NF- κ B, and NO have pleiotropic effects, and their role in melanoma is not well understood. However, we emphasize that our results indicate that these molecules decrease in correlation with tumor regression and wound healing.

Many anticancer therapies have the potential to induce cancer cell death, resulting in tumor elimination and a patient free of malignancy. However, only immunogenic cell death inducers can prevent cancer recurrence. Therefore, drugs that induce immunogenic cell death represent a recent innovation in the field of onco-immunotherapy [25], such is the case of the use of immunomodulator IMMUNEPOTENT CRP, that recently demonstrated this capacity [12]. We set out to evaluate whether our treatments were capable of inducing an immunogenic cell death.

The presence of alarmins *in vitro* indicates the potential to induce immunogenic cell death [26]. But, despite treatment-dependent increase of HMGB1, HSP70, and HSP90 (but not calreticulin), the vaccination of mice with

B16F10 cells lysed with Ag, DCA, or the combination Ag + DCA did not induce immunogenic cell death as evidenced by the tumor appearance in all mice (vaccinated or unvaccinated) after challenge with viable B16F10 cells. Tumor growth indicates a specific immune response was not induced by the vaccines. A reason for this could be that DCA, Ag, and DCA + Ag do not induce the release of DAMPs in a coordinated spatiotemporal pattern; therefore, they lack the capacity to induce cytokines and efficient antigen presentation [27].

In conclusion, the combination of Ag and DCA has potential antitumor properties against melanoma cells; however, the *in vivo* antitumor mechanism is not immunogenic cell death. Further studies to elucidate the cell death mechanism are important in order to design strategies and combinations with clinical efficacy against melanoma.

Data Availability

Data associated with the manuscript is available upon reasonable request.

Conflicts of Interest

The authors declare that there is no conflict of interest.

Acknowledgments

This study was supported by “Fondo Sectorial de Investigación para la Educación” grant A1-S-35951, CONACYT, México. We thank MsC. Alejandra Arreola Triana for manuscript revision.

References

- [1] D. B. Johnson and J. A. Sosman, “Update on the targeted therapy of melanoma,” *Current Treatment Options in Oncology*, vol. 14, no. 2, pp. 280–292, 2013.
- [2] E. A. Zaal and C. R. Berkers, “The influence of metabolism on drug response in cancer,” *Frontiers in Oncology*, vol. 8, p. 500, 2018.
- [3] Z.-F. Lim and P. C. Ma, “Emerging insights of tumor heterogeneity and drug resistance mechanisms in lung cancer targeted therapy,” *Journal of Hematology & Oncology*, vol. 12, no. 1, p. 134, 2019.
- [4] V. De Matteis, M. Cascione, C. Toma, and S. Leporatti, “Silver nanoparticles: synthetic routes, in vitro toxicity and theranostic applications for cancer disease,” *Nanomaterials*, vol. 8, no. 5, p. 319, 2018.
- [5] N. Durán, W. J. Fávoro, and A. B. Seabra, “What do we really know about nanotoxicology of silver nanoparticles in vivo? New aspects, possible mechanisms, and perspectives,” *Current Nanoscience*, vol. 16, no. 3, pp. 292–320, 2020.
- [6] M. Ahamed, M. S. AlSalhi, and M. K. J. Siddiqui, “Silver nanoparticle applications and human health,” *Clinica Chimica Acta*, vol. 411, no. 23–24, pp. 1841–1848, 2010.
- [7] K. Habiba, K. Aziz, K. Sanders et al., “Enhancing colorectal cancer radiation therapy efficacy using silver nanoprisms decorated with graphene as radiosensitizers,” *Scientific Reports*, vol. 9, no. 1, p. 17120, 2019.
- [8] T. Tataranni and C. Piccoli, “Dichloroacetate (DCA) and cancer: an overview towards clinical applications,” *Oxidative Medicine and Cellular Longevity*, vol. 2019, 14 pages, 2019.
- [9] S. Pustynnikov, F. Costabile, S. Beghi, and A. Facciabene, “Targeting mitochondria in cancer: current concepts and immunotherapy approaches,” *Translational Research*, vol. 202, pp. 35–51, 2018.
- [10] S. Grazioli and J. Pugin, “Mitochondrial damage-associated molecular patterns: from inflammatory signaling to human diseases,” *Frontiers in Immunology*, vol. 9, p. 832, 2018.
- [11] Y. Nie, D. Yang, and J. J. Oppenheim, “Alarmins and antitumor immunity,” *Clinical Therapeutics*, vol. 38, no. 5, pp. 1042–1053, 2016.
- [12] M. Rodríguez-Salazar, M. A. Franco-Molina, E. Mendoza-Gamboa et al., “The novel immunomodulator IMMUNEPOTENT CRP combined with chemotherapy agent increased the rate of immunogenic cell death and prevented melanoma growth,” *Oncology Letters*, vol. 14, no. 1, pp. 844–852, 2017.
- [13] C. A. Sierra Rivera, M. A. Franco Molina, E. Mendoza Gamboa, P. Zapata Benavides, R. S. Tamez Guerra, and C. Rodriacut euz Padilla, “Potential of colloidal or silver nanoparticles to reduce the growth of B16F10 melanoma tumors,” *African Journal of Microbiology Research*, vol. 7, no. 22, pp. 2745–2750, 2013.
- [14] L. M. Valenzuela-Salas, N. G. Girón-Vázquez, J. C. García-Ramos et al., “Antiproliferative and antitumour effect of non-genotoxic silver nanoparticles on melanoma models,” *Oxidative Medicine and Cellular Longevity*, vol. 2019, 12 pages, 2019.
- [15] A. L. R. LazarAA-n, A. Zugasti Cruz, G A A.jn. A. de la PeAAa, S. Y. S. Belmares, and C. A. Sierra Rivera, “Synergistic cytotoxic effect of sodium dichloroacetate combined with chemotherapeutic drugs on B16F10 murine melanoma cell line,” *Biomedical Research*, vol. 30, no. 1, 2019.
- [16] R. B. Mokhtari, T. S. Homayouni, N. Baluch et al., “Combination therapy in combating cancer,” *Oncotarget*, vol. 8, no. 23, pp. 38022–38043, 2017.
- [17] A. M. Brotas, J. M. T. Cunha, E. H. J. Lago, C. C. N. Machado, and S. C. S. Carneiro, “Tumor necrosis factor-alpha and the cytokine network in psoriasis,” *Anais Brasileiros de Dermatologia*, vol. 87, no. 5, pp. 673–683, 2012.
- [18] S. Moretti, C. Pinzi, A. Spallanzani et al., “Immunohistochemical evidence of cytokine networks during progression of human melanocytic lesions,” *International Journal of Cancer*, vol. 84, no. 2, pp. 160–168, 1999.
- [19] S. Rossi, M. Cordella, C. Tapolacci et al., “TNF-alpha and metalloproteases as key players in melanoma cells aggressiveness,” *Journal of Experimental & Clinical Cancer Research*, vol. 37, no. 1, p. 326, 2018.
- [20] A. Montfort, C. Colacios, T. Levade, N. Andrieu-Abadie, N. Meyer, and B. Ségui, “The TNF paradox in cancer progression and immunotherapy,” *Frontiers in Immunology*, vol. 10, p. 1818, 2019.
- [21] V. A. Soldatenkov, A. Dritschilo, Z. Ronai, and S. Y. Fuchs, “Inhibition of homologue of Slimb (HOS) function sensitizes human melanoma cells for apoptosis,” *Cancer Research*, vol. 59, no. 20, pp. 5085–5088, 1999.
- [22] C. Wang, M. W. Mayo, R. G. Korneluk, D. V. Goeddel, and Baldwin AS Jr, “NF-B antiapoptosis: induction of TRAF1 and TRAF2 and c-IAP1 and c-IAP2 to suppress caspase-8 activation,” *Science*, vol. 281, no. 5383, pp. 1680–1683, 1998.
- [23] O. Salvucci, M. Carsana, I. Bersani, G. Tragni, and A. Anichini, “Antiapoptotic role of endogenous nitric oxide in human melanoma cells,” *Cancer Research*, vol. 61, no. 1, pp. 318–326, 2001.
- [24] L. Rössig, B. Fichtlscherer, K. Breitschopf et al., “Nitric oxide inhibits caspase-3 by S-nitrosation in vivo,” *The Journal of Biological Chemistry*, vol. 274, no. 11, pp. 6823–6826, 1999.
- [25] B. Rapoport and R. Anderson, “Realizing the clinical potential of immunogenic cell death in cancer chemotherapy and radiotherapy,” *International Journal of Molecular Sciences*, vol. 20, no. 4, p. 959, 2019.
- [26] A. Terenzi, C. Pirker, B. K. Keppler, and W. Berger, “Anticancer metal drugs and immunogenic cell death,” *Journal of Inorganic Biochemistry*, vol. 165, pp. 71–79, 2016.
- [27] O. Kepp, L. Menger, E. Vacchelli et al., “Crosstalk between ER stress and immunogenic cell death,” *Cytokine & Growth Factor Reviews*, vol. 24, no. 4, pp. 311–318, 2013.